ENERGY TRANSFER IN NANOSTRUCTURED SYSTEMS

A Dissertation
Presented to
The Academic Faculty

By

Daniel Saldinger O'Neil

In Partial Fulfillment of
Of the requirements of the Degree
Doctor of Philosophy in Chemistry

Georgia Institute of Technology

August, 2017

ENERGY TRANSFER IN NANOSTRUCTURED SYSTEMS

Approved by:

Dr. Mostafa El-Sayed, Advisor
School of Chemistry and Biochemistry
Georgia Institute of Technology

Dr. Kenneth Brown
School of Chemistry and Biochemistry
Georgia Institute of Technology

Dr. Robert Dickson
School of Chemistry and Biochemistry
Georgia Institute of Technology

Dr. Seth Marder
School of Chemistry and Biochemistry
Georgia Institute of Technology

Dr. Vladimir Tsukruk
School of Materials Science and Engineering
Georgia Institute of Technology

Date Approved: 5-19-17

ACKNOWLEDGEMENTS

Science is rarely a solitary pursuit and I owe a great deal to the friends, family, mentors, and colleagues who helped, taught, and supported me along my way to produce this document. To all those mentioned below, and those I failed to mention – thank you.

This work was made possible because Dr. Mostafa El-Sayed generously adopted me into his group. When I was trying to find a group to join at Georgia Tech he took me on as a temporary researcher before I could enter as a graduate student. His commitment to training and mentorship has been indispensable – he taught me how to be a scientist.

Before coming to Georgia Tech I was advised by Dr. Hal Van Ryswyk at Harvey Mudd College Dr. John Arnold at UC Berkeley. Hal inspired my love of kinetics and taught me how to build my first dye sensitized solar cell. John taught me how to do air-sensitive chemistry and when I decided that I did not enjoy air-sensitive chemistry, helped me to find another field that I preferred.

I have been fortunate to have numerous formal and informal collaborations with gifted scientists. Dr. Paul Szymanski, thank you for teaching me how to use a laser without blinding myself. Dr. Mahmoud Mahmoud, thank you for teaching me how to make nanoparticles of every color. To all of those in Dr. Seth Marder's group – Rebecca Hill, Dr. Fadi Jradi, Dr. Yulia Getmanenko, and Dr. Tim Parker – I enjoyed our collaboration and hearing an organic chemist's perspective. A similar thanks to Dr. Harry Anderson and his student Dr. Jinsze Wong – you made some cool molecules and it was fun to characterize them. I would like to thank the rest of my group as well. In particular, Dr. Nasrin Hooshmand for teaching me

DDA, Dr. Steven Hayden for my initial training, and Dr. Steven Hira, Dr. Justin Bordley, Dr. Batyr Garlyyev, Dr. Xiongwu Kang, and Mena Aioub for great support and friendship.

Lastly, I thank my family. You have shown me years of love and have made me who I am. Mom and Dad, thank you for always supporting me and helping me to find the right path. Most importantly I thank my wife Jessie for helping me through the rough spots and always being wonderful – you are the best.

TABLE OF CONTENTS

LIST OF TABLES

LIST OF FIGURES

NOMENCLATURE

Au	Gold
Ag	Silver
Cu	Copper
Cu_2O	Copper oxide
Ti	Titanium
TiO_2	Titanium dioxide
$TiCl_4$	Titanium chloride
Al_2O_3	Aluminum oxide
ZrO_2	Zirconium oxide
Mn_3O_4	Manganese (II/III) oxide
MnOx	Manganese oxide
VO_2	Vanadium dioxide
V_2O_5	Vanadium pentoxide
SiO_2	Silica
FTO	Flourine doped tin oxide
I_2	Iodine
I^-	Iodide
I_3^-	Triiodide
AuNP	Gold nanoparticle
AuNR	Gold nanorod
AuNC	Gold nanocube
AgNP	Silver nanoparticle
AgNR	Silver nanorod
AgNC	Silver nanocube
CA	Carboxylic acid
PA	Phosphonic acid
CDCA	Chenodeoxycholic acid
PVP	Polyvinylpyrrolidone
CTAB	Cetrymethylammonium bromide
nm	Nanometer
μm	Micrometer
cm	Centimeter
fs	Femtosecond
ps	Picosecond
ns	Nanosecond
ms	Millisecond
Hz	Hertz
ppm	Parts per million
V	Volts
a.u.	Arbitrary units
R	Universal gas constant
F	Faraday constant
mM	Millimolar

M	Molar
mA	Milliamp
rpm	rotations per minute
E	Electric field
N	Number density
J_{sc}	Short-circuit photocurrent
V_{oc}	Open-circuit photovoltage
FF	Fill factor
PCE	Power conversion efficiency
IPCE	Incident photon to current efficiency
τ_{rel}	Characteristic relaxation time
τ_{inj}	Characteristic injection time
η	Injection efficiency
F	Force
E_f	Fermi level
S^*/S^+	Excited state reduction potential
S/S^+	Ground state reduction potential
τ_d	Transport lifetime
τ_r	Characteristic recombination time
ω_p	Plasmon frequency
ε	Relative permittivity
ε	Strain
ε_0	Permittivity of free space
λ	Wavelength
λ_{max}	Maximum absorption wavelength
σ	Stress
CBE	Conduction band edge
EIS	Electrochemical impedance spectroscopy
SERS	Surface enhanced Raman spectroscopy
LSPR	Localized surface plasmon resonance
DDA	Discrete dipole approximation
DSSC	Dye sensitized solar cell
HOMO	Highest occupied molecular orbital
LUMO	Lowest unoccupied molecular orbital
AM	Air mass
CW	Continuous wave
AC	Alternating current
UV	Ultraviolet
IR	Infrared
NIR	Near infrared
D	Donor
A	Acceptor

SUMMARY

This dissertation contains a number of projects involving the experimental and theoretical investigation of energy transfer within nanostructured systems. Chapter 1 begins with an overview of pump-probe spectroscopy - the primary tool used for these investigations. We then look at the two classes of materials considered in the later chapters: dye sensitized solar cells and plasmonic nanoparticles. This covers the motivation for examining these systems and their photophysics.

Chapters 2 and 3 focus on exploring squaraine-based dye sensitized solar cells. The former deals with how the anchor and bridge groups within these molecules affect the energy loss and transfer processes which determine cell efficiency. We see how dye structure relates to aggregation and how this hinders effective charge transfer. The latter considers sensitizers which include an additional porphyrin chromophore. Although this improves the amount of light absorbed, it also changes the charge transfer kinetics.

Chapters 4 and 5 explore plasmonic nanoparticle systems which could be used as optical sensors. Chapter 4 looks at the mechanical properties of gold and silver nanorods and how it relates to the crystalline structure and temperature. Chapter 5 is a theoretical investigation of how gold and silver nanocubes couple to each other – a pump-probe experiment is proposed to further study the interaction.

Chapter 6 looks at hybrid metal oxide-gold nanoparticles for use in catalysis. The chapter focuses on the synthetic control of nanoparticle shape. It describes the future work of how pump-probe spectroscopy could be used to investigate catalytic enhancement mechanisms.

CHAPTER 1

1.1 The Role of Time in Science

Good science requires accurate measurements. For many disciplines, accurate measurements require precise determination of time intervals. Thus, much scientific progress relied upon inventions which more accurately measured time. Galileo's work on acceleration due to gravity in the 17th century required measuring how fast wheels rolled down a ramp – a hard task without good clocks.[4] In the late 18th century Harrison invented an accurate mechanical clock that worked at sea thus allowing explorers and cartographers to accurately determine their longitude and make good maps – a problem which had bedeviled long distance naval navigation.[5] In the 19th century high speed filming allowed people to finally answer such simple questions as 'How do horses run?'.[6] In all these cases superior time keeping led to more knowledge. The temporal control of events became even stronger in the 20th century as the invention of complex electronic circuits and, in time, lasers led to femtosecond and even attosecond measurements.

Chemists first foray into time sensitive measurements focused on why some reactions happened faster than others and why concentration had an effect on reaction rate.[7] To monitor reaction rate the concentration of the reactants or products had to be followed accurately over time. When some of the species are colored, this permits the use of colorimetry – the determination of concentration from the color of solution. When Beer's Law applies, the simple linear relationship between intensity of color and concentration makes for an easy and noninvasive determination of concentration over time. This has been used to measure the kinetics of everything from retinal photoreceptors[8] to the action of enzymes[9].

In a typical experimental procedure familiar to the thousands of students taking general chemistry each year, a reaction is initiated by mixing to reactants together.[10] This mixture is sampled – every 5 minutes, say – and an absorbance spectrum is measured. If only a single species absorbs at a particular wavelength, the absorbance at that wavelength becomes a proxy for concentration of that species.

Though powerful, this technique is limited by its time resolution. It can only measure processes which are significantly slower than the speed at which it can record absorption spectra. Although many interesting chemical transformations occur above the microsecond timescale accessible to traditional colorimetry and flash photolysis, there is a huge world of ultrafast chemistry which does not. Consider the typical speeds of fundamental chemical processes: dissociation (200 fs)[11], molecular vibration (100 fs), proton transfer (250 fs)[12], and isomerization (200 fs)[13]. The invention of the laser in the 1950s provided a new tool which revolutionized kinetics measurements.[14] Lasers are an ideal tool for these measurements because they provide short pulses of monochromatic, coherent light. This allows chemists to selectively excite certain molecules and follow their behavior.

The particular focus of this work is the technique of transient absorption spectroscopy. With laser spectroscopic techniques, the achievable time resolution is limited by the duration of and the time separation between sequential pulses. In a typical experiment, a beam of short (<100 fs) pulses is generated. This beam is divided with one portion directed to the sample as the "pump". The energy of this beam disturbs the equilibrium of the system and initiates the chemical processes of interest. The other piece of the original beam is sent through a delay line before reaching the sample. The delay line is a set of mirrors mounted on a motorized track which reflects the beam back along its original path. Every micron the mirrors move

increases the travel time of the beam by about 7 fs. This lets the operator control the time between the arrival of the pump and probe beams.

As the probe beam passes through the sample, some of it will be absorbed. After passing through, the probe beam is collected by a fiber cable and passed on to a diode detector which measures intensity. The value typically reported is transient absorption (ΔA) which is found by comparing the intensities of the transmitted probe light for the pumped vs the unpumped system. Repeating this process for many different delay times permits the mapping out of how the absorption of the system changes over time.

This thesis will cover a series of projects in which kinetics experiments, especially transient absorption, were applied to study energy flow in nanostructured systems. By understanding how quickly energy moves around, and what it does once it has moved, we can better understand efficiency losses in photovoltaic materials, mechanical properties of nanoparticles, electromagnetic coupling between nanoparticles, and photocatalysis by nanoparticles.

1.2 Transient Absorption

Transient absorption has been used to study numerous processes including the solvation of electrons[15], dissociation of molecules[16-17], vibrational and rotational energy redistribution in molecules, energy transfer in photosynthesis,[18] and electron energy redistribution in metals[16]. These measurements rely upon the wavelength and time control which lasers provide. Figure 1-1 shows a diagram for a typical transient absorption apparatus.

The critical component of all lasers is the gain medium. Typically, a material that absorbs light will become saturated (unable to absorb more light) after it is 50% excited. To illustrate this, consider a group of atoms which each have a ground state (S_0) and one excited

state S_1). There is some probability that a particular ground state atom will absorb a photon and become excited. This is exactly equal to the probability that a particular excited state atom will emit an additional photon after interacting with a photon in the process of stimulated emission. Accordingly, under intense light, the collection of atoms will reach a 50-50 mixture of ground and excited states. A gain material can reach population inversion in which there are more atoms in the excited state than the ground state. For many lasers (including the original ruby laser), this can occur because there is a second, higher energy excited state (S_2). This state quickly relaxes to the long-lived lower energy excited state. The gain material is pumped with high energy photons reaching S_2 states but not triggering stimulated emission from S_1 because the photons are the wrong wavelength. When photons of the proper wavelength to trigger stimulated emission from S_1 pass through the material, they will be amplified because more new photons will be emitted than absorbed.

Capping two ends of the gain medium with mirrors produces an optical cavity. Photons will bounce between the two ends and continue to be amplified if the medium is in population inversion. If one of the mirrors is slightly transparent some of the photons will escape and the light can be used for experiments. Additionally, the length of the cavity controls which wavelength of light will propagate and be amplified. The cavity will create constructive interference only for wavelengths which are an integer fraction of the cavity length.

The basis of transient absorption spectroscopy is a laser which can generate ultrafast pulses. In Figure 1-1 this role is served by a Ti:sapphire laser. These lasers utilize Al_2O_3 doped with titanium (III) as the gain medium and generate light around 800 nm.[18] The titanium ions are optically active and will absorb 500 nm light (often provided by a neodymium yttrium aluminum garnet laser).[16] In its excited state, the Ti^{3+} ion couples to a vibrational mode of the surrounding lattice (a phonon) and its electronic energy is thus reduced.[17] Since there are a

wide variety of phonon modes with different energies, many different emission wavelengths are possible. Control of the emission wavelength is provided by the size of the laser cavity. Different sized cavities will be resonant with different wavelengths. This allows for a wide degree of tunability in the output wavelength. By varying the cavity length, the amplified wavelength will vary.

As described, the laser will operate in continuous wave (CW) mode. To induce the creation of ultrashort laser pulses, passive mode locking is employed.[18] For passive mode locking a saturatable absorber is included in the cavity. Absorption of photons decreases depletes the number of ground state ions available to absorb light and so the absorption of the saturatable absorber will decrease. A CW beam has constant low power and so will be consistently damped by the saturatable absorber. A short pulse delivers all its energy in a brief period of time which saturates the absorber and so much of the pulse is reflected rather than absorbed. Thus, the cavity will suppress CW beams but amplify pulses. The initial pulses are produced by rapid fluctuation of the cavity length inducing power fluctuations which are amplified and shaped into pulses. In our particular system we have an additional cavity for pulse amplification. The input pulse is first stretched in time to decrease peak intensity. This passes through another gain medium which is pumped by a secondary laser increasing the intensity by up to 10^3. Finally the pulse is recompressed and exits the cavity.

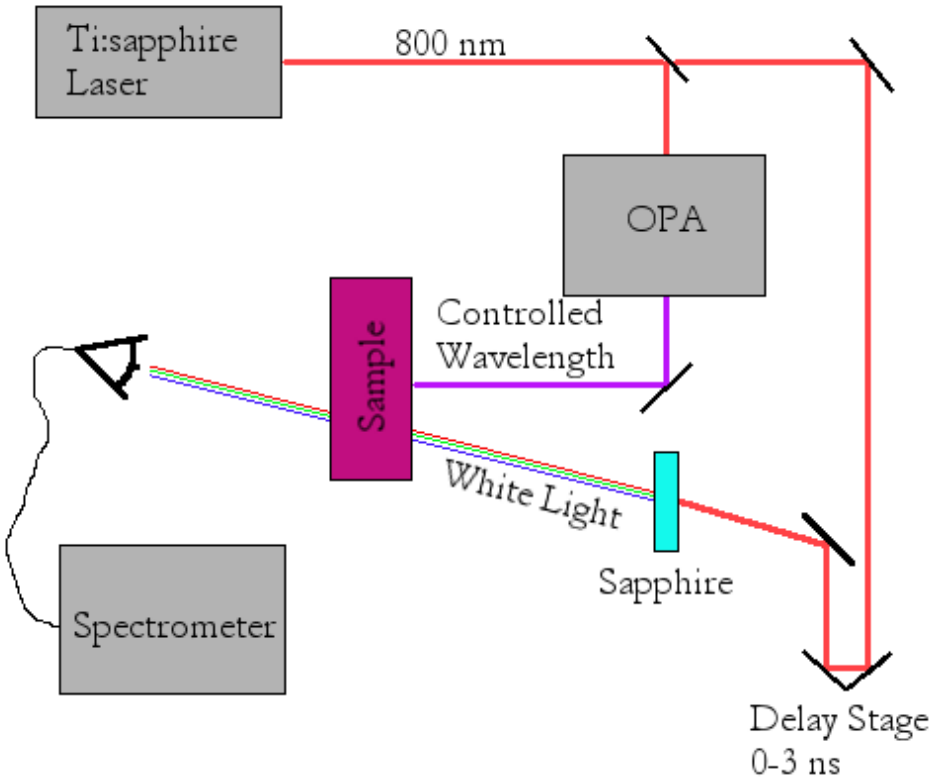

Figure 1-1. Diagram of a typical transient absorption apparatus.

The output beam is split into pump and probe components. Wavelength control of the pump beam is provided by an optical parametric amplifier. This uses nonlinear mixing effects to convert the input 800 nm beam into a beam of between 350 and 1500 nm. The probe beam is passed through a sapphire which produces white light through a process known as supercontinuum generation. This process creates undesirable dispersion within the beam in which the front of part of the pulse contains different frequencies than the end of the pulse.[16] This so-called chirp causes red light to reach the sample faster than the blue – perhaps by a few hundred femtoseconds. This may be corrected for experimentally, with additional optics[17] or software.

1.3 Solar Research

The global population is expected to reach almost 10 billion by 2050.[18] More people means more energy consumption. This is especially true as the increasingly wealthy populations of the developing nations use more energy per capita. The Energy Information Agency predicts that by 2040 the total energy consumption of the world will increase by 50%.[16] Although much of this is predicted to come from renewables, oil and natural gas consumption will increase by around 60%. If current trends continue, the increase in CO_2 emissions will have a number of potentially catastrophic changes on the environment including a decrease in ocean pH from 8.13 to 7.82 by 2100; an increase in sea levels by about 0.2 meters due to ice melt and thermal expansion; and a total temperature increase of about 2 ^{o}C by 2050.[19] These changes could be mitigated by the use of cheap carbon neutral energy generation.

In an attempt to stabilize the concentration of greenhouse gases, countries have been meeting for 21 years and developed the United Nations Framework on Climate Change (UNFCCC). Their current aim is to develop a legally binding treaty that major countries would sign to keep global warming below 2 ^{o}C. The US, china, Japan, and the EU have pledged to decrease greenhouse gas emissions by up to 40% by 2030. This would require building fewer coal power plants (or coal plants which feature carbon capture). Energy demands would be met by building more nuclear, wind, or solar requiring a tripling of their output by 2030.[20]

These goals would be substantially easier to meet if there were a technology which produced carbon free energy at a cost competitive with fossil fuels. Solar has the potential to fill this role because the operational costs of solar facilities are essentially null. With over 600 TW of practically capturable solar power globally, there is more than enough available for human consumption (currently 12.6 TW).[21-22] Unfortunately solar cells suffer from a high cost

of production, frequently use environmentally dangerous maerials[23], and produce significant amounts of greenhouse gases in their production[24-25].

Factoring into the overall cost equation of photovoltaics is the total power conversion efficiency (PCE). This figure accounts for the fraction of incident solar energy (P_{in}) converted into electrical energy (P_{out}).

$$PCE = \frac{P_{out}}{P_{in}} \quad (1)$$

The original widely deployed photovoltaic system was the silicon diode device which achieves, at best, just shy of 25% PCE.[26] The second generation of solar cells included gallium arsenide cells which have achieved an efficiency of closer to 29%.[27] which is close to the 33.1% theoretical maximum for these types of single-junction cells.[29] Research since then has diverged in two directions. The first aims to achieve higher efficiencies by exploring multi-junction devices made of materials like InGaP, InGaAs, and InGaN. These materials have efficiencies as high as 40% without a light concentrator.[30] This unfortunately comes at a significant cost for materials and production.[31]

The other research direction aims to produce photovoltaics with efficiencies similar to silicon but with much lower production costs. These fall into three main categories. Organic photovoltaics utilize easily processable conductive polymers.[32] Dye sensitized solar cells (DSSCs) make use of organic dyes, cheap TiO_2, and low processing temperatures.[33]. An outgrowth of DSSCs, organic lead halide perovskites, have recently achieved 20% efficiency and seem poised to keep improving.[34]

1.3.1 Dye Sensitized Solar Cells

Dye sensitized solar cells (DSSCs) were introduced in 1991 by O'Regan and co-workers.[32] This technology grew out of interest in photoelectrochemical water splitting – originally pioneered by Honda *et al.*[35] The major shift was to capture solar energy as an electrical

current rather than producing a chemical transformation.[34, 36] A schematic of the most common variety of DSSC is shown in Figure 1-2. The technology relies upon dye molecules bound to the surface of a semiconductor (typically TiO_2) deposited upon a conducting transparent oxide like fluorine doped tin oxide (FTO). The circuit is completed by a redox active electrolyte (commonly a mixture of I^- and I_3^-) in contact with a cathode material like platinum on FTO.

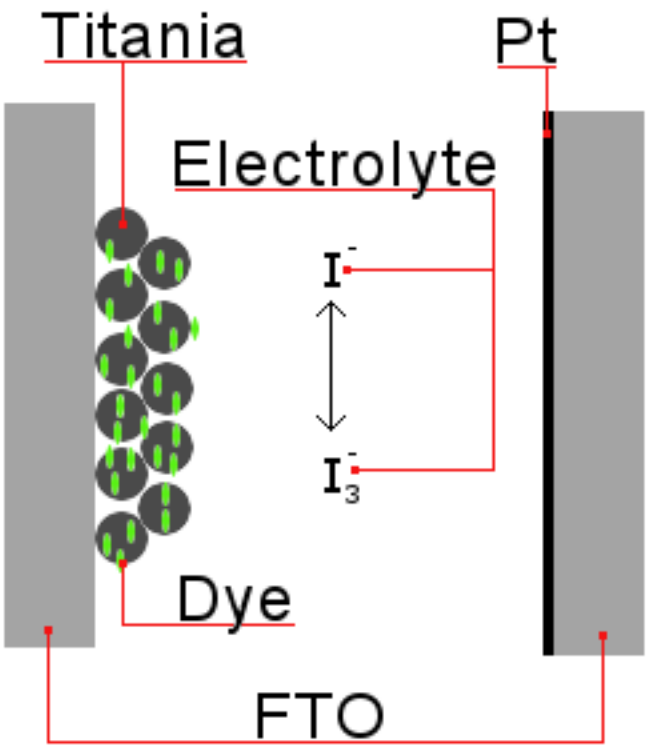

Figure 1-2. Schematic of a dye sensitized solar cell. In a typical device a dye is adsorbed on titania nanoparticles which are attached to a transparent but conductive FTO substrate. The cathode is made of a thin layer of platinum on FTO. The cell is filled with an iodide/triiodide electrolyte. In this configuration, the light enters the cell from the left side.

In standard operation the device is illuminated by light which is absorbed by the dye molecules. If the excited state of the dye lies above the conduction band of the TiO_2, it can

inject an electron into the semiconductor. The electron will slowly migrate towards the FTO and then into the external circuit. Meanwhile, the dye cation will be regenerated by the electrolyte via reduction and the electrolyte is in turn reduced by electrons from the external circuit at the cathode.

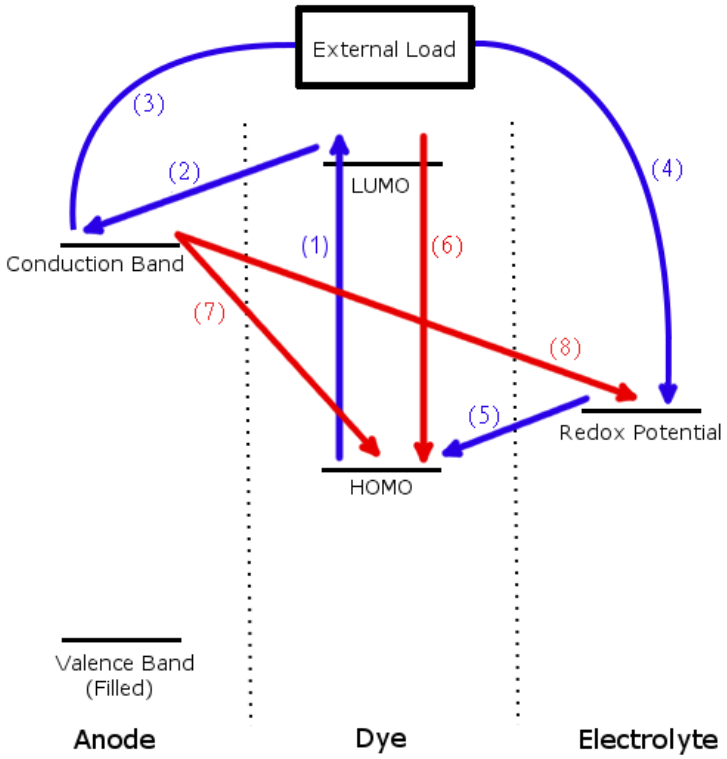

Figure 1-3. Energy level diagram of a dye sensitized solar cell. Beneficial processes are shown in blue: 1) absorption of light by the dye, 2) injection of the electron into the TiO2, 3) collection of the electron by the external circuit, 4) reduction of the electrolyte by the cathode, and 5) regeneration of the dye cation by the electrolyte. Detrimental processes are shown in red: 6) relaxation of the dye excited state, 7) recombination of electron and dye cation, and 8) scavenging of the injected electrons by the electrolyte. Although the energy levels of the dye are shown as HOMO and LUMO, this is a common simplification. It would be more accurate to include the ground and excited state reduction potentials.

Much can go wrong during the harvesting of electrons. First, the excited dye molecule can simply relax before injection occurs. This may be caused by fluorescence or radiationless

relaxation. After injection the electron may remain electrostatically bound to the dye cation and they may simply recombine.[37] Even escaping this fate, the electron takes many milliseconds to reach the FTO.[38] During this time the electron could be scavenged by the electrolyte, reducing current.[39-41] An energy level schematic of these processes is given in Figure 1-3.

1.3.1.1 Cell Efficiency

These microscopic processes have a tremendous effect on the overall operation of the cell. Several key macroscopic values are needed to describe the performance of a photovoltaic cell. Open-circuit photovoltage (V_{oc}) is the voltage that the cell will produce under standard illumination but with no current drawn. Short-circuit photocurrent (J_{sc}) is the current density the cell will produce under illumination when the external load has no resistance. The current density is simply the current the cell produces divided by its area. This allows for a direct comparison between cells that are different sizes. Fill factor (FF) describes the ideality of the diode behavior. A device with a FF of 100% would produce the max J_{sc} right up until a bias of $-V_{oc}$ was applied at which point it would give no current. In actuality, all devices will show a drop off in current as the applied bias is increased. These may be related to the PCE of the cell:

$$PCE = \frac{J_{sc}V_{oc}FF}{P_{in}} \quad (2)$$

All these values must be determined under standard illumination conditions. The most commonly applied are those of solar irradiance at noon in the Northern Hemisphere. Since the atmosphere absorbs light, the path length of the light through the atmosphere matters. A standard of 1.5 times the shortest possible path (termed air mass AM 1.5) is used. The fill factor is determined by measuring the voltage (V_{max}) and current (J_{max}) pair which give the most power output.

$$FF = \frac{J_{max} \times V_{max}}{J_{sc} \times V_{oc}} \quad (3)$$

Experimentally, these values are all determined by applying a varying voltage to the cell and measuring the resultant current. This produces a so-called IV-curve (showing a current/voltage relationship) as seen in Figure 1-4. The power at each voltage is found by multiplying the voltage by the corresponding current. There will be some peak value which is the maximum power extractable from the device. The voltage and current density for this power are J_{max} and V_{max}. The fill factor can be reduced by a variety of factors but losses from electrical resistance through the electrolyte seem to be a key factor.

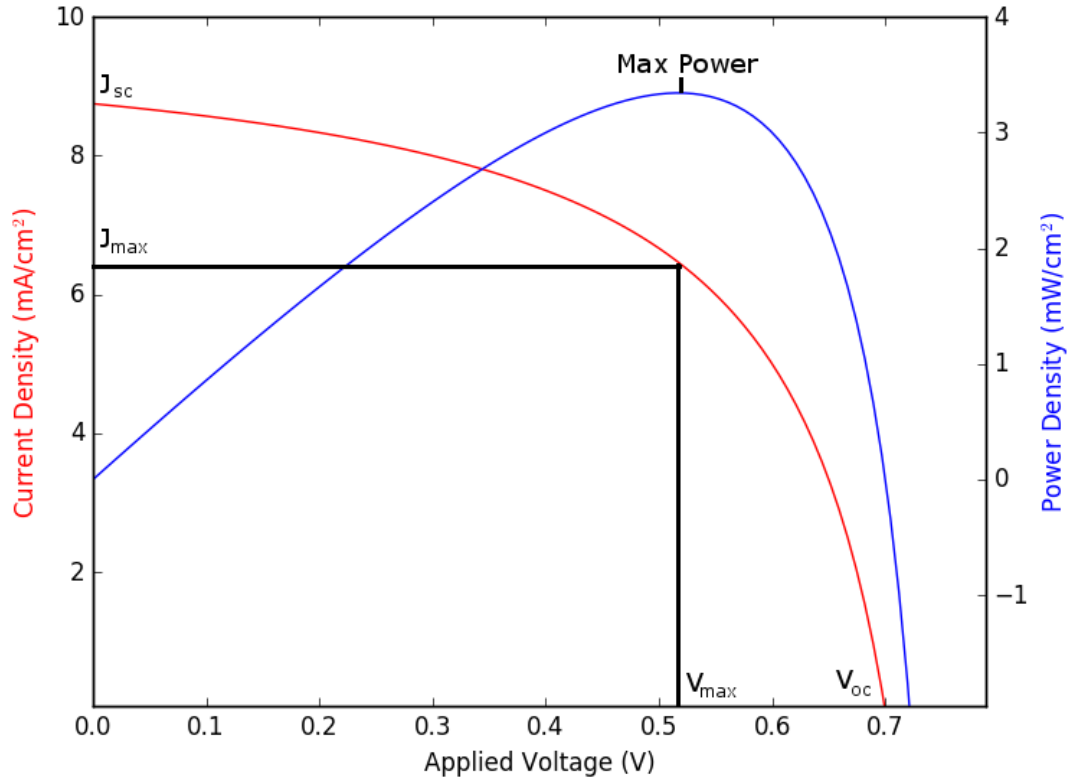

Figure 1-4. Exampled current voltage relationship for a photovoltaic device. The power curve is found by multiplying the voltage by the current density.

The V_{oc} of a device is fundamentally limited by the difference in energy between the redox couple potential and the Fermi level (E_f) of the TiO_2 (Figure 1-5). The Fermi level will be reduced by lowered electron density within the TiO_2 such as would occur under low light conditions or due to scavenging of injected electrons by the electrolyte. The potential of the redox couple is dependent upon the specific species used. Although iodide/triiodide is most common, moving to cobalt based systems can add up to 0.3 V to the V_{oc}.[42-43]

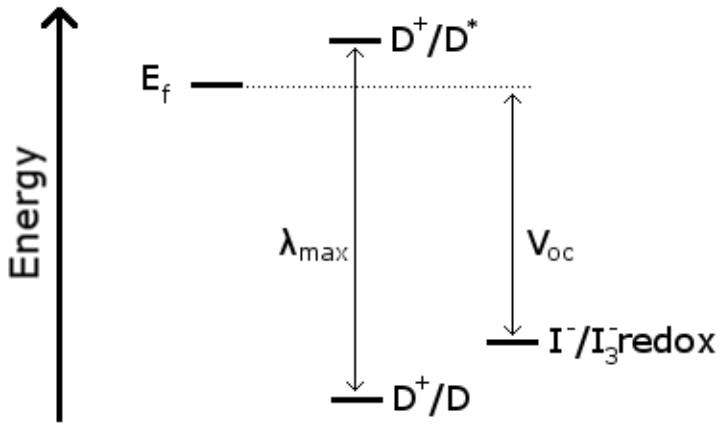

Figure 1-5. Energy levels in dye sensitized solar cells. The maximum wavelength absorbable is set by the difference between the reduction potential of the ground state dye (D+/D) and the excited state (D+/D*). The open circuit photovoltage is set by the difference between the potential of the redox couple and the Fermi energy of the TiO_2.

The short circuit photocurrent is really a measure of total quantum efficiency. Each photon impinging on the cell has the potential to create, at most, one electron of current. This is reduced when the dye molecules absorbance is too low to absorb certain regions of the spectrum. This may be because the difference in energy between ground and excited states is greater than the photon energy or there is too little dye loading. Even after absorption, any of the detrimental processes in Figure 1-3 could cause the electron to be captured. Joining these

problems are some inherent engineering issues including reflection of photons off the glass, absorption of light by the electrolyte, and scattering of light by the TiO_2.[45]

The summation of all these losses is neatly folded into the incident photon to current efficiency (IPCE) value. IPCE is a measure of how many photons at each wavelength are converted into electrons. Experimentally, it is measured by illuminating the cell with constant white light and adding a small amount fluctuating light of a specific wavelength. The variable AC component of the current is solely attributable to photons from the added colored light. Although it is possible to measure IPCE without the white light illumination, cells behave very differently when the amount of illumination is changed so this tends to give inaccurate values. Figure 1-6 shows some example data. It illustrates typical trends in IPCE. The IPCE will be near 80% where the dye absorbs light most strongly (about 570 nm in this example). It will fall off to zero at higher wavelengths where the dye absorption edge exceeds the photon energy. Although many cells absorb in excess of 90% of photons in certain windows, the IPCE does not reach this value because of the aforementioned loss pathways.[37, 47] An ideal cell would have an IPCE of 100% from the UV through 940 nm and would give a PCE of 20% with a standard iodide/triiodide electrolyte.

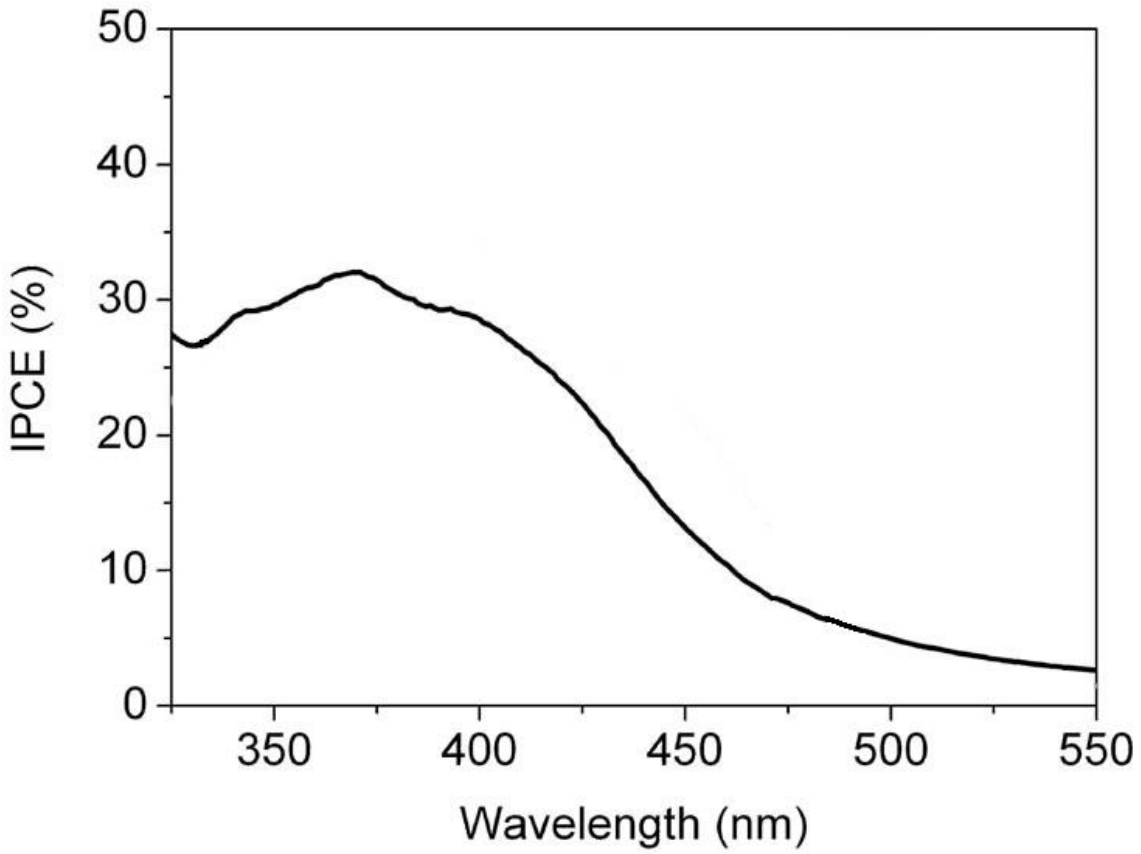

Figure 1-6. Example IPCE data. The IPCE falls off at longer wavelengths when the photon energies are less than the minimum needed to excite the dye.

1.3.1.2 Kinetics

Overall, the limits of efficiency in DSSCs comes down to the rates of the electron transfer processes of Figure 1-3. The rates of these processes span more than nine orders of magnitude from injection occurring at the picosecond scale to electron migration at the millisecond.[49] This range raises a challenge to any scientist seeking to understand the inner workings of DSSCs in an attempt to improve efficiency. The three processes which physical chemists have focused on measuring are, recombination, electron diffusion, and electron injection.

A good basis for understanding the kinetics of electron transfer is provided by Marcus theory.[51-52] In general, it provides a way to relate the change in energy as the electron is transferred to the rate of the reaction. Its results are especially applicable to electron transfer in DSSCs because the reactions typically involve little structural rearrangement. In this model the starting and ending systems are depicted as parabolas (Figure 1-7). The reaction coordinate describes how far the reaction has progressed and contains the structural rearrangement of the reactants and the surrounding solvent. To transfer from reactant 1 to reactant 2, the electron must hop from one parabola to the next. The is accomplished by tunneling through the energy barrier between the two. The size of this barrier ($\Delta G^{\ddagger}$) depends on the overall free energy favorability of the reaction (ΔG^{o}) and the similarity of the starting and ending states (λ). In general, we see that the size of the barrier will decrease and the rate (k) will increase if the reaction is more exergonic. These values can be calculated as follows:

$$\Delta G^{\ddagger} = \frac{(\Delta G^{o} + \lambda)^2}{4\lambda} \tag{4}$$

$$k = A\, e^{\Delta G^{\ddagger}/RT} \tag{5}$$

Where A is a reactant specific constant, R is the universal gas constant, and T is the temperature. One interesting result of Marcus theory is that as ΔG^{o} becomes larger, the rate will increase to a maximum before decreasing in the so-called inverted Marcus region.

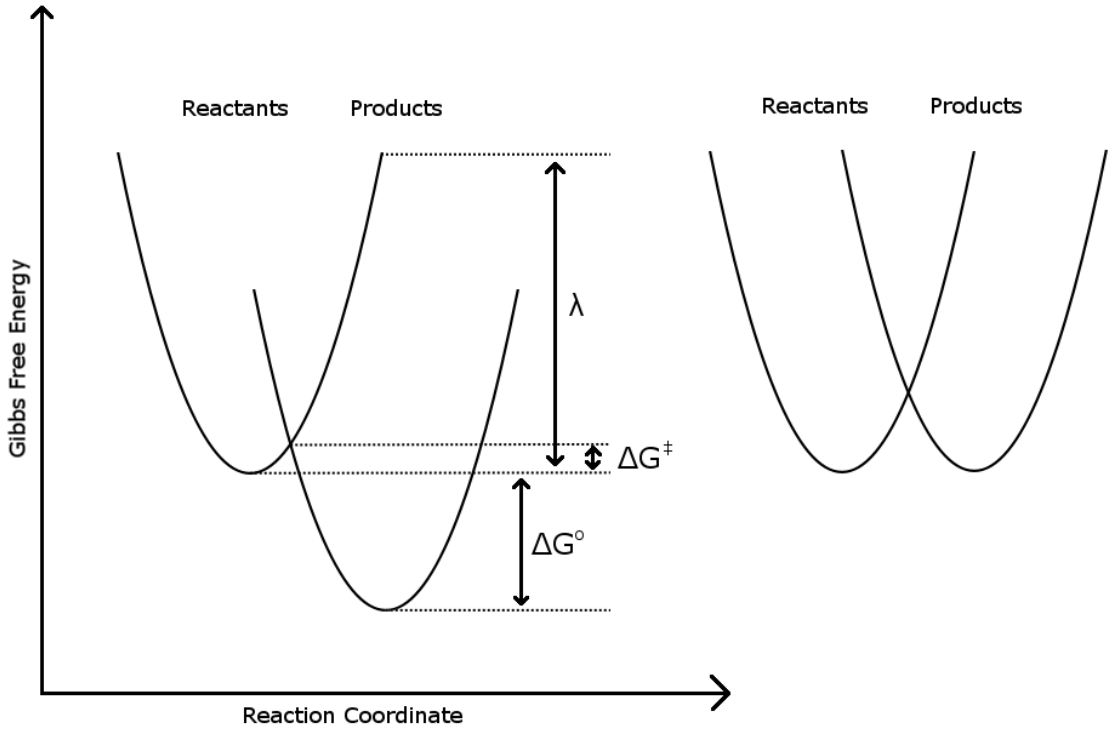

Figure 1-7. Depiction of the model of Marcus theory.

1.3.1.2.1 Recombination with the Dye Cations

After a dye molecule injects an electron into TiO_2, the electron and dye cation will remain temporarily electrostatically bound. If this exciton is long lived it will have ample opportunity for recombination. Early on it was recognized that the addition of lithium to the electrolyte will boost efficiency by upwards of 10%.[53-54] It was eventually determined that the Li^+ acts as a charge screen which reduces the exciton binding energy and facilitates rapid transit of the injected electrons away from the interface.

1.3.1.2.2 Electron diffusion

After the electron manages to escape the coulombic pull of the dye cation, it must still make its way to the external circuit. In a typical DSSC this will involve hopping through a ~10 μm layer of sintered TiO_2 nanoparticles. This process occurs via diffusion and not under the

influence of a substantial electric field (as is the case in Si diode photovoltaics). The amount of time required for electron transport is between 1 ms and 20 ms.[55] This process essentially involves hopping from one TiO_2 nanoparticle to the next. The TiO_2 nanoparticles have numerous trap sites which will slow transport as well.[58] Some groups have tried to speed the transport process by using more ordered TiO_2 morphologies like nanotubes[59] and nanowires.[61] This has the intended effect but also reduces the available surface area for dye adsorption hindering efficient photon capture.[62]

During transport, the electrons may react with the electrolyte in a process called either scavenging or recombination. The rate of recombination can be slowed by the introduction of surface protecting groups onto the TiO_2. Guanidinium reduced recombination with the electrolyte by 20 fold.[63] Recombination may also be retarded by treatment of the TiO_2 film with $TiCl_4$. This passivates surface defect sites by depositing a thin layer of new TiO_2.[64-65] The electrolyte also influences the rate of recombination. The iodide/triiodide couple has surprisingly slow kinetics because it is second order with respect to the I^- concentration.[63] Ferrocene[66] and cobalt are both much faster at dye reduction and electron recombination than iodide. Finally, the dye itself can act as an insulating layer.[69] Bulky side chain groups can restrict electrolyte access to the surface and impede recombination.[70]

Electrochemical methods are most commonly used to study recombination and transport kinetics. Intensity-modulated photocurrent spectroscopy (IMPS)[69], intensity-modulated photovoltage spectroscopy (IMVS)[70], and electrochemical impedance spectroscopy (EIS)[69] are a family of related techniques. IMPS and IMVS involve measuring changes in current or voltage, respectively, in a cell in response to fluctuations in the intensity of the illuminating light. For EIS, a fluctuating voltage is applied to the cell under illumination and the resultant current is recorded.

Analyzing EIS results requires modeling the cell with an equivalent electrical circuit composed of resistors and capacitors representing different transport and electrochemical processes.[69, 71-72] These components have impedances (resistances which change with frequency of the applied voltage) which describe how much they oppose an applied voltage. A larger impedance, Z, restricts current more. A resistor-like chemical process has an impedance which is constant with voltage frequency (e.g. a metal dissolving into an electrolyte). A capacitor-like chemical process has an impedance which varies with the frequency of the applied voltage (e.g. ions diffusing through a liquid). The impedance values can be experimentally determined from EIS and can then be equated to their fundamental physical properties like diffusion coefficient. For instance, diffusion of electrons through TiO_2 is modeled by an impedance term, Z_d:

$$Z_d = \frac{Z_0}{\sqrt{i\omega}} tanh\left(\sqrt{i\tau_d \omega}\right) \quad (6)$$

$$Z_0 = \frac{RT}{F^2 C_0 A \sqrt{D}} \quad (7)$$

$$\tau_d = \frac{d^2}{D} \quad (8)$$

Where ω is the voltage frequency, τ_d is the characteristic transport lifetime, R is the universal gas constant, T is temperature, F is the Faraday constant, C_0 is the concentration of electrons, A is the area, D is the diffusion coefficient of electrons in TiO_2, and d is the thickness of the layer. If the experimental impedance as a function of ω is measured, the values of the unknowns (D and C_0) can be solved for.

The entire process of electron diffusion and recombination with the electrolyte is represented by the following impedance, Z:

$$Z = \frac{1}{3} Z_d + \frac{R_r}{1 + i\omega/\omega_r} \quad (9)$$

Where R_r is the resistance of the interfacial recombination reaction and ω_r is the harmonic frequency of this process. This final value is relatable to the characteristic time for recombination.

$$\omega_r = \frac{1}{\tau_r} \tag{10}$$

1.3.1.2.3 Electron injection

Electron injection is typically quantified by the term injection efficiency (η) which is the percentage of excited dye molecules which inject their electrons into the TiO_2. This value depends upon the relative rates of electron injection from the dye to the TiO_2 and relaxation of the excited dye to the ground state by other means (fluorescence, radiationless relaxation). This value is frequently measured by an experiment developed by Tachibana *et al.*

To perform a measurement the relaxation of the dye excited state is measured on TiO_2 and on some other semiconductor with a wider band gap (usually ZrO_2, Al_2O_3, or SiO_2). Since the energy of the conduction band is too high, the dye is unable to inject an electron. This provides a way to measure the intrinsic excited state lifetime (τ_{rel}) in the absence of the injection pathway. This may be compared to the lifetime on TiO_2 (τ_{tot}) which must be shorter since it includes the extra relaxation pathway. The excited state lifetimes are measured optically by transient absorption spectroscopy.

For the best ruthenium dyes – N719, for one – injection efficiencies were established to be close to unity due to the sub-picosecond injection rates vs excited state lifetimes in the nanoseconds.[73-76] This, however, is not true for many organic dyes which have slower injection and/or shorter excited state lifetimes. This limits their overall efficiency and so bears studying. There are several factors which contribute to decreased injection efficiency.

The injection rate is controlled in large part by the difference between the conduction band and the dye excited state (D^*/D^+ vs E in Figure 1-5). In general, a greater energy

difference between these two will lead to a faster injection rate as per Marcus theory.[78] But too large an energy difference will yield slower kinetics as the interaction between dye and TiO_2 enters the inverted region.[79-80] Additionally, all downhill energy is lost and cannot be captured as useful voltage. A larger driving force here means either low photocurrent because the dye has a large HOMO-LUMO gap or a low photovoltage because there is little distance between the redox potential of the electrolyte and the semiconductor's conduction band. Thus there is a penalty in using dyes which have a large driving force.

1.4 Plasmonic Nanoparticles

Metal nanoparticles are fascinating materials whose optical and electronic properties differ tremendously from the bulk. Although nanoparticles are widely considered a modern invention, they have long been used to color vitreous materials. The glass walls of the Roman Lycurgus cup appear either red or green depending upon the direction of illumination (Figure 1-8). This is due to the inclusion of gold and silver nanoparticles. Colors differing so greatly from the usual hues of gold and silver are only possible because the particles are smaller than the wavelength of visible light. The small size of these nanoparticles produces unique optical properties.[78]

The properties of metal nanomaterials are not restricted to interesting colors. Below 100 nm, particles can take on new electronic, physical , and catalytic properties as well.[79] These nanomaterials have moved from the lab to the world of the consumer. Metallic nanoparticles are used in home pregnancy tests, anti-microbial band aids, and catalytic converters.[78] These products have been aided by fundamental science improving the synthesis and characterization of nanoparticles in the past few decades.

Figure 1-8. The Lycurgus cup illustrating the unusual optical properties of metallic nanoparticles. Photo credit: Marie-Lan Nguyen (2011).

1.4.1 Optical Properties of Plasmonic Nanoparticles

Although long used to color glass, Faraday was the first to identify that small gold clusters were responsible for these beautiful colors.[81] In 1857 Faraday delivered a Bakerian lecture in which he examined the interaction of light with various metals and metalloids including gold, silver, copper, aluminum, and arsenic. Though the results concerning colloidal gold nanoparticles are best remembered, he also provided examples of aerosols and thin films. Faraday prepared his gold colloids by the reduction of a gold salt ($NaAuCl_4$) with phosphorous dissolved in carbon disulfide. This produced brilliant red colors. He correctly deduced that the gold was present as minute particles saying,

> *The latter, when in their finest state, often remain unchanged for many months, and have all the appearance of solutions. But they never are such, containing in fact no dissolved, but only diffused gold. The particles are easily rendered evident, by gathering the rays of the sun (or a lamp) into a cone by a lens, and sending the part of the cone near the focus into the fluid; the cone becomes visible, and though the illuminated particles cannot be distinguished because of their minuteness, yet the light they reflect is golden in character, and is seen to be abundant in proportion to the quantity of solid gold present.*

This observation of the Tyndall effect (before John Tyndall, indeed) shows a surprisingly deep understanding of the material. He identified another famous property of colloidal gold – the variation of color with size. He noted that as the suspended particles aggregated, their color changed from red to purple and finally to a dark brown-black. He even identified that the smaller particles absorb light while the larger scatter more:

> *It would seem that more light is transmitted and absorbed and less reflected by the finer particles than by the coarser set, the same quantity of gold being in the same space.*

Although brilliant as an experimentalist, Faraday had limited mathematical abilities (his complete papers contained not a single equation). The complete explanation for these effects was developed by Gustav Mie.[82] He demonstrated how to solve Maxwell's equations for an oscillating electromagnetic field interacting with a particle. When the particle is small and made of gold it predicts the behavior that Faraday observed. This behavior differs from the typical interaction of light with macroscopic objects and is termed a localized surface plasmon resonance (LSPR). Systems other than metal nanoparticles exhibit plasmons but they lie beyond the scope of this thesis.[83] Instead, I will present an exploration of the origin of LSPRs, how the nanoparticle shape affects the optical properties, and some practical uses.

1.4.2 Plasmons

The conduction band electrons of metals are delocalized and can easily move away from their parent nuclei. When a static electric field is applied to a metal, the electrons will move in the direction of the field until an equilibrium position is reached. At this point the force of the electric field is balanced with the electrostatic pull of the nuclei and repulsion of the other electrons. If the field is released, the conduction band electrons will rapidly oscillate about their original positions in a coherent wave with frequency ω_p. This oscillation may be described as a quasiparticle termed a bulk plasmon.[80] It will dampen as the electrons collide with each other and the nuclei. This process is responsible for many of the optical properties of bulk metals. When light below ω_p illuminates the surface, the electrons can respond and screen the charge leading to reflection of the light. Above this frequency the electrons are too slow to shield and so the light is transmitted.

Surface plasmons occur when the oscillation is restricted to the surface of the metal.[84] In this case alternating regions of positive and negative charge are produced along the surface. A special example of this is the localized surface plasmon resonance observed in some nanoparticles. When the size of the nanoparticle is smaller than the wavelength of incident light, it may produce coherent oscillations of conduction band electrons as shown in Figure 1-9. Because the nanoparticle is smaller than the wavelength of light, all the electrons will experience roughly the same electric field and be pulled in a single direction thus producing the coherent oscillation of a plasmon.[85] The original mathematical treatment of this phenomenon was carried out by Mie.[84, 86] Although his solution is applicable to a wide variety of sizes, we are most interested in the case where the size of the particle is much smaller than the wavelength of light. When the incident electric field interacts with a conducting sphere

(like a nanoparticle) it will polarize it in proportion to the polarizability, α, of the sphere. The polarizability can be found using the following equation

$$\alpha = (3\varepsilon_0 V)\frac{\varepsilon-\varepsilon_m}{\varepsilon+2\varepsilon_m} \tag{11}$$

Where ε_0 is the permittivity of free space, V is the volume of the particle, ε is the permittivity of the metal, and ε_m is the permittivity of the surrounding medium. It can be seen that the polarizability will reach a maximum when $\varepsilon+2\varepsilon_m$ approaches 0. ε is strongly wavelength dependent and ε_m is approximately constant over the visible wavelengths for mediums like air and water. Maximum polarizability will be reached for the wavelength which satisfies

$$\varepsilon = -2\varepsilon_m \tag{12}$$

If the frequency of the light matches the resonant frequency of the particle it will result in strong extinction (either absorption or scattering). Although all metals (and indeed any particle with loosely bound electrons) can exhibit plasmonic resonances, silver and gold[87] are particularly well studied because they are reasonably stable under typical conditions and their resonances are near the visible light spectrum. Their high conductivity lends itself to particularly strong responses to light which is desirable for optical sensors. This is accompanied by an intense electric field surrounding the nanoparticles. The strength of this electric field has been exploited for the enhancement of Raman scattering leading to sensitivity increases on the order of 10^{10}.[88]

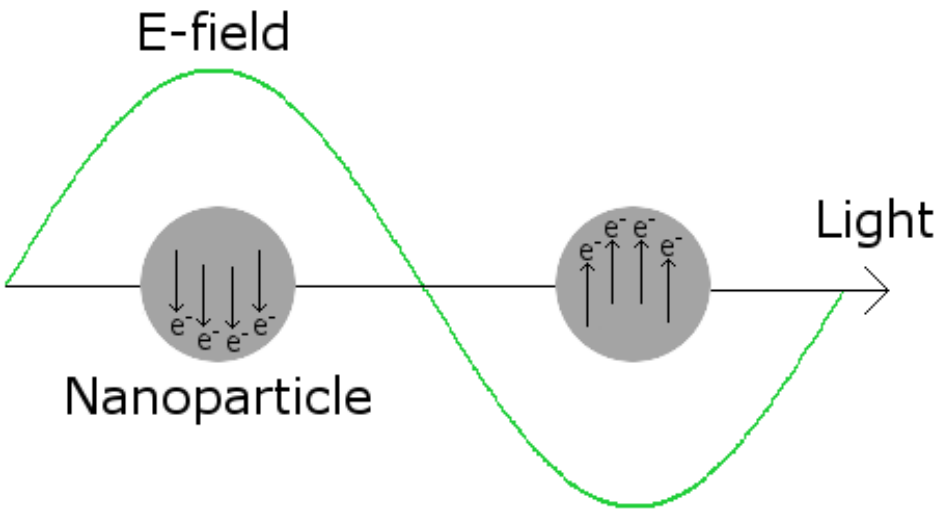

Figure 1-9. Schematic of a plasmon oscillation in a metallic nanoparticle. The incident light imparts an oscillating electric field on the nanoparticle which causes the conduction band electrons to oscillate.

The frequencies of light which resonate with a plasmonic nanoparticle will depend upon the material[90], shape[91], coupling to adjacent particles[92], medium[93], and temperature[94]. The extinction spectra for spheres, rods, and a few other shapes can be calculated exactly but most others are found numerically using methods like the discrete dipole approximation[84], finite difference time domain calculations[95], or finite element modeling[84, 96].

1.4.2.1 Surface Enhanced Raman Spectroscopy

Raman spectroscopy allows scientists to probe the vibrational modes of molecules using visible light. Standard, nonresonant Raman spectroscopy suffers from low sensitivity. Typical Raman cross sections are on the order of 10^{-30} cm^{-2} per molecule. Compare this with fluorescence cross section of a usual dye (10^{-16} cm^{-2}). It was observed in 1973 that pyridine adsorbed on a silver surface exhibited significantly stronger Raman scattering.[97] It was later found that plasmonic nanoparticles could give a similar enhancement of up to 10^{11} permitting

the detection of single molecules.[98] There are two theories to explain this enhancement effect: chemical and electromagnetic[101]. The first proposes that charge transfer from the metal to adsorbed molecules increases the polarizability of the molecule and thus increases the Raman cross section. The second suggests that plasmonic modes increase the local electric field and so increase Raman scattering. Although still unsettled, extensive studies have suggested that the electromagnetic mechanism must play a partial role in all enhancement while the chemical mechanism only participates in certain situations.[102]

The electromagnetic mechanism relies upon the fact that enhancement factor for the scattering intensity will scale with the fourth-power of the enhancement of the local electric field.[104] This is because there are two processes which will be enhanced by the electric field 1) the interaction of the incident photon with the molecule and 2) the emission of radiation from the molecule with vibrational loss. Each has a square dependence on the electric field leading to an E^4 total effect.

When a plasmonic nanoparticle is excited by resonant light it will temporarily increase the local electric field by up to 10^5. [105] As a general principal, nanoparticles with shapes that contain sharp corners will have a more dramatically enhanced electric field.[1] This explains why a roughened silver electrode was so effective at enhancing Raman scattering from pyridine. In general, the field enhancement around a single nanoparticles is less than in a coupled system so in typical analytical settings, aggregates of nanoparticles are used instead.[104] Aggregates enhance scattering because the nanoparticles will couple to each other generating even stronger electric fields in the space between. In order to optimize systems for analytical measurements, we need to understand how to strengthen the electric fields. This can be accomplished through careful simulation and measurements.

1.5 References

1. Schoenlein, R.; Peteanu, L., The first step in vision: femtosecond isomerization of rhodopsin. *Science* **1991,** *254* (5030), 412.

2. Schawlow, A. L.; Townes, C. H., Infrared and optical masers. *Physical Review* **1958,** *112* (6), 1940.

3. Alfano, J. C.; Walhout, P.; Kimura, Y.; Barbara, P. F., Ultrafast transient-absorption spectroscopy of the aqueous solvated electron. *J. Chem. Phys.* **1993,** *98* (7), 5996-5998.

4. Joly, A. G.; Nelson, K. A., Femtosecond transient absorption spectroscopy of Cr (CO) sub 6 in methanol: Observation of initial excited states and CO dissociation. *Journal of Physical Chemistry;(USA)* **1989,** *93* (8).

5. Lessing, H.; Von Jena, A., Separation of rotational diffusion and level kinetics in transient absorption spectroscopy. *Chem. Phys. Lett.* **1976,** *42* (2), 213-217.

6. Holzwarth, A. R.; Schatz, G.; Brock, H.; Bittersmann, E., Energy transfer and charge separation kinetics in photosystem I: Part 1: Picosecond transient absorption and fluorescence study of cyanobacterial photosystem I particles. *Biophys. J.* **1993,** *64* (6), 1813-1826.

7. Logunov, S.; Ahmadi, T.; El-Sayed, M.; Khoury, J.; Whetten, R., Electron dynamics of passivated gold nanocrystals probed by subpicosecond transient absorption spectroscopy. *J. Phys. Chem. B* **1997,** *101* (19), 3713-3719.

8. Link, S.; Burda, C.; Wang, Z. L.; El-Sayed, M. A., Electron dynamics in gold and gold–silver alloy nanoparticles: The influence of a nonequilibrium electron distribution and the size dependence of the electron–phonon relaxation. *J. Chem. Phys.* **1999,** *111* (3), 1255-1264.

9. Moulton, P. F., Spectroscopic and laser characteristics of Ti: Al 2 O 3. *JOSA B* **1986,** *3* (1), 125-133.

10. Yamaga, M.; Yosida, T.; Hara, S.; Kodama, N.; Henderson, B., Optical and electron spin resonance spectroscopy of Ti3+ and Ti4+ in Al2O3. *J. Appl. Phys.* **1994,** *75* (2), 1111-1117.

11. Eggleston, J. M.; Deshazer, L. G.; Kangas, K. W., Characteristics and kinetics of laser-pumped Ti: sapphire oscillators. *IEEE journal of quantum electronics* **1988,** *24* (6), 1009-1015.

12. Ippen, E.; Shank, C.; Dienes, A., Passive mode locking of the cw dye laser. *Appl. Phys. Lett.* **1972,** *21* (8), 348-350.

13. Lorenc, M.; Ziolek, M.; Naskrecki, R.; Karolczak, J.; Kubicki, J.; Maciejewski, A., Artifacts in femtosecond transient absorption spectroscopy. *Appl Phys B* **2002,** *74* (1), 19-27.

14. Klimov, V. I.; McBranch, D. W., Femtosecond high-sensitivity, chirp-free transient absorption spectroscopy using kilohertz lasers. *Opt. Lett.* **1998,** *23* (4), 277-279.

15. Economic, U. N. D. o.; Affairs, S.; Division, P., World Population Prospects: The 2015 Revision, Key Findings and Advance Tables. *Working Paper, No. ESA/P/WP. 241*. **2015**.

16. EIA, U., International energy outlook 2016. *US Energy Information Administration (EIA)* **2016**.

17. Labat, A.; Kitous, A.; Perry, M.; Saveyn, B.; Vandyck, T.; Vrontisi, V., GECO 2015-Global energy and climate outlook: road to Paris. **2015**.

18. Cozier, M., The UN COP21 Climate Change Conference and the role of CCS. *Greenhouse Gases: Science and Technology* **2015,** *5* (6), 697-700.

19. Fthenakis, V., Considering the Total Cost of Electricity From Sunlight and the Alternatives [Point of View]. *Proceedings of the IEEE* **2015,** *103* (3), 283-286.

20. Sener, C.; Fthenakis, V., Energy policy and financing options to achieve solar energy grid penetration targets: Accounting for external costs. *Renewable and Sustainable Energy Reviews* **2014,** *32*, 854-868.

21. Nugent, D.; Sovacool, B. K., Assessing the lifecycle greenhouse gas emissions from solar PV and wind energy: A critical meta-survey. *Energy Policy* **2014,** *65*, 229-244.

22. Nian, V., Impacts of changing design considerations on the life cycle carbon emissions of solar photovoltaic systems. *Applied Energy* **2016,** *183*, 1471-1487.

23. Green, M. A.; Emery, K.; Hishikawa, Y.; Warta, W.; Dunlop, E. D., Solar cell efficiency tables (Version 45). *Progress in photovoltaics: research and applications* **2015,** *23* (1), 1-9.

24. Burgess, J.; Davis, R.; Knight, J. In *Gallium arsenide solar cells*, International Conference on Future Energy Concepts, 1979; pp 40-43.

25. Yablonovitch, E.; Miller, O. D.; Kurtz, S. In *The opto-electronic physics that broke the efficiency limit in solar cells*, Photovoltaic Specialists Conference (PVSC), 2012 38th IEEE, IEEE: 2012; pp 001556-001559.

26. Shockley, W.; Queisser, H. J., Detailed balance limit of efficiency of p-n junction solar cells. *Journal of applied physics* **1961,** *32* (3), 510-519.

27. Razykov, T. M.; Ferekides, C. S.; Morel, D.; Stefanakos, E.; Ullal, H. S.; Upadhyaya, H. M., Solar photovoltaic electricity: Current status and future prospects. *Solar Energy* **2011,** *85* (8), 1580-1608.

28. Cotal, H.; Fetzer, C.; Boisvert, J.; Kinsey, G.; King, R.; Hebert, P.; Yoon, H.; Karam, N., III–V multijunction solar cells for concentrating photovoltaics. *Energy & Environmental Science* **2009,** *2* (2), 174-192.

29. Kippelen, B.; Brédas, J.-L., Organic photovoltaics. *Energy & Environmental Science* **2009,** *2* (3), 251-261.

30. Grätzel, M., Dye-sensitized solar cells. *Journal of Photochemistry and Photobiology C: Photochemistry Reviews* **2003,** *4* (2), 145-153.

31. Qin, P.; Tanaka, S.; Ito, S.; Tetreault, N.; Manabe, K.; Nishino, H.; Nazeeruddin, M. K.; Grätzel, M., Inorganic hole conductor-based lead halide perovskite solar cells with 12.4% conversion efficiency. *Nature communications* **2014,** *5*.

32. Durrant, J. R.; Haque, S. A.; Palomares, E., Towards optimisation of electron transfer processes in dye sensitised solar cells. *Coordination Chemistry Reviews* **2004,** *248* (13), 1247-1257.

33. Fujishima, A.; Honda, K., TiO2 photoelectrochemistry and photocatalysis. *Nature* **1972,** *238* (5358), 37-38.

34. Ohsaki, Y.; Masaki, N.; Kitamura, T.; Wada, Y.; Okamoto, T.; Sekino, T.; Niihara, K.; Yanagida, S., Dye-sensitized TiO 2 nanotube solar cells: fabrication and electronic characterization. *Physical Chemistry Chemical Physics* **2005,** *7* (24), 4157-4163.

35. Huang, S.; Schlichthörl, G.; Nozik, A.; Grätzel, M.; Frank, A., Charge recombination in dye-sensitized nanocrystalline TiO2 solar cells. *The Journal of Physical Chemistry B* **1997,** *101* (14), 2576-2582.

36. Nelson, J.; Chandler, R. E., Random walk models of charge transfer and transport in dye sensitized systems. *Coordination Chemistry Reviews* **2004,** *248* (13), 1181-1194.

37. Green, A. N.; Palomares, E.; Haque, S. A.; Kroon, J. M.; Durrant, J. R., Charge transport versus recombination in dye-sensitized solar cells employing nanocrystalline TiO2 and SnO2 films. *The Journal of Physical Chemistry B* **2005,** *109* (25), 12525-12533.

38. Hamann, T. W.; Ondersma, J. W., Dye-sensitized solar cell redox shuttles. *Energy & Environmental Science* **2011,** *4* (2), 370-381.

39. Mosconi, E.; Yum, J.-H.; Kessler, F.; Go□ mez Garci□ a, C. J.; Zuccaccia, C.; Cinti, A.; Nazeeruddin, M. K.; Grätzel, M.; De Angelis, F., Cobalt electrolyte/dye interactions in dye-sensitized solar cells: a combined computational and experimental study. *Journal of the American Chemical Society* **2012,** *134* (47), 19438-19453.

40. Hamann, T. W., The end of iodide? Cobalt complex redox shuttles in DSSCs. *Dalton Transactions* **2012,** *41* (11), 3111-3115.

41. Tsao, H. N.; Yi, C.; Moehl, T.; Yum, J. H.; Zakeeruddin, S. M.; Nazeeruddin, M. K.; Grätzel, M., Cyclopentadithiophene Bridged Donor–Acceptor Dyes Achieve High Power Conversion Efficiencies in Dye-Sensitized Solar Cells Based on the tris-Cobalt Bipyridine Redox Couple. *ChemSusChem* **2011,** *4* (5), 591-594.

42. Hamann, T. W.; Jensen, R. A.; Martinson, A. B.; Van Ryswyk, H.; Hupp, J. T., Advancing beyond current generation dye-sensitized solar cells. *Energy & Environmental Science* **2008,** *1* (1), 66-78.

43. Nayak, P. K.; Cahen, D., Updated assessment of possibilities and limits for solar cells. *Advanced Materials* **2014,** *26* (10), 1622-1628.

44. Barnes, P. R.; Anderson, A. Y.; Koops, S. E.; Durrant, J. R.; O'Regan, B. C., Electron injection efficiency and diffusion length in dye-sensitized solar cells derived from incident photon conversion efficiency measurements. *The Journal of Physical Chemistry C* **2008,** *113* (3), 1126-1136.

45. Hara, K.; Sato, T.; Katoh, R.; Furube, A.; Ohga, Y.; Shinpo, A.; Suga, S.; Sayama, K.; Sugihara, H.; Arakawa, H., Molecular design of coumarin dyes for efficient dye-sensitized solar cells. *Journal of Physical Chemistry B-Condensed Phase* **2003,** *107* (2), 597-606.

46. Snaith, H. J., Estimating the maximum attainable efficiency in dye-sensitized solar cells. *Advanced Functional Materials* **2010,** *20* (1), 13-19.

47. Cherepy, N. J.; Smestad, G. P.; Grätzel, M.; Zhang, J. Z., Ultrafast Electron Injection: Implications for a Photoelectrochemical Cell Utilizing an Anthocyanin Dye-Sensitized TiO2 Nanocrystalline Electrode Nerine. *Journal of Physical Chemistry B* **1997,** *101*, 9342-9351.

48. Marcus, R. A., On the theory of oxidation-reduction reactions involving electron transfer. I. *The Journal of Chemical Physics* **1956,** *24* (5), 966-978.

49. Clifford, J. N.; Martínez-Ferrero, E.; Viterisi, A.; Palomares, E., Sensitizer molecular structure-device efficiency relationship in dye sensitized solar cells. *Chemical Society Reviews* **2011,** *40* (3), 1635-1646.

50. Bach, U.; Lupo, D.; Comte, P.; Moser, J.; Weissörtel, F.; Salbeck, J.; Spreitzer, H.; Grätzel, M., Solid-state dye-sensitized mesoporous TiO2 solar cells with high photon-to-electron conversion efficiencies. *Nature* **1998,** *395* (6702), 583-585.

51. Yu, Q.; Wang, Y.; Yi, Z.; Zu, N.; Zhang, J.; Zhang, M.; Wang, P., High-efficiency dye-sensitized solar cells: the influence of lithium ions on exciton dissociation, charge recombination, and surface states. *ACS nano* **2010,** *4* (10), 6032-6038.

52. Bai, Y.; Zhang, J.; Wang, Y.; Zhang, M.; Wang, P., Lithium-modulated conduction band edge shifts and charge-transfer dynamics in dye-sensitized solar cells based on a dicyanamide ionic liquid. *Langmuir* **2011,** *27* (8), 4749-4755.

53. Adachi, M.; Sakamoto, M.; Jiu, J.; Ogata, Y.; Isoda, S., Determination of parameters of electron transport in dye-sensitized solar cells using electrochemical impedance spectroscopy. *The Journal of Physical Chemistry B* **2006,** *110* (28), 13872-13880.

54. Lee, K.-M.; Suryanarayanan, V.; Ho, K.-C., A study on the electron transport properties of TiO 2 electrodes in dye-sensitized solar cells. *Solar Energy Materials and Solar Cells* **2007,** *91* (15), 1416-1420.

55. Nelson, J.; Haque, S. A.; Klug, D. R.; Durrant, J. R., Trap-limited recombination in dye-sensitized nanocrystalline metal oxide electrodes. *Physical Review B* **2001,** *63* (20), 205321.

56. Jennings, J. R.; Ghicov, A.; Peter, L. M.; Schmuki, P.; Walker, A. B., Dye-sensitized solar cells based on oriented TiO2 nanotube arrays: transport, trapping, and transfer of electrons. *Journal of the American Chemical Society* **2008,** *130* (40), 13364-13372.

57. Mor, G. K.; Shankar, K.; Paulose, M.; Varghese, O. K.; Grimes, C. A., Use of highly-ordered TiO2 nanotube arrays in dye-sensitized solar cells. *Nano letters* **2006,** *6* (2), 215-218.

58. Law, M.; Greene, L. E.; Johnson, J. C.; Saykally, R.; Yang, P., Nanowire dye-sensitized solar cells. *Nature materials* **2005,** *4* (6), 455-459.

59. Zhu, K.; Vinzant, T. B.; Neale, N. R.; Frank, A. J., Removing structural disorder from oriented TiO2 nanotube arrays: reducing the dimensionality of transport and recombination in dye-sensitized solar cells. *Nano Letters* **2007,** *7* (12), 3739-3746.

60. Kopidakis, N.; Neale, N. R.; Frank, A. J., Effect of an adsorbent on recombination and band-edge movement in dye-sensitized TiO2 solar cells: evidence for surface passivation. *The Journal of Physical Chemistry B* **2006,** *110* (25), 12485-12489.

61. O'Regan, B. C.; Durrant, J. R.; Sommeling, P. M.; Bakker, N. J., Influence of the TiCl4 treatment on nanocrystalline TiO2 films in dye-sensitized solar cells. 2. Charge density, band edge shifts, and quantification of recombination losses at short circuit. *The Journal of Physical Chemistry C* **2007,** *111* (37), 14001-14010.

62. Fabregat-Santiago, F.; Bisquert, J.; Garcia-Belmonte, G.; Boschloo, G.; Hagfeldt, A., Influence of electrolyte in transport and recombination in dye-sensitized solar cells studied by impedance spectroscopy. *Solar Energy Materials and Solar Cells* **2005,** *87* (1), 117-131.

63. Klahr, B. M.; Hamann, T. W., Performance enhancement and limitations of cobalt bipyridyl redox shuttles in dye-sensitized solar cells. *The Journal of Physical Chemistry C* **2009,** *113* (31), 14040-14045.

64. Daeneke, T.; Kwon, T.-H.; Holmes, A. B.; Duffy, N. W.; Bach, U.; Spiccia, L., High-efficiency dye-sensitized solar cells with ferrocene-based electrolytes. *Nature chemistry* **2011,** *3* (3), 211-215.

65. Feldt, S. M.; Cappel, U. B.; Johansson, E. M.; Boschloo, G.; Hagfeldt, A., Characterization of surface passivation by poly (methylsiloxane) for dye-sensitized solar cells employing the ferrocene redox couple. *The Journal of Physical Chemistry C* **2010,** *114* (23), 10551-10558.

66. Feldt, S. M.; Gibson, E. A.; Gabrielsson, E.; Sun, L.; Boschloo, G.; Hagfeldt, A., Design of organic dyes and cobalt polypyridine redox mediators for high-efficiency dye-sensitized solar cells. *Journal of the American Chemical Society* **2010,** *132* (46), 16714-16724.

67. Cai, N.; Zhang, J.; Xu, M.; Zhang, M.; Wang, P., Improving the Photovoltage of Dithienopyrrole Dye-Sensitized Solar Cells via Attaching the Bulky Bis (octyloxy) biphenyl Moiety to the Conjugated π-Linker. *Advanced Functional Materials* **2013,** *23* (28), 3539-3547.

68. Gao, P.; Kim, Y. J.; Yum, J.-H.; Holcombe, T. W.; Nazeeruddin, M. K.; Grätzel, M., Facile synthesis of a bulky BPTPA donor group suitable for cobalt electrolyte based dye sensitized solar cells. *Journal of Materials Chemistry A* **2013,** *1* (18), 5535-5544.

69. Asbury, J. B.; Ellingson, R. J.; Ghosh, H. N.; Ferrere, S.; Nozik, A. J.; Lian, T., Femtosecond IR Study of Excited-State Relaxation and Electron-Injection Dynamics of Ru (dcbpy)~ 2 (NCS)~ 2 in Solution and on Nanocrystalline TiO~ 2 and Al~ 2O~ 3 Thin Films. *Journal of Physical Chemistry B* **1999,** *103*, 3110-3119.

70. Tachibana, Y.; Moser, J. E.; Grätzel, M.; Klug, D. R.; Durrant, J. R., Subpicosecond interfacial charge separation in dye-sensitized nanocrystalline titanium dioxide films. *The Journal of Physical Chemistry* **1996,** *100* (51), 20056-20062.

71. Ramakrishna, G.; Jose, D. A.; Kumar, D. K.; Das, A.; Palit, D. K.; Ghosh, H. N., Strongly Coupled Ruthenium− Polypyridyl Complexes for Efficient Electron Injection in Dye-Sensitized Semiconductor Nanoparticles. *The Journal of Physical Chemistry B* **2005,** *109* (32), 15445-15453.

72. Kuang, D.; Ito, S.; Wenger, B.; Klein, C.; Moser, J.-E.; Humphry-Baker, R.; Zakeeruddin, S. M.; Grätzel, M., High molar extinction coefficient heteroleptic ruthenium complexes for thin film dye-sensitized solar cells. *Journal of the American Chemical Society* **2006,** *128* (12), 4146-4154.

73. Kamat, P. V.; Das, S.; Thomas, K. G.; George, M. V., Ultrafast photochemical events associated with the photosensitization properties of a squaraine dye. *Chemical physics letters* **1991,** *178* (1), 75-79.

74. Hotchandani, S.; Das, S.; Thomas, K. G.; George, M.; Kamat, P. V., Interaction of semiconductor colloids with J-aggregates of a squaraine dye and its role in sensitizing nanocrystalline semiconductor films. *Research on Chemical Intermediates* **1994,** *20* (9), 927-938.

75. Moser, J. E.; Grätzel, M., Observation of temperature independent heterogeneous electron transfer reactions in the inverted Marcus region. *Chemical physics* **1993,** *176* (2-3), 493-500.

76. Tian, H.; Yang, X.; Chen, R.; Pan, Y.; Li, L.; Hagfeldt, A.; Sun, L., Phenothiazine derivatives for efficient organic dye-sensitized solar cells. *Chemical Communications* **2007,** (36), 3741-3743.

77. Yan, S. G.; Prieskorn, J. S.; Kim, Y.; Hupp, J. T., In search of the inverted region: Chromophore-based driving force dependence of interfacial electron transfer reactivity at the nanocrystalline titanium dioxide semiconductor/solution interface. *The Journal of Physical Chemistry B* **2000,** *104* (46), 10871-10877.

78. Rowe, J.; Ibach, H., Surface-state transitions of silicon in electron energy-loss spectra. *Physical Review Letters* **1973,** *31* (2), 102.

79. Faraday, M., The Bakerian lecture: experimental relations of gold (and other metals) to light. *Philosophical Transactions of the Royal Society of London* **1857,** *147*, 145-181.

80. Mie, G., Beiträge zur Optik trüber Medien, speziell kolloidaler Metallösungen. *Annalen der physik* **1908,** *330* (3), 377-445.

81. Pines, D.; Bohm, D., A collective description of electron interactions: II. Collective vs individual particle aspects of the interactions. *Physical Review* **1952,** *85* (2), 338.

82. Ritchie, R., Plasma losses by fast electrons in thin films. *Physical Review* **1957,** *106* (5), 874.

83. Kelly, K. L.; Coronado, E.; Zhao, L. L.; Schatz, G. C., The optical properties of metal nanoparticles: the influence of size, shape, and dielectric environment. American Chemical Society: 2003.

84. Nie, S.; Emory, S. R., Probing single molecules and single nanoparticles by surface-enhanced Raman scattering. *science* **1997,** *275* (5303), 1102-1106.

85. Link, S.; El-Sayed, M. A., Spectral properties and relaxation dynamics of surface plasmon electronic oscillations in gold and silver nanodots and nanorods. Citeseer: 1999.

86. Mahmoud, M.; Tabor, C.; El-Sayed, M., Surface-Enhanced Raman Scattering Enhancement by Aggregated Silver Nanocube Monolayers Assembled by the Langmuir− Blodgett Technique at Different Surface Pressures. *The Journal of Physical Chemistry C* **2009,** *113* (14), 5493-5501.

87. West, P. R.; Ishii, S.; Naik, G. V.; Emani, N. K.; Shalaev, V. M.; Boltasseva, A., Searching for better plasmonic materials. *Laser & Photonics Reviews* **2010,** *4* (6), 795-808.

88. Sherry, L. J.; Jin, R.; Mirkin, C. A.; Schatz, G. C.; Van Duyne, R. P., Localized surface plasmon resonance spectroscopy of single silver triangular nanoprisms. *Nano letters* **2006,** *6* (9), 2060-2065.

89. Zou, S.; Schatz, G. C., Narrow plasmonic/photonic extinction and scattering line shapes for one and two dimensional silver nanoparticle arrays. *The Journal of chemical physics* **2004,** *121* (24), 12606-12612.

90. Templeton, A. C.; Pietron, J. J.; Murray, R. W.; Mulvaney, P., Solvent refractive index and core charge influences on the surface plasmon absorbance of alkanethiolate monolayer-protected gold clusters. *The Journal of Physical Chemistry B* **2000,** *104* (3), 564-570.

91. Srivastava, T.; Das, R.; Jha, R., Highly sensitive plasmonic temperature sensor based on photonic crystal surface plasmon waveguide. *Plasmonics* **2013,** *8* (2), 515-521.

92. Draine, B. T.; Flatau, P. J., Discrete-dipole approximation for scattering calculations. *JOSA A* **1994,** *11* (4), 1491-1499.

93. Mur, G., Absorbing boundary conditions for the finite-difference approximation of the time-domain electromagnetic-field equations. *IEEE transactions on Electromagnetic Compatibility* **1981,** (4), 377-382.

94. McMahon, J. M.; Henry, A.-I.; Wustholz, K. L.; Natan, M. J.; Freeman, R. G.; Van Duyne, R. P.; Schatz, G. C., Gold nanoparticle dimer plasmonics: finite element method calculations of the electromagnetic enhancement to surface-enhanced Raman spectroscopy. *Analytical and bioanalytical chemistry* **2009,** *394* (7), 1819-1825.

95. Fleischmann, M.; Hendra, P. J.; McQuillan, A. J., Raman spectra of pyridine adsorbed at a silver electrode. *Chemical Physics Letters* **1974,** *26* (2), 163-166.

96. Kneipp, K.; Wang, Y.; Kneipp, H.; Perelman, L. T.; Itzkan, I.; Dasari, R. R.; Feld, M. S., Single molecule detection using surface-enhanced Raman scattering (SERS). *Physical review letters* **1997,** *78* (9), 1667.

97. Albrecht, M. G.; Creighton, J. A., Anomalously intense Raman spectra of pyridine at a silver electrode. *J. Am. Chem. Soc* **1977,** *99* (15), 5215-5217.

98. Jeanmaire, D. L.; Van Duyne, R. P., Surface Raman spectroelectrochemistry: Part I. Heterocyclic, aromatic, and aliphatic amines adsorbed on the anodized silver electrode. *Journal of Electroanalytical Chemistry and Interfacial Electrochemistry* **1977,** *84* (1), 1-20.

99. Lombardi, J. R.; Birke, R. L., A unified approach to surface-enhanced Raman spectroscopy. *The Journal of Physical Chemistry C* **2008,** *112* (14), 5605-5617.

100. Kukushkin, V.; Van'kov, A. B.; Kukushkin, I. V., Long-range manifestation of surface-enhanced Raman scattering. *JETP letters* **2013,** *98* (2), 64-69.

101. Kerker, M.; Wang, D.-S.; Chew, H., Surface enhanced Raman scattering (SERS) by molecules adsorbed at spherical particles. *Applied optics* **1980,** *19* (19), 3373-3388.

102. Weber, W. H.; Ford, G., Optical electric-field enhancement at a metal surface arising from surface-plasmon excitation. *Optics letters* **1981,** *6* (3), 122-124.

103. Liao, P.; Wokaun, A., Lightning rod effect in surface enhanced Raman scattering. *The Journal of Chemical Physics* **1982,** *76* (1), 751-752.

104. Nikoobakht, B.; El-Sayed, M. A., Surface-enhanced Raman scattering studies on aggregated gold nanorods. *The Journal of Physical Chemistry A* **2003,** *107* (18), 3372-3378.

105. Gunnarsson, L.; Bjerneld, E.; Xu, H.; Petronis, S.; Kasemo, B.; Käll, M., Interparticle coupling effects in nanofabricated substrates for surface-enhanced Raman scattering. *Applied Physics Letters* **2001,** *78* (6), 802-804.

CHAPTER 2 – EFFECT OF LINKERS AND ANCHORING GROUPS ON ELECTRON INJECTION FROM ASYMMETRIC SQUARAINE DYES

2.1 Introduction

Dye sensitized solar cells (DSSCs) were introduced by Graetzel and O'Regan in 1991. They are the purest example of a molecular photovoltaic. Their advantage is that they split the photon absorption and charge separation processes into two different materials – an organic or organometallic dye and a semiconductor.[2] Over the decades since their inception, the efficiency has improved and reached a total power conversion efficiency (PCE) of 13%.[2] Even more impressively, the best dyes are able to convert nearly 100% of absorbed photons into electrons in the external circuit.[6-7] This means that the only way to continue to improve the PCE of these devices is to absorb a greater percentage of solar photons or to extract more energy from each photon. The original champion dye, N719, exhibits very little conversion of photons above 750 nm. However, the Shockley–Queisser limit states that the maximum efficiency achievable for a single gap photovoltaic occurs when the absorption edge is around 900 nm.[5, 8] Thus, dyes which absorb near-infrared (NIR) light would be a superior choice.

Squaraines are one promising class of organic dyes with NIR absorption. They have absorption coefficients in excess of 10^5 $M^{-1}cm^{-1}$ in the red to NIR region. This rosy outlook is clouded by the low PCEs that squaraine sensitizers typically achieve - in the sub 5% range.[10] This seems to be due to a combination of factors including low open circuit photovoltage (V_{oc}) and low IPCE even in the region of high molar extinction.[19] Supposing these problems

to be related to dye aggregation the typical structure of the dye was modified pushing the PCE of YR6 to 6.7%.[18] This section describes our work in understanding the role of squaraine structure in improving dye efficiency. Focusing on using transient absorption spectroscopy to look at injection rates from related squaraine dyes with a variety of linkers and anchoring groups.

We have taken a donor-π-acceptor (D-π-A) architecture for our dyes. This structure (Figure 2-1) involves a donor chromophore (squaraine in our work) combined with an acceptor linked by a π-bridge. The acceptor binds to TiO_2 via a carboxylic or phosphonic acid group. The HOMO of the molecule is located predominantly on the donor while the LUMO is located on the acceptor. This improves electron transfer as both injection and rejeneration rates are increased. The excited state electron density on the acceptor provides good spatial overlap with the TiO_2. The proximity of the hole on the donor to the electrolyte improves regeneration.

In addition to facilitating charge transfer, the π-bridge can act as a secondary chromophore. Since squaraines absorb in the red region, we have selected bridges which provide complimentary absorption in the blue to green regions. This grants the dyes better panchromicity and improves the usable spectral regions. The π-bridge also provides an attachment point for long alkyl chains which act as deaggregating agents.

Most photosensitizer dyes utilize a carboxylic acid with side cyanoacrylic group for anchoring to the titania. Carboxylic acids offer three advantages: 1) ease of synthesis, 2) reasonable stability, and 3) outperformance of other anchoring groups[8]- why this should be the case is under debate. The most complete analysis to date revealed that replacing the carboxylic linker with a phosphonic or silatrane drops the efficiency of the system by over half.[8] This was attributed to the carboxylic dyes packing better and having a greater surface

coverage.[15] More dye molecules means more photons absorbed and a higher resulting efficiency. Wiberg *et al.* made an even less substantial change: replacing the cyanoacrylic group with a rhodanine.[16] This gave the dye a beneficial red shift in absorbance but caused a significant decrease in PCE. Ultrafast studies showed that although injection was still occurring rapidly, charge recombination was faster in the rhodanine version dropping quantum yield. However, Wang *et al.* observed the opposite effect for a ruthenium based dye: the phosphonic version had slower recombination (and higher efficiency) than the carboxylic version.[17] This is clearly a muddied topic which raises the question "Why bother to investigate different anchoring groups at all?".

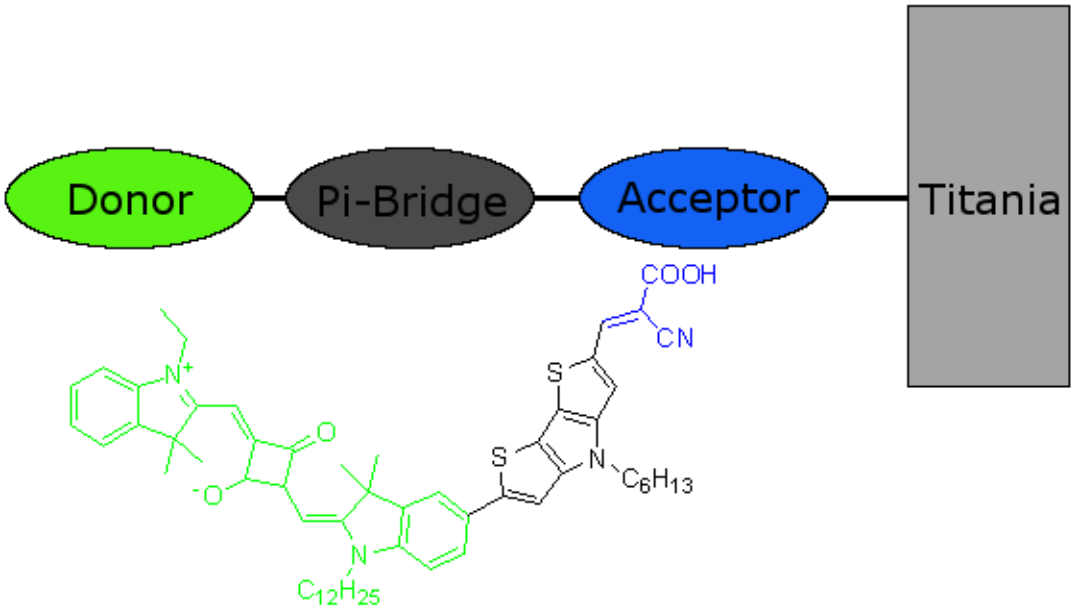

Figure 2-1. Generalized structure of a dye. The donor is the main chromophore. The π-bridge is a secondary chromophore and also shuttles electrons to the acceptor. The acceptor contains an anchor group which binds to the TiO_2.

One clear advantage that the phosphonic acid based dyes considered in this chapter have over their carboxylic counterparts is improved stability. Mulhern *et al.* and Murakami *et*

al. have demonstrated that some phosphonic anchored dyes lose less than 10% of their efficiency over 1000 hours of continuous operation compared with over 80% loss for carboxylate dyes. [15-16,] Despite the potential for photodegradation and heat induced desorption, the phosphonic acids last well during exposure.[15, 17] Since any economically feasible device will have to last for at least 20000 hours of light exposure, any modifications which can improve stability are important and worthy of further study.

2.2 Results and Discussion

Collaboration Note: Synthesis of the dyes was and electrochemical measurements were conducted by Dr. Fadi Jradi of the Marder group at Georgia Tech. Dr. Xiongwu Kang of the El-Sayed group at Georgia Tech assembled the photovoltaic devices and performed the impedance/IV measurements. I performed ultrafast dynamics measurements and assembled some of the devices.

The structures of the dyes discussed are shown in Table 2-2. In push-pull systems, light absorption triggers a transfer of charge from the donor to the acceptor. This transfer is moderated by the conjugated bridge between the systems. Accordingly, any chemical variations in the bridge will change the optical properties of the whole system. The optical and electronic properties of the dyes discussed in this section are given in Table 2-2. Cell efficiency for phosphonic anchored dyes at varying concentrations of added CDCA. The change from CA to PA anchoring group has only a slight change in λ_{max}. It does, however, lead to a 10-20% increase in the molar extinction (and similar change in the oscillator strength). The different bridges have a more pronounced effect on peak position leading to a full 10 nm shift from T to DTP. Although this was accompanied by a decrease in molar extinction, the oscillator strength was roughly the same, indicating a broadening of the peak – a beneficial

effect since it is better to have a large region of intense absorption rather than one narrow peak. The various bridge groups also introduced a higher energy absorption in the 400 nm to 500 nm region. This was strongest for the DTS and DTP groups (26,000 $M^{-1}cm^{-1}$ and 42,000 $M^{-1}cm^{-1}$, respectively).

R =	COOH	PO_3H_2
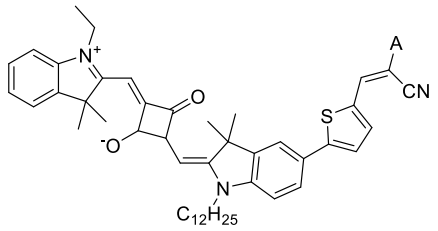	T-CA	T-PA
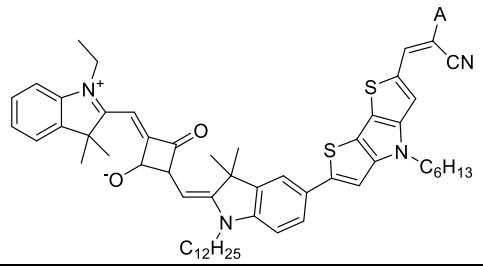	DTP-CA	DTP-PA
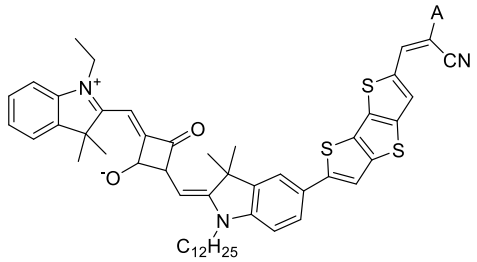	DTT-CA	DTT-PA
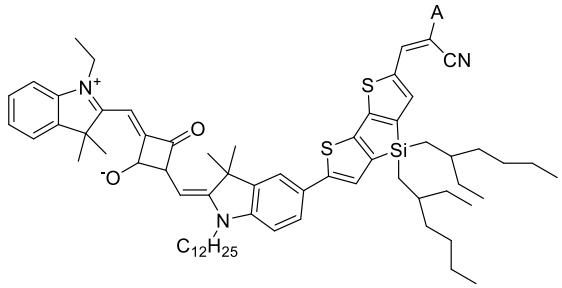	DTS-CA	DTS-PA

Figure 2-2. Structures of the eight dyes discussed in this work. The squaraine chromophore is identical in all molecules but four different bridges are used. For each bridge a carboxylic and a phosphonic acid analogue were produced.

We looked at the oxidation potentials of the ground-states ($E_{S+/S}$) and the excited-states ($E_{S+/S*}$) of the dyes to understand its influence on injection. A greater downhill force will tend to speed injection (it is unlikely that any of these dyes are in the Marcus inverted region). The energy of injection is given by the difference between $E_{S+/S*}$ and the conduction band edge of TiO_2 (~-0.5 V vs NHE). [17]. It is suggested that 0.15 V difference is necessary for efficiency injection but this value would depend upon the anchoring group, dye excited state lifetime, and aggregation.[16] Regardless, all dyes here have a driving force of 0.4-0.5 V. This should be sufficient and indeed may be in excess of what is required. This could lead to a drop in energy collected per photon with no improvement in quantum yield.

Table 2-1. Electronic and optical properties of the dyes. These are the wavelength of maximum absorption, molar extinction at this wavelength, oscillator strength, optically derived energy difference between the ground and first excited states, ground state oxidation potential, and excited state oxidation potential derived from the previous two quantities. The potentials are reported vs NHE.

Dyes	**λ_{max} (nm)**	**E ($M^{-1}cm^{-1}$)**	***f***	**$E_{0\text{-}0}^{opt}$ (eV)**	**$E_{(S+/S)}$ (V)**	**$E_{(S+/S*)}$ (V)**
T-CA	659	279,000	1.39	1.76	0.80	−0.96
T-PA	655	311,000	1.49	1.85	0.86	−0.99
DTP-CA	670	160,000	1.34	1.74	0.74	−1.00
DTP-PA	670	204,000	1.43	1.82	0.82	−1.00
DTT-CA	662	231,000	1.28	1.76	0.80	−0.99
DTT-PA	661	259,000	1.43	1.84	0.85	−0.99
DTS-CA	667	257,000	1.58	1.82	0.84	−0.98
DTS-PA	666	214,000	1.32	1.83	0.88	−0.95

On the other side of the system, the ground-state potential gives an idea of the rate of dye regeneration by the electrolyte. The iodide/triiodide redox couple has a reduction potential of 0.35 V vs NHE (this will change based on the concentrations within the cell). A driving

force of at least 0.3 V would be needed for efficient regeneration.[18] Once again, the value will depend on the specifics of the system. All dyes considered here have sufficient driving force.

2.2.1 Aggregation

Understanding the energetics of injection is important but there is another side to the efficiency equation. Regardless of how fast injection occurs, if the dye relaxes faster efficiency will be low. A key factor in relaxation rate is aggregation. Aggregation can have opposite effects on excited state lifetimes of dyes either by speeding relaxation through exciton-exciton annihilation[19-21] or slowing it by restricting vibrational motion. We investigated this effect in our DSSCs by introducing CDCA. This carboxylic acid binds to the surface of TiO_2 and acts as a spacer between the dye molecules. Generally, this improves the PCE of the devices.[19-20, 22] We observed a particular strong effect for the phosphonic acid anchored dyes (Table 2-2). Since PA groups have stronger hydrogen bonding than carboxylic acids it may be that they are more prone to the form hydrogen bonded clusters.[19] As a result, the addition of CDCA may be more necessary for forcing deaggregation in PA dyes.

Table 2-2. Cell efficiency for phosphonic anchored dyes at varying concentrations of added CDCA.

Dye	CDCA Concentration (mM)	J_{sc} (mA/cm^2)	PCE (%)
T-PA	10	9.6±0.3	4.6±0.2
T-PA	0	4.6±0.2	2.2±0.0
DTP-PA	10	5.9±0.4	2.8±0.3
DTP-PA	0	3	1.3
DTT-PA	50	3.7±0.2	1.8±0.1
DTT-PA	10	2.7±0.1	1.3±0.0
DTS-PA	10	10.4±0.2	5.0±0.09
DTS-PA	0	4.5±0.1	2.2±0.0

The formation of aggregates will result in a change in the absorption spectra of the dyes. To demonstrate that these dyes are aggregating on the surface of the TiO_2 we measured the absorption spectra in solution (Figure 2-3) and on TiO_2 (Figure 2-4). The absorption spectra on TiO_2 were obtained after soaking in 0.05 mM dye solution for 1 hour with 10 mM CDCA. The main difference between these sets of spectra is the appearance of a blue-shifted peak next to the main squaraine band around 625 nm. This hypsochromic shift is indicative of H-aggregate formation. H-aggregates have a head-to-head arrangement of dye molecules which makes sense in this system because all the molecules are bound to TiO_2 on the same end. Interestingly, this aggregation peak is much reduced for DTS-CA and DTS-PA indicating that the DTS bridge disrupts the formation of aggregates. The 2-ethylhexyl groups present on this bridge are quite bulky and could prevent the alignment of the dye molecules into H-aggregates.

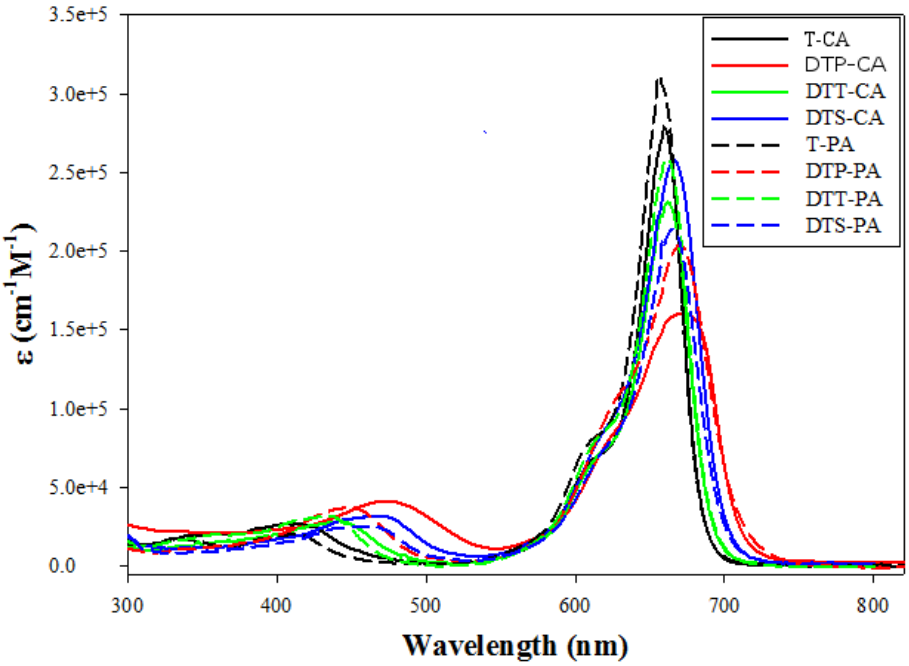

Figure 2-3. Absorption spectra for the dyes in ethanol.

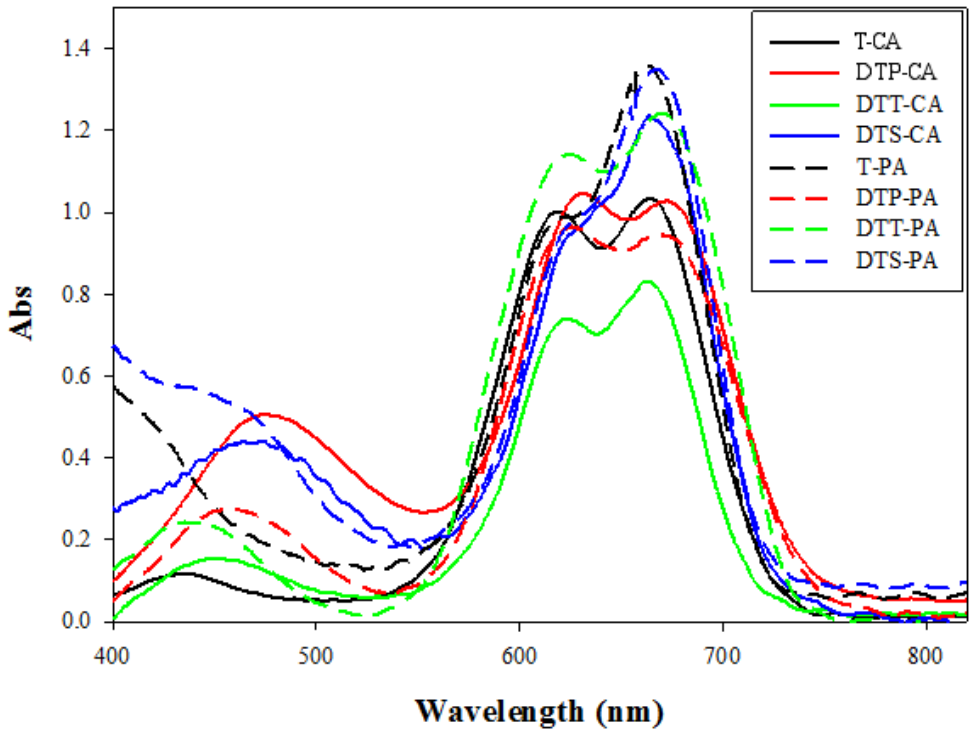

Figure 2-4. Absorption spectra of the dyes on titania.

2.2.2 Photovoltaic Measurements

The CDCA concentration of the dye soak solution was optimized for each dye and photovoltaic measurements were recorded for each (Table 2-3). The performance of DTP-CA and DTT-CA looks similar to previously studied squaraines in DSSCs.[22] The V_{oc} of squaraines is consistently low. This limits cell performance even in the cases of exceptionally high J_{sc}. DTS-CA reached 19.2 mA/cm^2 which is better than the record setting porphyrin sensitizer SM315 at 18.1 mA/cm^2. This high photocurrent was accompanied by the best V_{oc} of the set. DTS-CA achieved a 10% increase in V_{oc} compared to dyes with other bridge groups. This may be related to the decreased aggregation that we observed on TiO_2. This is the highest V_{oc} achieved for any squaraine-based sensitizer. Additionally, we see that the PA anchored

dyes have worse photovoltaic performance than their CA counterparts. This is primarily due to a drop in J_{sc} rather than V_{oc}, indicating that there may be reduced injection.

Table 2-3. Photovoltaic properties of optimized devices. The uncertainties are derived from the standard deviations of three cells.

Dye	V_{oc} (V)	J_{sc} (mA/cm^2)	FF (%)	PCE (%)
T-CA	0.647±0.006	14.2±0.3	70.4±0.2	6.5±0.1
T-PA	0.644±0.000	9.6±0.3	72.2±0.6	4.6±0.2
DTP-CA	0.61	13.5	68.3	5.6
DTP-PA	0.642±0.002	5.9±0.4	73.5±0.1	2.8±0.3
DTT-CA	0.644±0.004	13.1±0.3	71.6±1.1	6.0±0.1
DTT-PA	0.621±0.002	3.7±0.2	76.3±0.2	1.8±0.1
DTS-CA	0.682±0.000	19.1±0.2	68.3±0.7	8.9±0.2
DTS-PA	0.676±0.002	10.4±0.2	70.5±0.4	5.0±0.09

2.2.3 Charge Injection Dynamics

We studied the charge injection and excited state kinetics of these dyes to help understand how charge-injection relates to the overall PCE of the devices. Traditional ruthenium dyes tend to have very long-lived excited states which makes injection occur with nearly perfect efficiency. Squaraines and many other organic dyes tend to have much faster excited state relaxation which can compete with injection. To study their relative rates, we measured the excited-state lifetime of the dyes adsorbed on TiO_2 and Al_2O_3 in fully assembled devices. The conduction band energy of alumina is too high for injection so it provides a control that allows us to measure the excited state dynamics of the dyes in the absence of the injection pathway. This, of course, assumes that the relaxation pathways on Al_2O_3 are otherwise identical to TiO_2 but this assumption has been found to hold, generally.[25-27]

To follow the excited state dynamics we looked at the decay of the transiently induced excited state peak (typically between 475 nm to 550 nm). The data was fit using the stretched exponential function.

$$f(t) = A \exp\left[\left(-\frac{t}{\tau}\right)^{\beta}\right] \quad (1)$$

A is a scaling constant, τ is the characteristic lifetime, and β is a measure of heterogeneity that accounts for variations in the lifetime of adsorbed dyes. Different dyes have different βs and so for the ease of comparison, a weighted τ_{obs} may be calculated.

$$\tau_{obs} = \frac{\tau}{\beta}\Gamma\left(\frac{1}{\beta}\right) \quad (2)$$

Where Γ is the gamma function.

These squaraine sensitizers exhibited fairly typical excited state dynamics. A characteristic example is shown in Figure 2-5. The dynamics in this figure are from DTS-CA adsorbed on TiO_2 pumped at 405 nm. Most measurements were performed with a pump wavelength that overlapped better with the main absorption peak of the dye (closer to 650 nm) but scattered pump light adds a large negative peak which obscures the spectrum. The transient absorption spectrum exhibits a positive peak around 550 nm. This has previously been assigned as the lowest energy excited state. The negative peak from 625 nm to 800 nm is the ground state bleach – it aligns with the position of the steady-state absorption spectrum of the dye. These peaks have similar transient behavior. The bottom figure shows the normalized transient absorption at 520 nm (excited state) and 720 nm (ground state). They have similar time constants for their initial decay (τ_{adj} = 1.3 ps at 520 nm and 1.6 ps at 720 nm). One clear difference is that the while the excited state peak nearly returns to 0 at large times, the ground state remains partially bleached. This occurs because after an excited state molecule injects, it does not immediately regain the absorption spectrum of the ground state – it is

currently a cation and has a different spectrum. The probable dye cation absorption can be seen above 800 nm. The reduction of cations to the neutral form occurs over the ns time scale involving either reduction by the electrolyte or recombination with the injected electron.

Injection may be calculated in the manner described earlier using the equation:

$$\eta_{ei} = \frac{\frac{1}{\tau_{TiO_2}} - \frac{1}{\tau_{Al2O3}}}{\frac{1}{\tau_{TiO_2}}} \quad (3)$$

Finally, the implied injection lifetime can be calculated

$$\tau_{inj} = \frac{\tau_{TiO2}\tau_{Al2O3}}{\tau_{Al2O3} - \tau_{TiO2}} \quad (4)$$

The injection efficiency and excited state parameters are provided in Table 2-4. Generally, we see that the PA dyes have shorter lived excited states on alumina. This faster relaxation may be due to the increased hydrogen bonding and associated aggregation discussed earlier. This leads to a very clear drop in the injection efficiency of the PA dyes. Although all the CA dyes have over 95% quantum yield for injection, the PA dyes are 20-30% lower. This poor injection would lead to the decreased J_{sc} observed for the PA dyes. The poor injection is also caused by slower absolute injection rates. In all cases the injection rates for the PA dyes were at least four times greater than the TA counterpart. This suggests that the phosphonic acid anchor works to retard injection. One possibility is that there is poor overlap between the orbitals of the PA and the TiO_2.

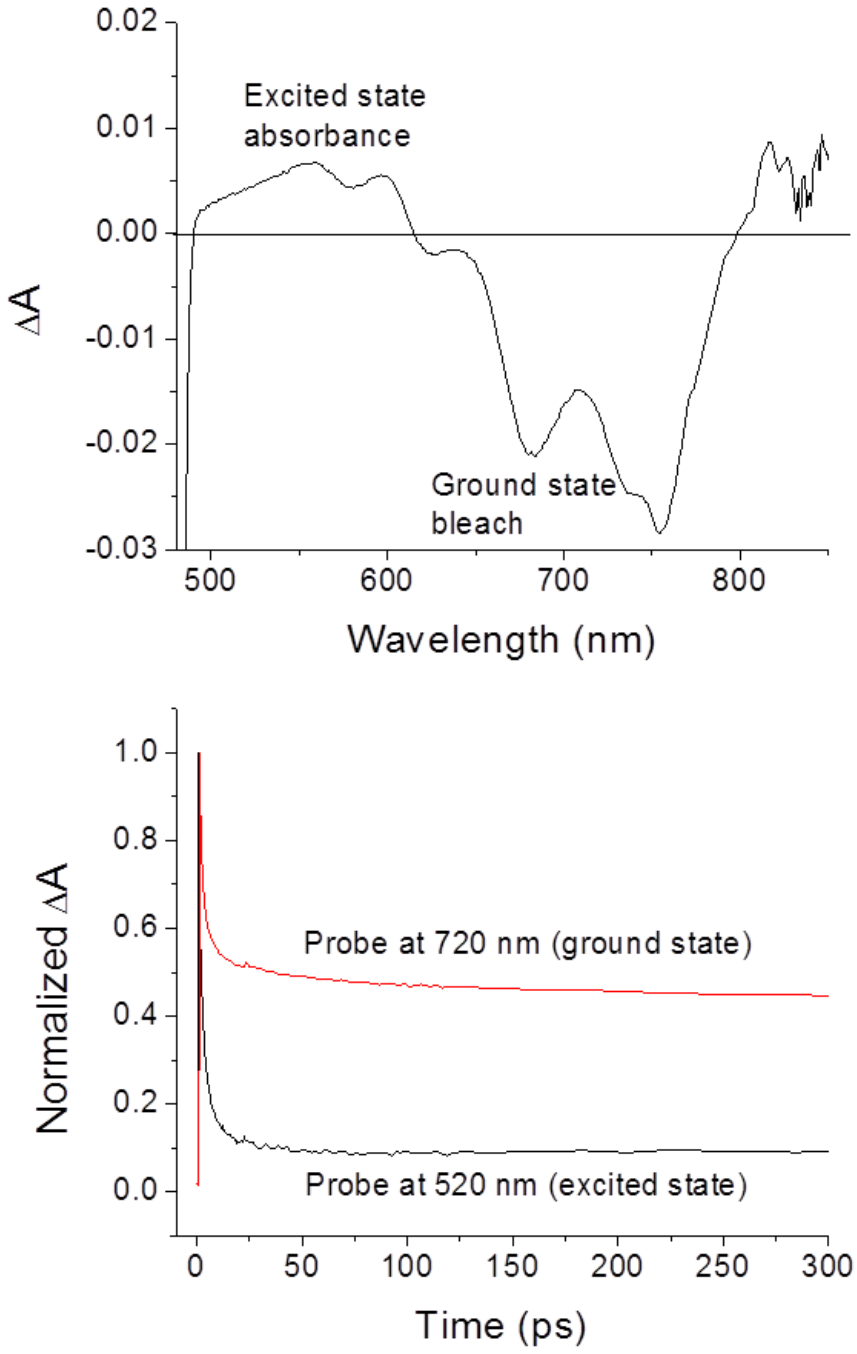

Figure 2-5. Excited state dynamics of DTS-CA. (Top) The transient absorption spectrum exhibits two peaks. The positive one is from the induced excited state absorption. The negative peak is the bleach of the ground state. (Bottom) Normalized decay curves for the ground state and excited states.

Table 2-4. Excited state lifetimes and injection efficiency for the dyes.

Dye	τ_{obs} Titania (ps)	τ_{obs} Alumina (ps)	η (%)	τ Injection (ps)
T-CA	1.8	123.9	98.5	1.82
T-PA	8.3	80.3	89.6	9.3
DTP-CA	1.0	14.1	97.6	1.1
DTP-PA	16.0	127.3	87.4	18.3
DTT-CA	19.8	3942	99.0	19.9
DTT-PA	19.1	32.3	41.0	46.7
DTS-CA	1.2	22.6	94.6	1.3
DTS-PA	4.0	18.5	78.6	5.1

Another striking change that we observe is that excited state lifetimes of the alkylated bridges (T, DTS) are much shorter than the alkylated ones (DTP, DTT). This suggests that there is a cost to including bulky antiaggregating agents. Perhaps the floppy side chains provide a faster vibrational relaxation for the excited state.

2.2.4 Charge Recombination Dynamics

Even after injection occurs, the electron's energy can be lost by recombination. In this process the electrolyte will oxidize the TiO_2 and the electron cannot be collected. This reduces both the J_{sc} (by reducing the number of electron that are collected) and the V_{oc} (by reducing the density of electrons in the TiO_2).[25, 28] We employed electrochemical impedance spectroscopy to study the rate of this process. The results are given in Table 2-5. These data were acquired in the dark with a bias of 0.64 V. This bias is applied to oppose the photovoltage generated under illumination. The peak frequency, *f*, is ascribed to charge transfer from the TiO_2 to the electrolyte.[1] A longer lifetime is better because it means that the electrolyte is less able to scavenge electrons from the TiO_2 leading to a greater number being collected at the anode. In all cases the PA dyes have slower scavenging than their CA analogues but the difference is greatest for the DTP and DTS bridges. Even though not directly involved in

recombination, the dye structure plays a big role. The dye molecules essentially provide an insulation of the TiO_2 surface from the electrolyte.[3] It would appear that a decrease in aggregation may result in faster recombination. Perhaps aggregates do a better job of protecting the TiO_2 surface because they are packed more closely.

Table 2-5. Peak frequencies (f) and calculated recombination lifetimes (τ) from impedance spectroscopy of devices assembled from the dyes.

Dyes	**T-CA**	**T-PA**	**DTP-CA**	**DTP-PA**	**DTT-CA**	**DTT-PA**	**DTS-CA**	**DTS-PA**
f (Hz)	21.3	16.7	27.7	11.0	25.6	11.2	17.5	9.9
τ (ms)	7.5	9.5	5.7	14.4	6.2	14.2	9.1	16.1

2.3 Conclusions

We analyzed a series of squaraine dyes with four different π-bridges and two anchoring groups. We measured how these structural changes impacted the optical, electronic, and kinetic properties of devices assembled from these dyes. The DTS bridge performed the best achieving a total efficiency of 8.9% when a carboxylic acid anchor was used. This dye had higher J_{sc} and V_{oc} than the others. We attributed these improvements to less dye aggregation. The corresponding phosphonic acid dye also outperformed its peers with an efficiency of 5.0%. This appears to be due to slower recombination. Transient absorption measurements were used to measure excited state dynamics. Generally, we observed that the phosphonic acid dyes had slower injection and shorter excited state lifetimes than their carboxylic acid analogues. This resulted in very poor injection efficiency for the PA dyes. We attribute this difference to greater aggregation of the phosphonic acid dyes and poor electronic overlap of the phosphonic acids and TiO_2. In their favor, the phosphonic acid dyes have slower

recombination than the carboxylic acid dyes. This may perhaps be due to the aggregates shielding the TiO_2 surface from the electrolyte.

2.4 Experimental

This project was part of a collaboration between numerous scientists. I will address, in detail, the work that I performed. For a detailed procedure for synthetic, optical, and electrochemical measurements please turn to the thesis work of Dr. Fadi Jradi of The Georgia Institute of Technology or the papers published containing these results.

2.4.1 Device Assembly

FTO slides were cleaned by sonication in a series of solutions for 15 minutes each. The solutions were Alconox, ethanol, and water. Finally, the slides were heated to 500 ^oC for 2 hours to remove all organics.

Platinized cathodes were prepared by drop coating a clean FTO slide with 3 drops of 0.1 M chloroplatinic acid in ethanol. After tilting the slide to evenly disperse the solution, the slide was heated to 400 ^oC for 20 minutes to leave a thin film of platinum metal.

The electrolyte consisted of consisted of 0.6 M 1,3-dimethylimidazolium iodide, 0.03 M iodine, 0.05 M LiI, 0.05 M guanidinium thiocyanate, and 0.5 M 4-tert-butylpyridine in 15/85 (v/v) mixture of valeronitrile and acetonitrile.

Dye solutions were prepared by dissolving the pure, solid dye in a viable anhydrous solvent (typically ethanol, tetrahydrofuran, or chloroform) to the desired concentration (0.01, 0.05, or 0.1 M). Chenodeoxycholic acid (CDCA) was added to a concentration of 0.1 M to reduce aggregation.

TiO_2 anodes were purchased from Solaronix item 74101. These consisted of a glass slide coated with FTO and a 10 μm thick layer of 20 nm TiO_2 nanospheres with a 4 μm thick

layer of 200 nm TiO_2 nanospheres. This first layer is for dye adsorption while the second is to increase light scattering to increase the effective path length of incident photons on the cell. The area of the cell coated with TiO_2 was 0.36 cm^2. These anodes were placed in a 0.2 M solution of $TiCl_4$ in water and heated to 70 °C for 30 minutes to lay down a thin blocking layer of dense TiO_2. Skipping this step results in poor contact between the TiO_2 nanoparticles and electrolyte contact with the FTO – scavenging increases resultantly. The anodes were removed from the solution and gently rinsed with water before being heated to 450 °C for 2 hours (heating/cooling rate = 2 °C/min).

After cooling to 80 °C, the anodes were immersed in the dye solution for 12 hours. Allowing the anodes to cool to room temperature before immersion decreases efficiency because water is allowed to bind to the TiO_2 which increases dye desorption. The anodes were removed and gently rinsed with acetonitrile and dried by a stream of nitrogen. The cells were immediately assembled by sandwiching a 60 μm Surlin spacer between the anode and cathode. The spacer had a hole large enough to accommodate the TiO_2 active area. To binder clips held the assembly together. Electrolyte was added by placing a drop near the active area, removing one binder clip, and gently separating the cathode and anode by a few millimeters. Capillary action drew the electrolyte into the cell and the clip was replaced giving a temporary seal.

2.4.2 PCE and IPCE Measurements

The air mass (AM) 1.5-irradiance of 100 mW / cm^2 was provided by a solar simulator, which consisted of a 300 W xenon light source (Oriel, U.S.A.) and an optical shutter connected to Keithley meter which was automated with an I-V station from Newport. The light intensity was calibrated with a silicon diode reference cell 91150V (Oriel, U.S.A.). The mismatch between the simulated and the true solar spectra was corrected with the light filter 81094 (Oriel, U.S.A.). The current-voltage performance of the cell under these conditions were tested

with four-wire connection mode by sourcing external potential bias to the cell and measuring the generated photocurrent with a Keithley 2400 digital source meter. The test results were acquired with Oriel IV test station software. The incident photon-to-electron conversion efficiency (IPCE) was characterized by using Oriel Quantum Efficiency Measurement Kit, consisted of a 300 W xenon lamp, Merlin lock-in amplifier, Cornerstone 260 monochromator and a silicon detector. The measuring process was automated with TracQ software from Newport.

2.4.3 Transient Absorption Spectroscopy

Sub picosecond pump and probe laser pulses were generated with a Coherent Libra-HE regenerative-amplified Ti:sapphire laser system. The basic pulse compression unit generates 4 mJ, sub-50 ps pulses of 808 nm-centered light at 1 kHz. Approximately 60% of this beam was directed into a Coherent OPerA Solo Ultrafast optical parametric amplifier. This computer controlled OPA was tuned to produce visible light pump pulses at a specific wavelength between 500 and 760 nm. Every other pump pulse was blocked by an optical chopper. For use as a probe, 5% of the original 800 nm beam was directed through a delay stage and then through a sapphire crystal producing a super continuum spectrum ranging from 450 to 820 nm. The two beams were focused and overlapped on the assembled full cells. The $1/e^2$ radii of the pump and probe beams were 900 ± 50 nm and 300 ± 25 nm, respectively. The transmitted portion of the probe beam was collected by a fiber optic cable and Si array detector. ΔA was calculated as a function of delay time by comparing the transmitted probe beam when the pump beam was and was not blocked by the chopper.

For transient absorption measurements, sample preparation was varied from the standard device assembly. Since charge collection was unnecessary, no FTO coated glass was used. TiO_2 films were prepared by doctor blading a layer of TiO_2 nanoparticles (Solaronix

20 nm TiO_2) onto a clean glass microscope slide. The doctor blading guide was simply a piece of Scotch tape with a ¼ inch hole punched out with a hole punch. The film was annealed at 500 °C for 1 hour. Unplatinized glass was used for the "cathode" side and the normal electrolyte was employed.

Alumina films were prepared similarly from an aluminum oxide/hydroxide paste. The paste was prepared by dissolving 100 mg of aluminum isopropoxide in 9 mL of water and 1 mL of HCl. The solution was slowly evaporated until the alumina began to gel into a thick transparent paste.

2.5 References

1. Yum, J. H.; Walter, P.; Huber, S.; Rentsch, D.; Geiger, T.; Nuesch, F.; De Angelis, F.; Gratzel, M.; Nazeeruddin, M. K., Efficient far red sensitization of nanocrystalline TiO2 films by an unsymmetrical squaraine dye. *Journal of the American Chemical Society* **2007,** *129* (34), 10320-+.

2. Shockley, W.; Queisser, H. J., Detailed balance limit of efficiency of p-n junction solar cells. *Journal of applied physics* **1961,** *32* (3), 510-519.

3. Chiba, Y.; Islam, A.; Watanabe, Y.; Komiya, R.; Koide, N.; Han, L., Dye-sensitized solar cells with conversion efficiency of 11.1%. *Japanese Journal of Applied Physics* **2006,** *45* (7L), L638.

4. Yen, Y.-S.; Chou, H.-H.; Chen, Y.-C.; Hsu, C.-Y.; Lin, J. T., Recent developments in molecule-based organic materials for dye-sensitized solar cells. *J. Mater. Chem.* **2012,** *22* (18), 8734-8747.

5. Wiberg, J.; Marinado, T.; Hagberg, D. P.; Sun, L.; Hagfeldt, A.; Albinsson, B., Effect of Anchoring Group on Electron Injection and Recombination Dynamics in Organic Dye-Sensitized Solar Cells. *J. Phys. Chem. C* **2009,** *113* (9), 3881-3886.

6. Sreejith, S.; Carol, P.; Chithra, P.; Ajayaghosh, A., Squaraine dyes: a mine of molecular materials. *Journal of Materials Chemistry* **2008,** *18* (3), 264-274.

7. Gundlach, L.; Szarko, J.; Socaciu-Siebert, L. D.; Neubauer, A.; Ernstorfer, R.; Willig, F., Different orientations of large rigid organic chromophores at the rutile TiO_2 surface controlled by different binding geometries of specific anchor groups. *Phys. Rev. B: Condens. Matter Mater. Phys.* **2007,** *75* (12), 125320.

8. Wang, P.; Klein, C.; Moser, J.-E.; Humphry-Baker, R.; Cevey-Ha, N.-L.; Charvet, R.; Comte, P.; Zakeeruddin, S. M.; Grätzel, M., Amphiphilic ruthenium sensitizer with 4, 4 '-diphosphonic acid-2, 2 '-bipyridine as anchoring ligand for nanocrystalline dye sensitized solar cells. *The Journal of Physical Chemistry B* **2004,** *108* (45), 17553-17559.

9. Murakami, T. N.; Yoshida, E.; Koumura, N., Carbazole dye with phosphonic acid anchoring groups for long-term heat stability of dye-sensitized solar cells. *Electrochim. Acta* **2014,** *131* (0), 174-183.

10. Mulhern, K. R.; Orchard, A.; Watson, D. F.; Detty, M. R., Influence of Surface-Attachment Functionality on the Aggregation, Persistence, and Electron-Transfer Reactivity of Chalcogenorhodamine Dyes on TiO2. *Langmuir* **2012,** *28*, 7071-7082.

11. Mishra, A.; Fischer, M. K. R.; Bauerle, P., Metal-Free Organic Dyes for Dye-Sensitized Solar Cells: From Structure: Property Relationships to Design Rules. *Angew. Chem., Int. Ed.* **2009,** *48* (14), 2474-2499.

12. Hagfeldt, A.; Boschloo, G.; Sun, L. C.; Kloo, L.; Pettersson, H., Dye-Sensitized Solar Cells. *Chem. Rev.* **2010,** *110* (11), 6595-6663.

13. Kalyanasundaram, K.; Gratzel, M., Applications of functionalized transition metal complexes in photonic and optoelectronic devices. *Coord. Chem. Rev.* **1998,** *177*, 347-414.

14. de Miguel, G.; Marchena, M.; Cohen, B.; Pandey, S. S.; Hayase, S.; Douhal, A., Relating the Photodynamics of Squaraine-Based Dye-Sensitized Solar Cells to the Molecular Structure of the Sensitizers and to the Presence of Additives. *J. Phys. Chem. C* **2012,** *116* (42), 22157-22168.

15. Lanzafame, J. M.; Muenter, A. A.; Brumbaugh, D. V., The effect of J-aggregate size on photoinduced charge transfer processes for dye-sensitized silver halides. *Chemical physics* **1996,** *210* (1), 79-89.

16. Khairutdinov, R.; Serpone, N., Photophysics of cyanine dyes: Subnanosecond relaxation dynamics in monomers, dimers, and H-and J-aggregates in solution. *The Journal of Physical Chemistry B* **1997,** *101* (14), 2602-2610.

17. Feldt, S. M.; Gibson, E. A.; Gabrielsson, E.; Sun, L.; Boschloo, G.; Hagfeldt, A., Design of organic dyes and cobalt polypyridine redox mediators for high-efficiency dye-sensitized solar cells. *Journal of the American Chemical Society* **2010,** *132* (46), 16714-16724.

18. Wang, Z.-S.; Cui, Y.; Dan-oh, Y.; Kasada, C.; Shinpo, A.; Hara, K., Thiophene-functionalized coumarin dye for efficient dye-sensitized solar cells: electron lifetime improved by coadsorption of deoxycholic acid. *The Journal of Physical Chemistry C* **2007,** *111* (19), 7224-7230.

19. Chen, H.; Law, K.-Y.; Whitten, D. G., Aggregation of Amphiphilic Squaraines at the Air− Water Interface and in Langmuir− Blodgett Films. *The Journal of Physical Chemistry* **1996,** *100* (14), 5949-5955.

20. Ehret, A.; Stuhl, L.; Spitler, M., Spectral Sensitization of TiO~ 2 Nanocrystalline Electrodes with Aggregated Cyanine Dyes. *Journal of Physical Chemistry B* **2001,** *105* (41), 9960-9965.

21. Mathew, S.; Yella, A.; Gao, P.; Humphry-Baker, R.; Curchod, B. F. E.; Ashari-Astani, N.; Tavernelli, I.; Rothlisberger, U.; Nazeeruddin, M. K.; Gratzel, M., Dye-sensitized solar cells with 13% efficiency achieved through the molecular engineering of porphyrin sensitizers. *Nature Chem.* **2014,** *6* (3), 242-247.

22. Tachibana, Y.; Haque, S. A.; Mercer, I. P.; Durrant, J. R.; Klug, D. R., Electron injection and recombination in dye sensitized nanocrystalline titanium dioxide films: a comparison of ruthenium bipyridyl and porphyrin sensitizer dyes. *The Journal of Physical Chemistry B* **2000,** *104* (6), 1198-1205.

23. Tachibana, Y.; Haque, S. A.; Mercer, I. P.; Moser, J. E.; Klug, D. R.; Durrant, J. R., Modulation of the Rate of Electron Injection in Dye-Sensitized Nanocrystalline TiO. *The Journal of Physical Chemistry B* **2001,** *105* (EPFL-ARTICLE-164398), 7424-7431.

24. Huang, S.; Schlichthörl, G.; Nozik, A.; Grätzel, M.; Frank, A., Charge recombination in dye-sensitized nanocrystalline TiO2 solar cells. *The Journal of Physical Chemistry B* **1997,** *101* (14), 2576-2582.

25. Nazeeruddin, M. K.; Péchy, P.; Renouard, T.; Zakeeruddin, S. M.; Humphry-Baker, R.; Comte, P.; Liska, P.; Cevey, L.; Costa, E.; Shklover, V., Engineering of efficient panchromatic sensitizers for nanocrystalline TiO2-based solar cells. *Journal of the American Chemical Society* **2001,** *123* (8), 1613-1624.

26. Mathew, S.; Yella, A.; Gao, P.; Humphry-Baker, R.; CurchodBasile, F. E.; Ashari-Astani, N.; Tavernelli, I.; Rothlisberger, U.; NazeeruddinMd, K.; Grätzel, M., Dye-sensitized solar cells with 13% efficiency achieved through the molecular engineering of porphyrin sensitizers. *Nat Chem* **2014,** *6* (3), 242-247.

27. Murakami, T. N.; Koumura, N.; Uchiyama, T.; Uemura, Y.; Obuchi, K.; Masaki, N.; Kimura, M.; Mori, S., Recombination inhibitive structure of organic dyes for cobalt complex redox electrolytes in dye-sensitised solar cells. *Journal of Materials Chemistry A* **2013,** *1* (3), 792-798.

28. Velusamy, M.; Justin Thomas, K.; Lin, J. T.; Hsu, Y.-C.; Ho, K.-C., Organic dyes incorporating low-band-gap chromophores for dye-sensitized solar cells. *Organic Letters* **2005,** *7* (10), 1899-1902.

CHAPTER 3 – PORPHYRIN-SQUARAINE DYES FOR PANCHROMATIC DYE SENSITIZED SOLAR CELLS

3.1 Introduction

Silicon and other semiconductors have broad absorption spectra which allow them to efficiently harvest all photons above their band gap energies. Molecular dyes tend to be good at absorbing photons in a relatively small region. Overcoming this problem necessitates the development of panchromatic sensitizers which can absorb light up to around 940 nm. Early work with ruthenium-based dyes yielded molecules with strong absorption into the near-IR.[4] But ruthenium is rare and expensive so replacing ruthenium sensitizers with an organic dye could reduce the cost of DSSCs.

There are a wide number of organic chromophores to choose from including as indolines[2], triarylamines[3], squaraines (Sq)[4], and porphyrins (Por)[2]. A porphyrin sensitizer currently holds the efficiency record for DSSCs at 13%.[5] These dyes typically have molar absorptivities in the 50,000-500,000 $M^{-1}cm^{-1}$ range in comparison with ~5,000 $M^{-1}cm^{-1}$ for ruthenium dyes. These photon absorbing properties originate in the strong transition dipole of π-π^* transitions between the ground state and first excited state. Though strong, these transitions are narrow and make it difficult to achieve panchromicity. Researchers have explored a number of solutions: 1) using multiple dyes in a single cell[6]; 2) covalently linking multiple chromophores into a single large dye[5, 7-8]; 3) Förster resonant energy transfer from unbound chromophores in solution to tethered sensitizers; and 4) chlorophyll-like antennae

attached to the chromophores to improve absorption. Option 1 has yielded cells with power conversion efficiencies (PCEs) over 10%.[9]

These solutions improve PCE by allowing the cells to capture a greater percentage of solar photons and so increase photocurrent without sacrificing cell voltage. An ideal cell would be able to absorb photons in the region from 400 to 940 nm where most of the energy of the solar spectrum lies.[12] If a sensitizer could absorb 100% of all photons below 920 nm, it could achieve a short-circuit photocurrent (J_{sc}) of 33 mA/cm^2 under normal test conditions.[10] This is double what the best organic sensitizers achieve so there is clearly plenty of room for improvement.[11-12]

Capturing the near IR photons is especially important. A dye with an absorption onset of 900 nm would have a 20% higher J_{sc} than one with an onset of 800 nm. Squaraines and phthalocyanines[10-12] perform particularly well in the red to infrared region with squaraines achieving absorptivities around 10^5 M^{-1}cm^{-1} above 650 nm. Thus, pairing squaraines with dyes that absorb high energy photons is an intriguing possibility. Other grounds have reported squaraines modified with bridges to the anchor group that can absorb high energy photons. Others have positioned the additional chromophore on the back side of the squaraine.[10]

Porphyrins make an excellent complement to squaraines in multichromophoric systems. Their absorption spectrum is characterized by a strong, sharp Soret band between 400 and 450 nm and a series of Q bands which form a broad absorption between 500 and 700 nm.[13] The absorptivities for these bands are around 10^5 M^{-1}cm^{-1} and 10^4 M^{-1}cm^{-1} respectively. This fills in the high energy gap in a typical squaraine sensitizer. Combining sensitizers can have unintended consequences including absorption shifts[14], the enhancement of two-photon processes[15], and challenging charge/energy transfer. We employed an acetylene bridge because these types of linkers have been shown to allow unidirectional flow from

porphyrins to squaraines.[13] By putting the squaraine closer to the TiO_2, we can increase the odds of efficient charge injection.

The structures of the dyes studied in this chapter are shown in Figure 3-1. The dye series features a zinc porphyrin conjugated to a squaraine through an acetylene which is attached to a bridge group attached to a cyanoacetic acid (CA) anchoring group. The *meta* positions on the phenyl rings of the porphyrins have either *tert*-butyl or trihexylsilyl groups. The indolines of the squaraines have either ethyl or dodecyl alkyl chains. The purposes of these bulky groups are to prevent the formation of H-aggregates upon adsorption on TiO_2. Two different bridge groups were explored: dithienosilol (DTS) and thiophene (T). The bridge group acts as a third chromophore with absorption in the UV-blue region. The behavior of these dyes will be discussed in comparison to two dyes of the previous chapter (T-CA and DTS-CA) and their structures are included for reference.

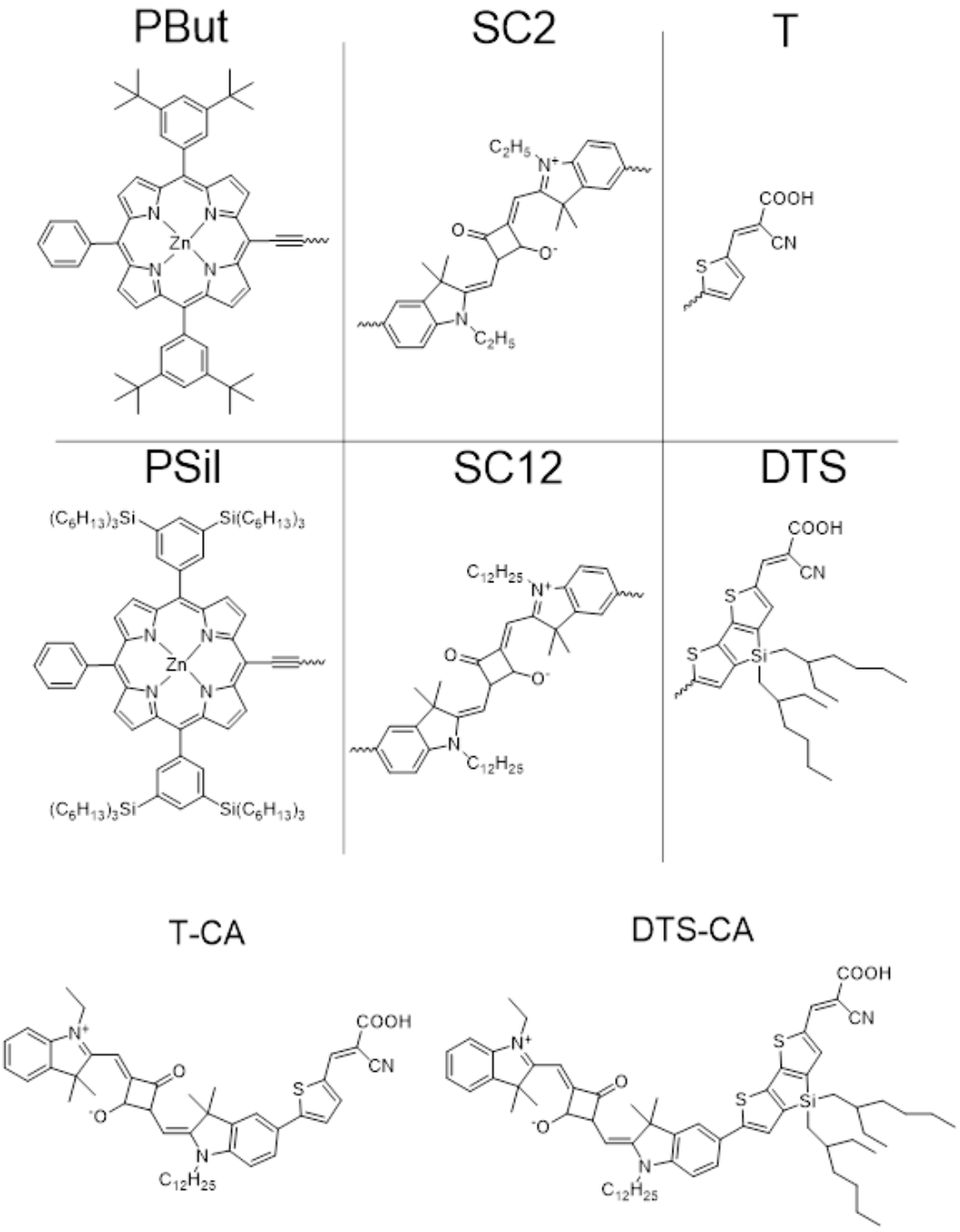

Figure 3-1. Structures of the dye molecules discussed in this chapter. The hybrid porphyrin-squaraine dyes are constructed out of the six fragments at the top – one each of PBut/PSil, SC2/SC12, and T/DTS.

3.2 Results and Discussion

Collaboration note: Synthesis of the dyes was conducted by Dr. Fadi Jradi of the Marder group at Georgia Tech and Dr. Jinsze Wong of the Anderson group at Oxford. Dr. Jradi conducted the electrochemical measurements Dr. Xiongwu Kang of the El-Sayed group at Georgia Tech assembled the photovoltaic devices and performed the IV measurements. I performed all dynamics measurements, assembled some of the devices and performed IV measurements.

Porphyrins typically have two main features in their absorption spectra: a low intensity Q-band in the 500-650 nm region and an intense Soret band around 400-450 nm. Squaraines have their main absorption peak around 650 nm. Figure 3-2 shows the absorption spectra of the Por-Sq dyes in comparison to their component squaraine T-CA. The squaraine band of PBut-SC12-T is red shifted 80 nm to around 720 nm. The porphyrin Soret band also fills in the absorption from 400 to 500 nm (overlapping with the thiophene absorption). PBut-SC2-T and PBut-SC12-T show the change upon increasing the alkyl chain on the indole groups from ethyl to dodecyl.

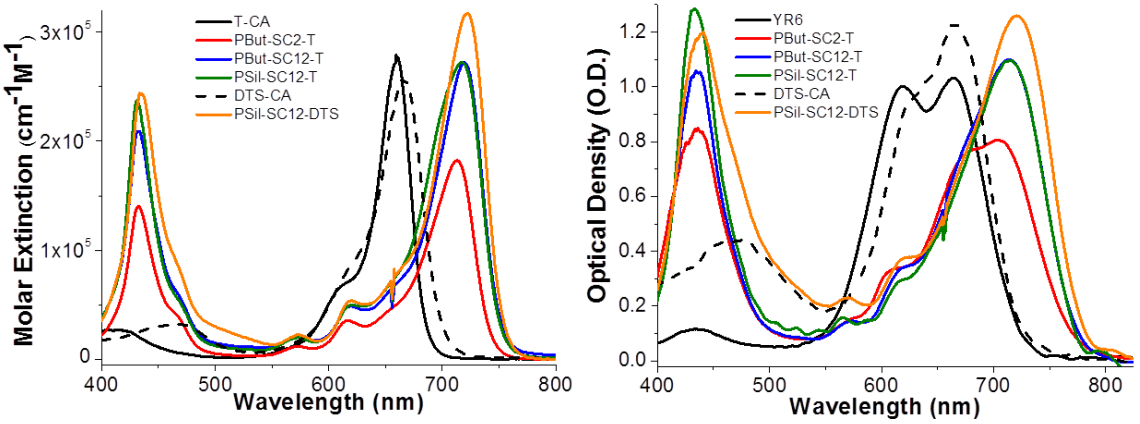

Figure 3-2. (Left) Molar extinction spectra for the dyes in THF. (Right) Absorbance measurements for the dyes adsorbed on titania. The titania films were soaked for 1 hour In solutions with 0.05 mM dye and 10 mM CDCA.

The spectra look similar with only a slight blue-shift of the absorption of PBut-SC12-T (which also has a much stronger absorption overall). Changing the π-bridge from thiophene (PSil-SC12-T) to dithiophene (PSil-SC12-DTS) causes a red shift of both the squaraine and porphyrin bands by 5 nm. The DTS bridge adds a little extra absorption in the blue-green region as well.

Figure 3-2 also shows the absorption of these dyes when adsorbed on TiO_2. Upon adsorption a blue shifting of the peaks was typically observed due to the formation of H-aggregates. A broadening on all peaks to higher energy was observed.[5,24] However, the extent of broadening varied depending upon the length of the alkyl chains on the indole. PBut-SC2-T exhibited a much broader squaraine absorption than PBut-SC12-T indicating that the longer alkyl chains help prevent the formation of aggregates. Curiously moving from butyl groups on the porphyrin (PBut-SC12-T) to hexylsilyl groups (PSil-SC12-T) had almost no effect on aggregation: these dyes exhibited nearly identical spectra. The increased absorption of PSil-SC12-DTS relative to PSil-SC12-T between 480-550 nm is attributed to the DTS bridge.

To explore the energy levels in these dyes we determined the ground-state oxidation potentials ($E_{S+/S}$) and the excited-state oxidation potentials (E_{S+/S^*}) (Table 3-1). The excited state oxidation potential must be higher than the conduction band edge (CBE) of TiO_2 or else injection will not occur efficiently. For bare TiO_2, the CBE is around -0.5 V vs NHE[30,31] although this can vary with surface modification[16], lithium ions[17], pH[18], and doping[14]. As such, it is generally thought that E_{S+/S^*} should be no less than -0.8 vs NHE to ensure fast injection. The addition of the porphyrin chromophore dropped the excited state potential from around -0.95 to -0.83: having the potential to slow injection.[19] On the other side of the cell, $E_{S+/S}$ must lie below the redox potential of the electrolyte (0.30 V vs NHE for I^-/I_3^-). All dyes have potentials in excess of 0.8 V vs NHE giving more than enough driving force for regeneration.

However, we do observe that this value is shifted by about 500 mV for the Por-Sq dyes relative to the parent porphyrin dyes.

Table 3-1. Optical and electronic properties of the dyes. The difference between ground and excited state energies was determined by the absorption and fluorescence spectra. The ground state reduction potential was determined by cyclic voltammetry. The excited state oxidation potential was calculated from these two values.

Dyes	**λ_{max} (nm)**	**ε ($M^{-1}cm^{-1}$)**	E_{0-0}^{opt} **(eV)**	$E_{(S^+/S)}$ **(V)**	$E_{(S^+/S^*)}$ **(V)**
T-CA	659	279,000	1.76	+0.80	-0.96
PBut-SC2-T	718	182,000	1.72	+0.90	-0.82
PBut-SC12-T	713	246,000	1.72	+0.88	-0.84
PSil-SC12-T	717	272,000	1.72	+0.89	-0.83
DTS-CA	657	257,000	1.82	+0.84	-0.98
PSil-SC12-DTS	722	317,000	1.72	+0.89	-0.83

3.2.1 Photovoltaic Measurements

We assembled fully operational cells with these dyes using the standard procedures for dye sensitized solar cells. We have found that it is essential to include chenodeoxycholic acid (CDCA) as a co adsorbent with the dyes. As other grounds have pointed out, the CDCA binds to the TiO_2 and helps to prevent aggregation. The ratio of dye and CDCA concentrations are shown in

Table 3-2. The incident photon to current efficiency (IPCE) spectra of the dyes are shown in Figure 3-3. Electrical measurements of the devices. (Left) The incident photons to current efficiency (IPCE) spectra. (Right) Current-voltage curves for each dye.. The IPCE curves show the same general trends as seen in the absorption spectra – this makes intuitive sense because the regions where the dyes absorb well will also be areas of high quantum

efficiency. The porphyrin dyes have improved IPCE in the 450-550 nm region due to the absorption from the Soret-band. All of these (except PBut-SC2-T) have an IPCE cutoff 50 nm redder than DTS-CA. This is in line with the goal of producing panchromatic dyes which absorb into the near infrared. It is suspected that PBut-SC2-T failed to achieve this same red shifting of IPCE because its short ethyl chains on the indole groups (compared to the hexyldecyl chains on the other dyes) failed to prevent aggregation. H-aggregates have blue shifted absorptions in line with this finding. PBut-SC12-T and PSil-SC12-T have very similar IPCE spectra although the former does have a slightly higher spectrum. This suggests that the R groups on the porphyrin makes little difference in performance. Compared to T-CA both PBut-SC12-T and PSil-SC12-T have better IPCE spectra. Their onset is almost 100 nm to the red of the squaraine only dye. One curious deviation between the IPCE spectra and the absorption spectra is for PSil-SC12-DTS. In the IPCE, the 400-600 nm region shows better efficiency than the 600-850 nm region. This, despite the fact that absorbances of the two regions are similar (the other porphyrin dyes to not exhibit this trend). We propose that this may be due to variable injection rates from different excited states. The higher energy excited state of the DTS group may inject faster than the absorption localized on the porphyrin. This could either be due to a larger driving force or better spatial overlap with the TiO_2. This mechanism has been observed for vibrationally "hot" electrons in ruthenium dyes.[20-21] Why this does not affect the other porphyrin dyes is an interesting question. It may simply be that the excited states of all the dyes are close to the minimum energy needed for efficient injection and the PSil-SC12-DTS is simply a bit lower than the others.

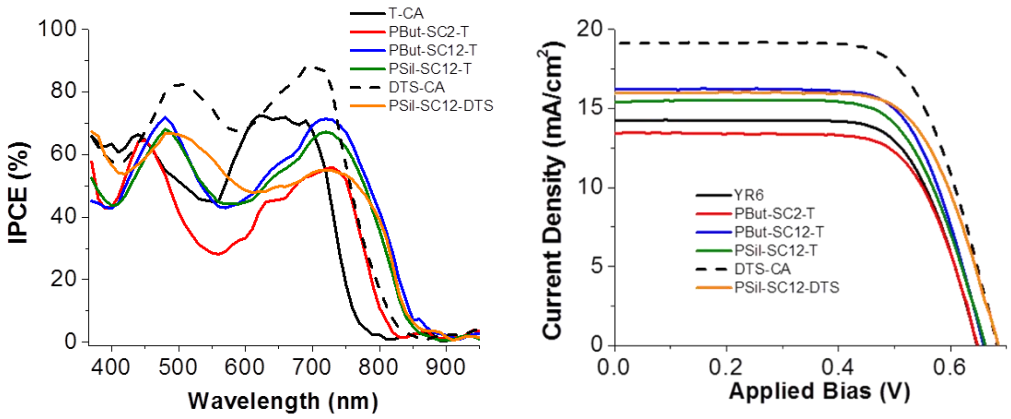

Figure 3-3. Electrical measurements of the devices. (Left) The incident photons to current efficiency (IPCE) spectra. (Right) Current-voltage curves for each dye.

Turning to the electrical measurements from the cells we see some interesting trends. PBut-SC2-T exhibits lower PCE and J_{sc} than T-CA but an identical V_{oc}. The loss in current is likely due to the significant aggregation suggested by the blue shift present on TiO_2. Another possibility is that the dye simply has worse injection than T-CA which could either be due to nonradiative losses associated with aggregation or slower injection due to a lower excited state reduction potential. By comparison, PBut-SC12-T and PSil-SC12-T both outperform their parent dye T-CA. PBut-SC12-T has a PCE of 7.5% compared to 6.5%, a similar V_{oc} and a much higher J_{sc}. This higher current is likely due to the broader absorption spectrum which better aligns with the solar spectrum.

The trihexylsilyl group on the porphyrin improves the photovoltage by about 30 mV relative to the porphyrin dyes with tert-butyl. This may be caused by superior insulation of the TiO_2 surface from the electrolyte. By blocking the electrolyte from approaching the surface, charge recombination can be retarded. This steric shielding effect has been observed by other groups.

Although an improvement over T-CA is seen upon the addition of a porphyrin chromophore, no improvement was seen for DTS-CA. Although PSil-SC-12-DTS did better than the other Por-Sq dyes, it did not exceed the PCE of DTS-CA. This was mainly due to poor injection efficiency as will be shown in the next section.

Table 3-2. Soaking solution concentrations and photovoltaic properties of the dyes.

Dyes	Dye Conc. (mM)	CDCA Conc. (mM)	V_{oc} (V)	J_{sc} (mA/cm^2)	FF (%)	PCE (%)
T-CA	0.1	10	0.65 ± 0.01	14.2 ± 0.3	70.4 ± 0.2	6.5 ± 0.1
PBut-SC2-T	0.1	10	0.65 ± 0.01	13.4 ± 0.1	70.4 ± 0.8	6.1 ± 0.1
PBut-SC12-T	0.05	10	0.66 ± 0.01	16.3 ± 0.4	70.1 ± 0.6	7.5 ± 0.1
PSil-SC12-T	0.05	10	0.65 ± 0.01	15.2 ± 0.1	71.2 ± 0.3	7.1 ± 0.1
DTS-CA	0.05	10	0.68 ± 0.01	19.1 ± 0.2	68.3 ± 0.7	8.9 ± 0.2
PSil-SC12-DTS	0.1	10	0.69 ± 0.01	16.0 ± 0.2	69.6 ± 0.7	7.6 ± 0.1

3.2.2 Injection Measurements

To get a better understanding of how the energy levels and structures of these dyes relate to their performance, we measured the injection efficiency of these dyes. Using ultrafast transient absorption measurements we can track the excited state lifetimes of the dyes. For ruthenium dyes, injection is very efficient – near 100%. Squaraines, porphyrins, and other organic dyes tend to have less efficient injection as other pathways compete with injection. To study their relative rates, we measured the excited-state lifetime of the dyes adsorbed on TiO_2 and Al_2O_3 in fully assembled devices. The conduction band energy of alumina is too high for injection so it provides a control that allows us to measure the excited state dynamics of the dyes in the absence of the injection pathway.

To follow the excited state dynamics we looked at the decay of the transiently induced excited state peak (typically between 475 nm to 550 nm). The data was fit using the stretched exponential function.

$$f(t) = A \exp\left[\left(-\frac{t}{\tau}\right)^{\beta}\right] \quad (1)$$

A is a scaling constant, τ is the characteristic lifetime, and β is a measure of heterogeneity that accounts for variations in the lifetime of adsorbed dyes. Different dyes have different βs and so for the ease of comparison, a weighted τ_{obs} may be calculated.

$$\tau_{obs} = \frac{\tau}{\beta}\Gamma\left(\frac{1}{\beta}\right) \quad (2)$$

Where Γ is the gamma function.

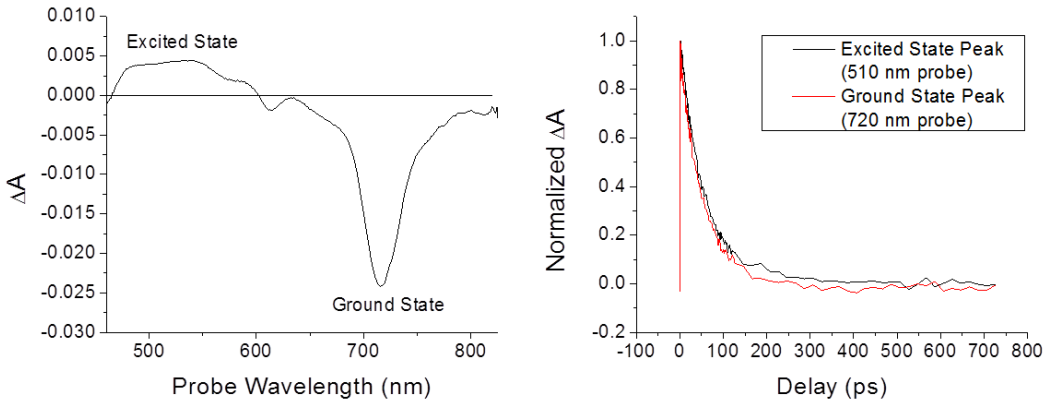

Figure 3-4. Excited state dynamics of PBut-SC2-T when excited at 720 nm in THF. (Left) The transient absorption spectrum shows a positive peak at high energy assigned to the excited state. The large negative peak around 720 nm is due to the scattered pump light overlapping with a negative ground state bleach. (Right) The dynamics of the ground state and excited state peaks are almost identical.

Multichromophoric dyes present a bit of a challenge when studying excited state dynamics. There will be multiple excited states accessible by visible light absorption which have different spatial distributions within the molecule. It is not unreasonable to think that

these excited states could have different injection rates. Indeed, the IPCE data from PSil-SC12-T suggests that the lowest lying excited state could indeed have poor injection efficiency. Figure 3-4 shows the behavior of PBut-SC2-T when excited at 720 nm in solution. This pump wavelength is only capable of exciting the squaraine chromophore as such the excited state behavior is expected to be very similar to a squaraine-only dye. This is indeed what is seen. There is an excited state bleach at high energy (480 to 600 nm) and a ground state bleach from 650 to 800 nm. This low energy peak overlaps with the scattered light at 720 nm. This assignment is confirmed by the identical transient kinetics of the two peaks.

To examine the effect of aggregation on excited state behavior we adsorbed PBut-SC2-T on alumina. We varied the pump power from 10 μW to 1000 μW and followed the excited state lifetime with a 532 nm probe (Figure 3-5). The following biexponential function was used to fit the data:

$$y = A_1 e^{-t/1\,ps} + A_2 e^{-t/75\,ps} \quad (3)$$

The two terms represent two different types of decay present in the sample 1) the slow decay is due to vibrational relaxation and 2) the fast decay is due to nonlinear loss pathways. We can tell that the fast decay is due to a nonlinear process because its relative weight increases with power. This means that as the number of excitons increases in the sample, the more important this pathway becomes. This type of behavior is consistent with exciton-exciton annihilation.[22-23]

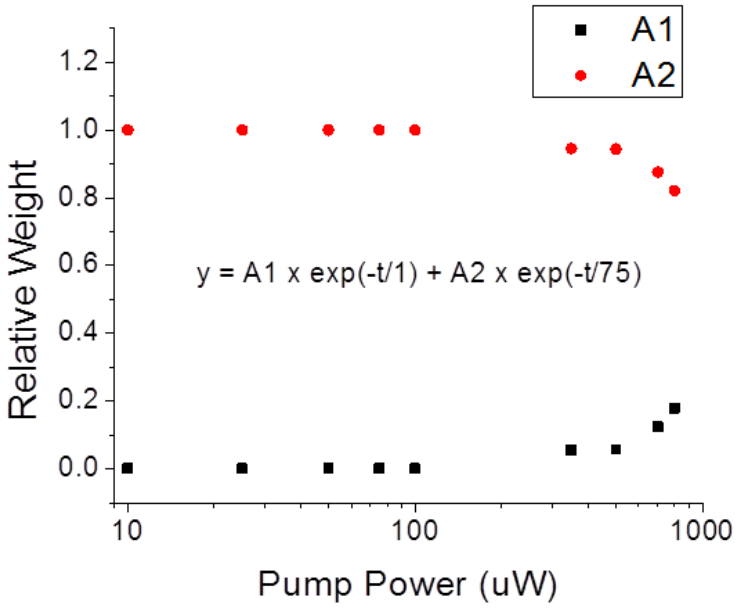

Figure 3-5. Excited state dynamics of PBut-SC2-T adsorbed on alumina. The dye was excited at 720 nm and probed at 532 nm. The data was fit using a biexponential with time constants 75 ps and 1 ps. The relative weight of the two terms is plotted. The excited state decay sped-up with increasing power.

The porphyrin-squaraine dyes have two separate chromophores so it is important to understand how these interact. PBut-SC12-T was deposited on TiO_2 and pumped at 470, 575 630, 705 nm. The results from this experiment are shown in Figure 3-6. The transient decays show the excited state decay measured at 520 nm. All the pump wavelengths show the same kinetics indicating that the injection rate is invariant with the pump wavelength. This suggests one of two possibilities 1) injection occurs from all excited states equally quickly or 2) the higher excited states (S_n) quickly relax to the lowest excited state (S_1) before injection. To further understand, we may examine the excited state spectra. All pump wavelengths exhibit very similar excited state spectra with the possible exception of 470 nm. This produces a broadly similar spectrum although the excited state peak is somewhat shifted around 500 nm. This could indicate the presence of a different, short lived excited state which quickly transfers

energy to S_1. It is quite likely that injection is not even possible from the porphyrin-based orbitals since they simply are too far from the TiO_2. This conclusion is supported by the fluorescence data in Figure 3-6. The fluorescence spectrum of the dye looks the same regardless of the excitation wavelength. This is in good agreement with Kasha's rule which states that fluorescence only occurs from S_1 of a chromophore because all the higher excited states quickly relax to S_1.

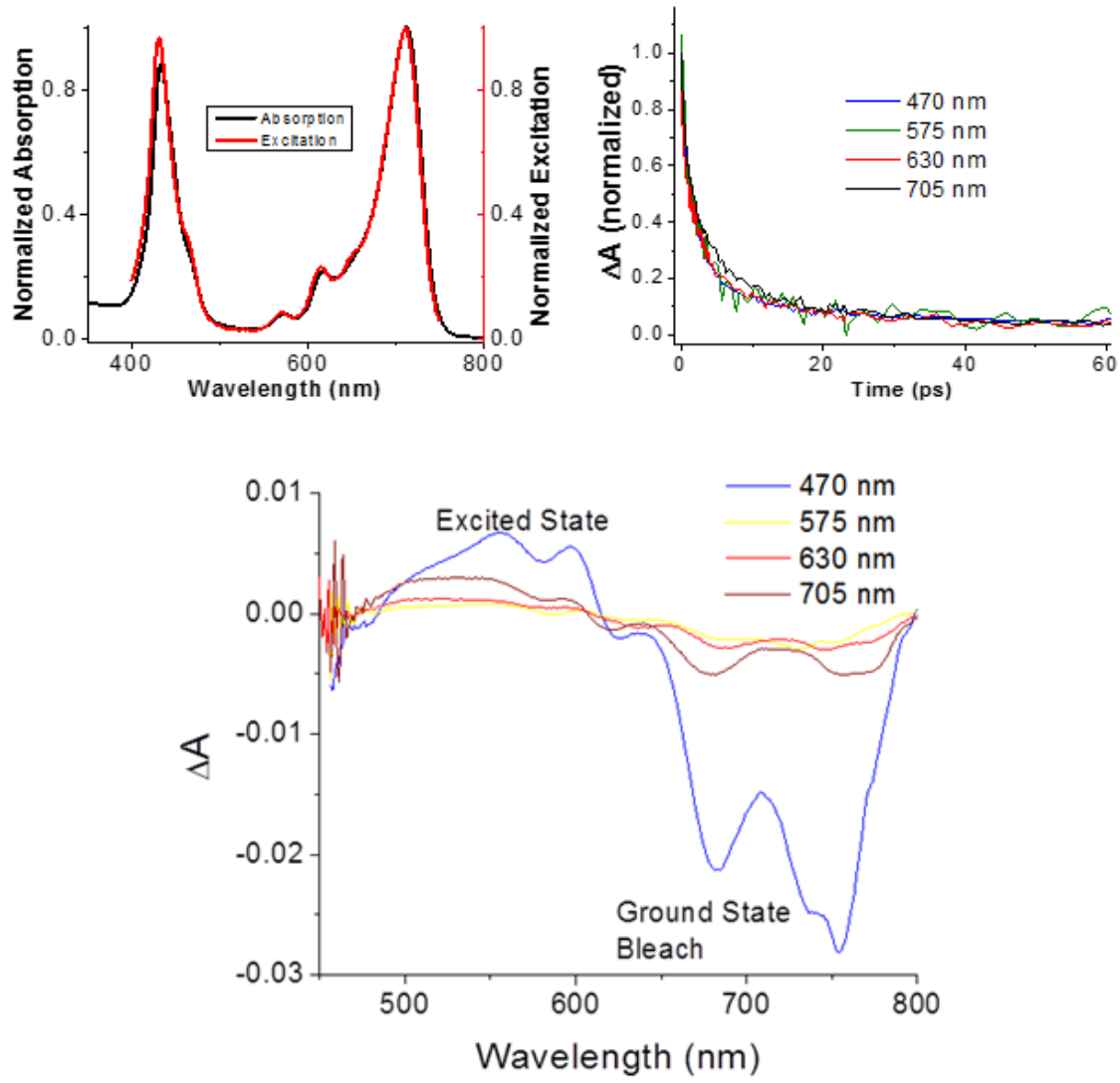

Figure 3-6. (Left) Absorption and excitation fluorescence spectra for PBut-SC21-T. Emission measured at 765 nm. (Right) Transient decays for the same dye pumped at a variety of wavelength and probed at 520 nm. (Bottom) Transient absorption spectra for the dye when pumped at different wavelengths. The scattered pump light has been subtracted from the spectra.

Knowing this, we may begin calculating injection rates and efficiencies for these dyes. Injection may be calculated in the manner described earlier using the equation:

$$\eta_{ei} = \frac{\frac{1}{\tau_{TiO_2}} - \frac{1}{\tau_{Al2O3}}}{\frac{1}{\tau_{TiO_2}}} \quad (4)$$

Finally, the implied injection lifetime can be calculated

$$\tau_{inj} = \frac{\tau_{TiO2}\tau_{Al2O3}}{\tau_{Al2O3} - \tau_{TiO2}} \quad (5)$$

Table 3-3 shows the results of the injection measurements for the various dyes. The porphyrin dyes all have lower injection efficiencies compared with the squaraine dyes. This makes sense, given the lower reduction potentials of the excited state. As discussed earlier, the E_{S+/E^*} must be significantly above the TiO_2 conduction band edge to drive injection. It would appear that the ~130 mV difference between the Por-Sq dyes and the squaraines is enough to hinder this process. This is seen in the calculated time constants for the injection process. While the value is less than 2 ps for T-CA and DTS-CA, the Por-Sq dyes are all in excess of 5 ps. Since the excited state lifetimes of the dyes on alumina are fairly short, they can compete with slower injection. This helps to account for the poor IPCE of these dyes – they absorb photons very well but they lose about 15% of absorbed photons to radiative relaxation before injection.

Table 3-3. Injection kinetics for the dyes. The kinetics on TiO_2 and Al_2O_3 are measured. The injection efficiency and injection time constant are calculated from these.

Dye	τ_{obs} TiO_2 (ps)	τ_{obs} Al_2O_3 (ps)	η (%)	τ_{inj} (ps)
T-CA	1.8	123.9	98.5	1.83
PBut-SC2-T	9.0	76.0	84.0	10.2
PBut-SC12-T	4.0	29.0	86.0	4.6
PSil-SC12-T	7.0	70.3	90.0	7.8
DTS-CA	1.2	22.6	94.6	1.27
PSil-SC12-DTS	6.1	32.5	81.3	7.5

3.3 Conclusions

We prepared a series of porphyrin-squaraine (Por-Sq) dyes and their electronic, optical, and excited state properties were measured and compared with those of their parent squaraine. These systems have exceptional absorbances because the two chromophores effectively complement each other – the porphyrin provides spectral density in the blue-green region while the squaraine provides it in the red. As an added benefit, the conjugation of these dyes red-shifts the squaraine absorption band about 100 nm to the red allowing these dyes to harvest energy into the near infrared. As a result the Por-Sq dyes outperformed the squaraine dye T-CA in photocurrent, voltage, and overall efficiency. The photocurrent is due to harvesting photons from a greater piece of the solar spectrum but the voltage change is likely due to some other effect. We suspect that the steric shielding of the porphyrin insulates the surface of the TiO_2 to prevent recombination of injected electrons with the electrolyte – although more study is needed to prove this. Curiously none of the Por-Sq dyes outperformed the optimized squaraine dye DTS-CA. Injection efficiency measurements showed that this is because while the squaraine dyes inject with >95% efficiency, the Por-Sq dyes are closer to 85%. We demonstrate that there is no difficulty in moving energy from the porphyrin localized excited states to the squaraine end of the dye – rather the problem is likely that the energy of the lowest lying excited state is too close to the TiO_2 conduction band edge. The energy of this orbital is about 150 mV lower than the lowest excited state on the squaraine dyes. From these results we propose that Por-Sq sensitizers may perform quite well but that the energy of the lower orbital must be raised to improve injection efficiency.

3.4 Experimental

This project was part of a collaboration between numerous scientists. I will address, in detail, the work that I performed. For a detailed procedure for synthetic, optical, and electrochemical measurements please turn to the thesis work of Dr. Fadi Jradi of The Georgia Institute of Technology or the papers published containing these results.

3.4.1 Device Assembly

FTO slides were cleaned by sonication in a series of solutions for 15 minutes each. The solutions were Alconox, ethanol, and water. Finally, the slides were heated to 500 °C for 2 hours to remove all organics.

Platinized cathodes were prepared by drop coating a clean FTO slide with 3 drops of 0.1 M chloroplatinic acid in ethanol. After tilting the slide to evenly disperse the solution, the slide was heated to 400 °C for 20 minutes to leave a thin film of platinum metal.

The electrolyte consisted of consisted of 0.6 M 1,3-dimethylimidazolium iodide, 0.03 M iodine, 0.05 M LiI, 0.05 M guanidinium thiocyanate, and 0.5 M 4-tert-butylpyridine in 15/85 (v/v) mixture of valeronitrile and acetonitrile.

Dye solutions were prepared by dissolving the pure, solid dye in a viable anhydrous solvent (typically ethanol, tetrahydrofuran, or chloroform) to the desired concentration (0.01, 0.05, or 0.1 M). Chenodeoxycholic acid (CDCA) was added to a concentration of 0.1 M to reduce aggregation.

TiO_2 anodes were purchased from Solaronix item 74101. These consisted of a glass slide coated with FTO and a 10 μm thick layer of 20 nm TiO_2 nanospheres with a 4 μm thick layer of 200 nm TiO_2 nanospheres. This first layer is for dye adsorption while the second is to increase light scattering to increase the effective path length of incident photons on the cell. The area of the cell coated with TiO_2 was 0.36 cm^2. These anodes were placed in a 0.2 M

solution of $TiCl_4$ in water and heated to 70 °C for 30 minutes to lay down a thin blocking layer of dense TiO_2. Skipping this step results in poor contact between the TiO_2 nanoparticles and electrolyte contact with the FTO – scavenging increases resultantly. The anodes were removed from the solution and gently rinsed with water before being heated to 450 °C for 2 hours (heating/cooling rate = 2 °C/min).

After cooling to 80 °C, the anodes were immersed in the dye solution for 12 hours. Allowing the anodes to cool to room temperature before immersion decreases efficiency because water is allowed to bind to the TiO_2 which increases dye desorption. The anodes were removed and gently rinsed with acetonitrile and dried by a stream of nitrogen. The cells were immediately assembled by sandwiching a 60 μm Surlin spacer between the anode and cathode. The spacer had a hole large enough to accommodate the TiO_2 active area. To binder clips held the assembly together. Electrolyte was added by placing a drop near the active area, removing one binder clip, and gently separating the cathode and anode by a few millimeters. Capillary action drew the electrolyte into the cell and the clip was replaced giving a temporary seal.

3.4.2 PCE and IPCE Measurements

The air mass (AM) 1.5-irradiance of 100 mW / cm^2 was provided by a solar simulator, which consisted of a 300 W xenon light source (Oriel, U.S.A.) and an optical shutter connected to Keithley meter which was automated with an I-V station from Newport. The light intensity was calibrated with a silicon diode reference cell 91150V (Oriel, U.S.A.). The mismatch between the simulated and the true solar spectra was corrected with the light filter 81094 (Oriel, U.S.A.). The current-voltage performance of the cell under these conditions were tested with four-wire connection mode by sourcing external potential bias to the cell and measuring the generated photocurrent with a Keithley 2400 digital source meter. The test results were acquired with Oriel IV test station software. The incident photon-to-electron conversion

efficiency (IPCE) was characterized by using Oriel Quantum Efficiency Measurement Kit, consisted of a 300W xenon lamp, Merlin lock-in amplifier, Cornerstone 260 monochromator and a silicon detector. The measuring process was automated with TracQ software from Newport.

3.4.3 Transient Absorption Spectroscopy

Sub picosecond pump and probe laser pulses were generated with a Coherent Libra-HE regenerative-amplified Ti:sapphire laser system. The basic pulse compression unit generates 4 mJ, sub-50 ps pulses of 808 nm-centered light at 1 kHz. Approximately 60% of this beam was directed into a Coherent OPerA Solo Ultrafast optical parametric amplifier. This computer controlled OPA was tuned to produce visible light pump pulses at a specific wavelength between 400 and 760 nm. Every other pump pulse was blocked by an optical chopper. For use as a probe, 5% of the original 800 nm beam was directed through a delay stage and then through a sapphire crystal producing a super continuum spectrum ranging from 450 to 820 nm. The two beams were focused and overlapped on the assembled full cells. The $1/e^2$ radii of the pump and probe beams were 900 ± 50 nm and 300 ± 25 nm, respectively. The transmitted portion of the probe beam was collected by a fiber optic cable and Si array detector. ΔA was calculated as a function of delay time by comparing the transmitted probe beam when the pump beam was and was not blocked by the chopper.

For transient absorption measurements, sample preparation was varied from the standard device assembly. Since charge collection was unnecessary, no FTO coated glass was used. TiO_2 films were prepared by doctor blading a layer of TiO_2 nanoparticles (Solaronix 20 nm TiO_2) onto a clean glass microscope slide. The doctor blading guide was simply a piece of Scotch tape with a ¼ inch hole punched out with a hole punch. The film was annealed at

500 °C for 1 hour. Unplatinized glass was used for the "cathode" side and the normal electrolyte was employed.

Alumina films were prepared similarly from an aluminum oxide/hydroxide paste. The paste was prepared by dissolving 100 mg of aluminum isopropoxide in 10 mL of 0.07 M HCl. The solution was slowly evaporated until the alumina began to gel into a thick transparent paste.

3.5 References

1. Nazeeruddin, M. K.; Péchy, P.; Renouard, T.; Zakeeruddin, S. M.; Humphry-Baker, R.; Comte, P.; Liska, P.; Cevey, L.; Costa, E.; Shklover, V., Engineering of efficient panchromatic sensitizers for nanocrystalline TiO2-based solar cells. *Journal of the American Chemical Society* **2001,** *123* (8), 1613-1624.

2. Velusamy, M.; Justin Thomas, K.; Lin, J. T.; Hsu, Y.-C.; Ho, K.-C., Organic dyes incorporating low-band-gap chromophores for dye-sensitized solar cells. *Organic Letters* **2005,** *7* (10), 1899-1902.

3. Mathew, S.; Yella, A.; Gao, P.; Humphry-Baker, R.; Curchod, B. F.; Ashari-Astani, N.; Tavernelli, I.; Rothlisberger, U.; Nazeeruddin, M. K.; Grätzel, M., Dye-sensitized solar cells with 13% efficiency achieved through the molecular engineering of porphyrin sensitizers. *Nature chemistry* **2014,** *6* (3), 242-247.

4. Yum, J.-H.; Jang, S.-R.; Walter, P.; Geiger, T.; Nüesch, F.; Kim, S.; Ko, J.; Grätzel, M.; Nazeeruddin, M. K., Efficient co-sensitization of nanocrystalline TiO 2 films by organic sensitizers. *Chemical communications* **2007,** (44), 4680-4682.

5. Kakiage, K.; Aoyama, Y.; Yano, T.; Oya, K.; Fujisawa, J.-i.; Hanaya, M., Highly-efficient dye-sensitized solar cells with collaborative sensitization by silyl-anchor and carboxy-anchor dyes. *Chemical communications* **2015,** *51* (88), 15894-15897.

6. Karthikeyan, C. S.; Wietasch, H.; Thelakkat, M., Highly Efficient Solid-State Dye-Sensitized TiO2 Solar Cells Using Donor-Antenna Dyes Capable of Multistep Charge-Transfer Cascades. *Advanced Materials* **2007,** *19* (8), 1091-1095.

7. Xie, Y.; Tang, Y.; Wu, W.; Wang, Y.; Liu, J.; Li, X.; Tian, H.; Zhu, W.-H., Porphyrin cosensitization for a photovoltaic efficiency of 11.5%: a record for non-ruthenium solar cells based on iodine electrolyte. *Journal of the American Chemical Society* **2015,** *137* (44), 14055-14058.

8. Kakiage, K.; Aoyama, Y.; Yano, T.; Oya, K.; Kyomen, T.; Hanaya, M., Fabrication of a high-performance dye-sensitized solar cell with 12.8% conversion efficiency using organic silyl-anchor dyes. *Chemical Communications* **2015,** *51* (29), 6315-6317.

9. Warnan, J.; Gardner, J.; Le Pleux, L.; Petersson, J.; Pellegrin, Y.; Blart, E.; Hammarström, L.; Odobel, F., Multichromophoric Sensitizers Based on Squaraine for NiO Based Dye-Sensitized Solar Cells. *The Journal of Physical Chemistry C* **2013,** *118* (1), 103-113.

10. Gouterman, M., Spectra of porphyrins. *Journal of Molecular Spectroscopy* **1961,** *6*, 138-163.

11. Ahrens, M. J.; Sinks, L. E.; Rybtchinski, B.; Liu, W.; Jones, B. A.; Giaimo, J. M.; Gusev, A. V.; Goshe, A. J.; Tiede, D. M.; Wasielewski, M. R., Self-assembly of supramolecular light-harvesting arrays from covalent multi-chromophore perylene-3, 4: 9, 10-bis (dicarboximide) building blocks. *Journal of the American Chemical Society* **2004,** *126* (26), 8284-8294.

12. Wang, Y.; He, G. S.; Prasad, P. N.; Goodson, T., Ultrafast dynamics in multibranched structures with enhanced two-photon absorption. *Journal of the American Chemical Society* **2005,** *127* (29), 10128-10129.

13. Lyon, L. A.; Hupp, J. T., Energetics of the nanocrystalline titanium dioxide/aqueous solution interface: approximate conduction band edge variations between H0=− 10 and H-=+ 26. *The Journal of Physical Chemistry B* **1999,** *103* (22), 4623-4628.

14. Kopidakis, N.; Neale, N. R.; Frank, A. J., Effect of an adsorbent on recombination and band-edge movement in dye-sensitized TiO2 solar cells: evidence for surface passivation. *The Journal of Physical Chemistry B* **2006,** *110* (25), 12485-12489.

15. Bai, Y.; Zhang, J.; Wang, Y.; Zhang, M.; Wang, P., Lithium-modulated conduction band edge shifts and charge-transfer dynamics in dye-sensitized solar cells based on a dicyanamide ionic liquid. *Langmuir* **2011,** *27* (8), 4749-4755.

16. Gai, Y.; Li, J.; Li, S.-S.; Xia, J.-B.; Wei, S.-H., Design of narrow-gap TiO 2: a passivated codoping approach for enhanced photoelectrochemical activity. *Physical review letters* **2009,** *102* (3), 036402.

17. Malinsky, M. D.; Kelly, K. L.; Schatz, G. C.; Van Duyne, R. P., Nanosphere Lithography: Effect of Substrate on the Localized Surface Plasmon Resonance Spectrum of Silver Nanoparticles. *J. Phys. Chem. B* **2001,** *105* (12), 2343-2350.

18. Lenzmann, F.; Krueger, J.; Burnside, S.; Brooks, K.; Grätzel, M.; Gal, D.; Rühle, S.; Cahen, D., Surface photovoltage spectroscopy of dye-sensitized solar cells with TiO2, Nb2O5, and SrTiO3 nanocrystalline photoanodes: Indication for electron injection from higher excited dye states. *The Journal of Physical Chemistry B* **2001,** *105* (27), 6347-6352.

19. Jain, P. K.; Lee, K. S.; El-Sayed, I. H.; El-Sayed, M. A., Calculated Absorption and Scattering Properties of Gold Nanoparticles of Different Size, Shape, and Composition: Applications in Biological Imaging and Biomedicine. *J. Phys. Chem. B* **2006,** *110* (14), 7238-7248.

20. Huang, W. Y.; Qian, W.; El-Sayed, M. A.; Ding, Y.; Wang, Z. L., Effect of the lattice crystallinity on the electron-phonon relaxation rates in gold nanoparticles. *J. Phys. Chem. C* **2007,** *111* (29), 10751-10757.

21. Hu, M.; Novo, C.; Funston, A.; Wang, H. N.; Staleva, H.; Zou, S. L.; Mulvaney, P.; Xia, Y. N.; Hartland, G. V., Dark-field microscopy studies of single metal nanoparticles: understanding the factors that influence the linewidth of the localized surface plasmon resonance. *J. Mater. Chem.* **2008,** *18* (17), 1949-1960.

22. Perner, M.; Gresillon, S.; März, J.; von Plessen, G.; Feldmann, J.; Porstendorfer, J.; Berg, K. J.; Berg, G., Observation of Hot-Electron Pressure in the Vibration Dynamics of Metal Nanoparticles. *Physical Review Letters* **2000,** *85* (4), 792-795.

23. Mohamed, M. B.; Ahmadi, T. S.; Link, S.; Braun, M.; El-Sayed, M. A., Hot electron and phonon dynamics of gold nanoparticles embedded in a gel matrix. *Chem. Phys. Lett.* **2001,** *343* (1-2), 55-63.

CHAPTER 4 – VIBRATIONAL DYNAMICS OF GOLD AND SILVER NANORODS

4.1 Overview

Nanorods and other anisotropic nanoparticles have very different mechanical properties than the more usual nanospheres. We studied the coherent lattice oscillations (phonons) of gold and silver nanorods (AuNRs and AgNRs) by following the modulations of the plasmonic band position with ultrafast laser spectroscopy. Although gold and silver nanopheres of similar radius have similar phonon frequencies, AgNRs vibrate faster than AuNRs. We probed this dissimilarity by using finite element modeling. We were able to find better agreement between experimental and computational results by adopting a pentagonal rather than cylindrical shape for the nanorods. Furthermore we accounted for the fact that the electron-phonon relaxation causes a decrease in the Young's modulus and softens the rods. The calculations showed that shorter rods have an anomalously low frequency. This can be rationalized because their tips constitute a larger portion of their length and the thin tips are softer.

4.2 Introduction

When light of a resonant frequency illuminates metal, the loosely bound conduction band electrons may oscillate coherently.[1, 4] These plasmons rarely last more than a few femtoseconds. The energy can either be reradiated as scattered light, transferred to an adjacent system, or lost as heat as the process of absorption is completed.[6] If neither scattering nor

energy transfer occurs, the oscillating electrons will begin to dephase due to electron-surface scattering, electron-hole pair generation, and electron-crystal boundary scattering (especially prominent in polycrystalline nanoparticles).[8-9] Electron-hole pairs can be generated when the incident photon has sufficient energy to promote an electron within the conduction band (intra-band excitation) or between the d and conduction bands (inter-band).[12,13,] Although the plasmon has decayed, the electrons still have a tremendous amount of energy – depending on the illumination intensity, their temperature can be in excess of 1000 K – and that energy is in a non-equilibrium distribution. They begin to thermalize by electron-electron and electron-phonon collisions, each with a characteristic lifetime. Electron-electron scattering occurs in a few hundred femtoseconds and allows the electrons to thermalize among themselves. Transfer of energy to nuclear motion, that is to say phonons, occurs within 1-5 ps.[10-11] The electron-phonon coupling has been shown to vary with the matrix around the nanoparticle in $MgSO_4$[13], polymer, and glass[16]. This process appears to be size and shape independent.[17] Finally, these phonons couple to the surrounding medium and lose their energy as environmental heat over 10-100 ps. Femtosecond laser spectroscopy has revealed these various processes and their timescales.

The phononic modes of nanoparticles depend on a variety of factors including, shape, material, temperature, and crystallinity. Measuring the frequency begins by perturbing the particle with a femtosecond laser pulse. If absorption occurs, as described above, the energy will soon transfer to lattice vibrations. As the vibrations cause a periodic shift in the size, shape, and density of the nanoparticles, it will also cause the plasmonic resonance to shift.[20-21] As a practical matter, the frequency shift is typically measured as a change in intensity at a single frequency as the centerpoint of the resonance moves about a central value.

This technique has been used to study the lattice frequencies of isotropic shapes like gold and silver nanospheres[22] and nanoprisms[15]. For spheres, the fundamental vibrational mode is primarily dependent on the Young's modulus and so gold and silver nanospheres have similar frequencies for a given size. This does not hold true for other shapes whose frequencies have a stronger dependence on density. Additionally polycrystallinity can have an impact.[23-24]

This chapter contains our study of the optomechanical properties of anisotropic nanoparticle shapes experimentally, using ultrafast time-resolved pump-probe spectroscopy, and computationally, by finite element modeling. We compare our results for silver nanorods with the results of Hu *et al.* for similarly sized gold nanorods. The rods are compared to nanospheres. We also speculate on the effect of changing temperatures.

4.3 Experimental

Collaboration Note: Dr. Mahmoud Mahmoud of the El-Sayed group at Georgia Tech synthesized the gold and silver nanorods. I was responsible for collecting and analyzing the ultrafast dynamics data. I performed all finite element modeling.

All reagents were purchased from Sigma-Aldrich and used as received. Care was taken to store the silver nitrate in the dark and the sodium borohydride in a desiccator.

4.3.1 Silver Nanorods

We prepared silver nanorods with a fixed diameter but different lengths by the reduction of silver nitrate with ethylene glycol as reported previously.[25] 70 mL of ethylene glycol was heated to 140 ^{o}C for 1 hr with stirring. The temperature was then increased to 175 ^{o}C and 0.5 g of polyvinylpyrrolidone was added with stirring at 1600 rpm. A solution of silver nitrate (0.15 g in 15 mL ethylene glycol) was injected and stirring continued for a variable amount of time. After about five minutes the solution turned pink. As time progressed the

solution proceeded through red, green, olive, and yellow indicated increased length. Aliquots were withdrawn and quenched in ice as the reaction proceeded to obtain the different sizes. The resulting particles were purified by repeated centrifugation at 12000 rpm for 20 minutes and dispersion in DI water. Figure 4-1 shows a high-resolution TEM of a silver nanorod.

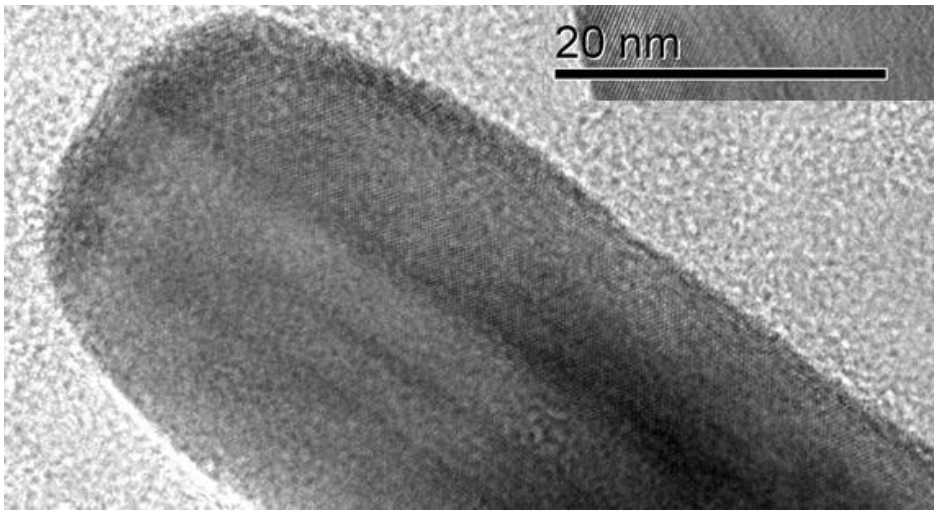

Figure 4-1. High-resolution TEM of a single silver nanorod. The rod has pentatwinned structure with a truncated tip

4.3.2 Gold Nanorods

Gold nanorods (AuNRs) were prepared with two different lengths following a known procedure.[11] Initially a seed solution was produced. To 5 mL of 200 mM cetrymonium bromide (CTAB), 5 mL of 0.5 mM $HAuCl_4$ was added. Next 0.6 mL of chilled 0.01 M $NaBH_4$ was added producing a bronze colored solution. Vigorous stirring over 2 minutes completed the reaction.

Growth solutions were prepared by adding CTAB (5 mL, 0.20 M) to between 0.05 and 0.25 mL of 4 mM $AgNO_3$ at 25 °C. 1 mM $HAuCl_4$ was added and after gentle mixing 70 μL of 0.0788 M ascorbic acid was introduced. The ascorbic acid acted as a mild reducing agent

and the yellow solvated gold chloride complex became colorless but did not produce metallic gold nanoparticles. Finally, 12 μL of seed solution was added to the growth solution at room temperature. With slow stirring the color of the solution changed over 20 minutes indicating the growth of nanorods.

4.3.3 Imaging

A Zeiss Ultra 60 was used to image the silver nanorods (Figure 4-2). A JEOL 2000 TEM was used to image the gold nanorods (Figure 4-3). A Tecnai F30 was used for high-resolution transmission electron microscopy (HR-TEM) imaging. The sizes of the nanoparticles were determined in ImageJ, at least 100 nanoparticles of each size were imaged to determine average sizes. These results are summarized in Table 4-1. The uncertainties are the standard deviations of the samples.

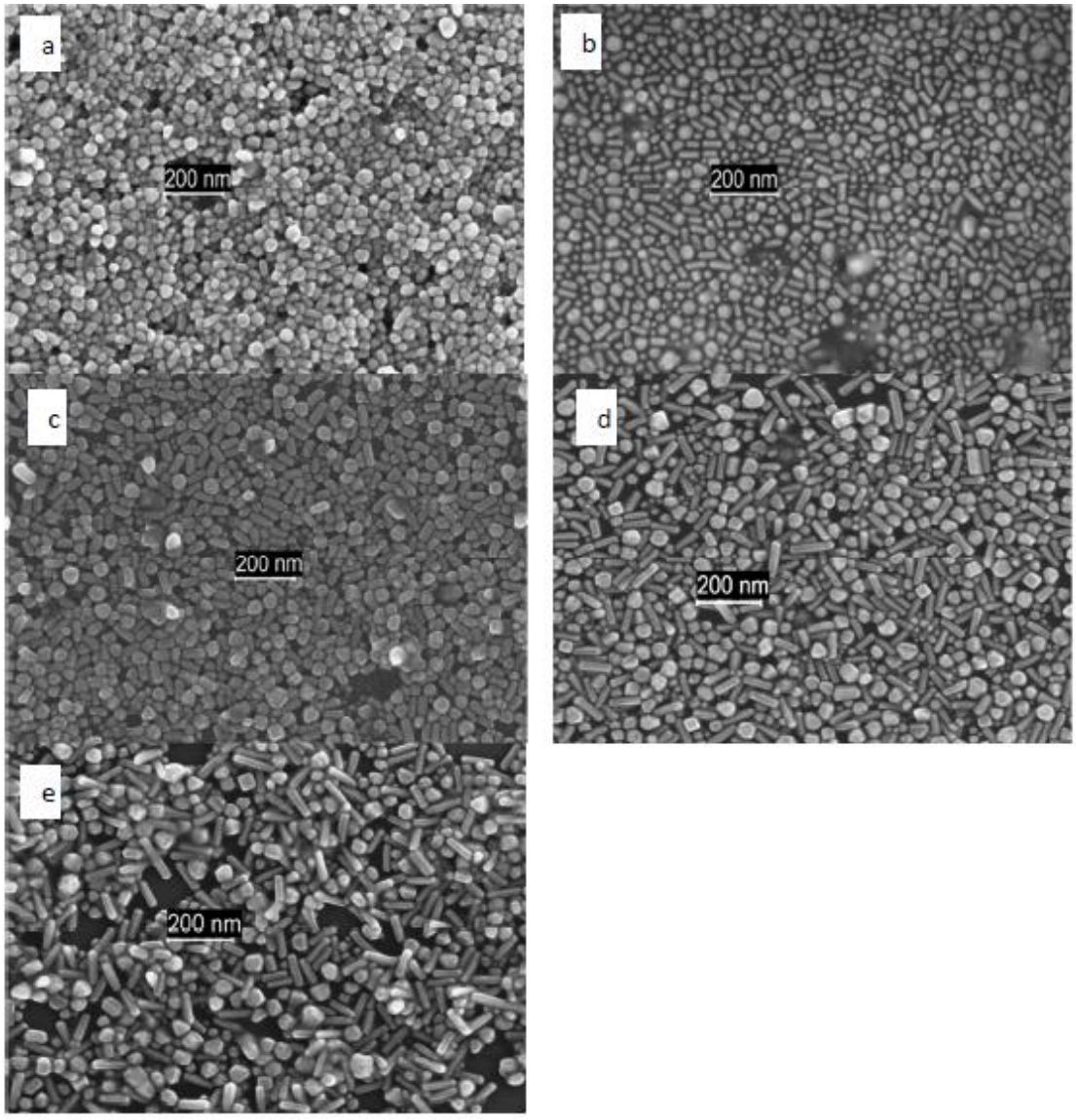

Figure 4-2. TEM images of silver nanorods. See table below for size information.

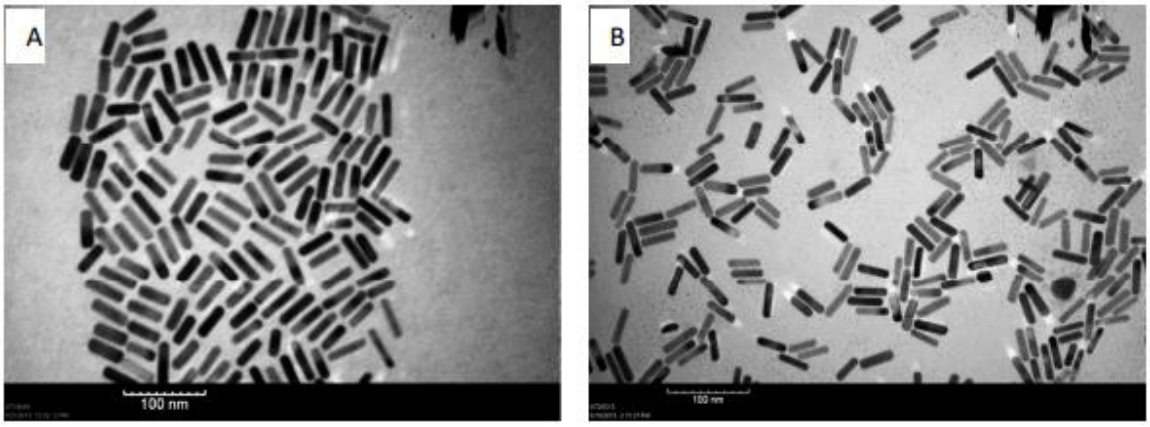

Figure 4-3. TEM images of gold nanorods. See table below for size information.

Table 4-1. Lengths and widths of the gold and silver nanorods.

Sample	Length (nm)	Diameter (nm)
Silver - a	39.6±3.2	20.1±1.7
Silver - b	44.9±4.7	20.3±1.1
Silver - c	55.5±5.5	21.7±1.7
Silver - d	73.5±7.8	21.3±1.7
Silver - e	86.0±9.7	21.1±1.7
Gold – a	67.2±1.2	22.4±0.8
Gold - b	77.3±2.2	21.1±0.9

4.3.4 Dynamics

The vibrational dynamics were determined for the nanorods by transient absorption. The system used consisted of a Coherent Libra HE regenerative-amplified Ti:sapphire laser system which yielded 4 mJ, sub-50 ps pulses of 810 nm-centered light with a repetition rate of 1 kHz. Approximately one quarter of this beam was frequency doubled by a barium borate crystal to give a 405 nm pump beam. The intensity of this beam was controlled by a neutral density filter. Every other pump beam pulse was blocked by an optical chopper. The remainder of the 800 nm beam passed through a delay stage and then a sapphire crystal producing a

supercontinuum from about 450 nm to 820 nm. This probe beam was band-pass filtered to remove excess 800 nm light.

The two beams were focused and overlapped on the sample. The $1/e^2$ radii of the pump and probe beams were 850 ± 50 μm and 275 ± 25 μm, respectively. The transmitted probe beam was focused into a fiber optic cable and measured by a Si array detector. ΔA was calculated as a function of delay time by comparing the transmitted probe beam when the pump beam was and was not blocked by the chopper.

Solution measurements were performed in 2 mm optical crown glass cuvettes. Solutions were diluted to peak optical densities of < 1 AU. Pump beam fluences were kept below 20 $\mu J/cm^2$ to minimize sample damage.

Sample dynamics were studied for a single wavelength between 15 and 40 nm below the sample's extinction maximum. The ΔA data was empirically modeled as two exponential decays and an exponentially decaying sinusoid:[15]

$$\Delta A(t) = B_1 \cos(2\pi f + \phi)\, e^{-t/\tau_1} + B_2 e^{-t/\tau_2} + B_3 e^{-t/\tau_3} + c \qquad (1)$$

B_n, τ_n, f, ϕ, and c are the pre-exponential constants, time constants, frequency, phase, and offset, respectively. Fits were performed using custom Python code utilizing the Scipy and Numpy libraries.[27] By probing all samples on the same side of their extinction maxima, we minimized phase and frequency differences.[28]

4.3.5 Finite Element Modeling

Finite element modeling (FEM) allows one to calculate the vibrational modes (eigenfrequencies) for arbitrarily shaped nanoparticles. We utilized the COMSOL 3.3 software package for our calculations. Nanoparticle shapes were constructed in AutoCAD.

4.4 Results and Discussion

4.4.1 Experimental Results

Gaining an understanding of the mechanical properties of nanostructures is essential before they can be fully utilized in applications. Bulk gold and silver are well understood but it is still debated how they change at the nanoscale. Additionally, nanoparticles can experience rapid thermal changes which may impact their properties.

We focused on studying isotropically shapped gold and silver nanorods. In order to make accurate comparisons we used rods of similar diameter but with varying lengths. A time-resolved femtosecond pump-probe technique was used to measure the optomechanical properties of AgNRs and AuNRs. Coherent lattice vibrations were first induced with a 405 nm femtosecond laser pulse and their frequencies were probed by a second pulse, with a wavelength in resonance with the LSPR of the nanoparticles, at variable time delay. The LSPR peak position changes with the structural changes caused by the phonons. Thus measuring the LSPR shift frequency is akin to measuring the phonon frequency.

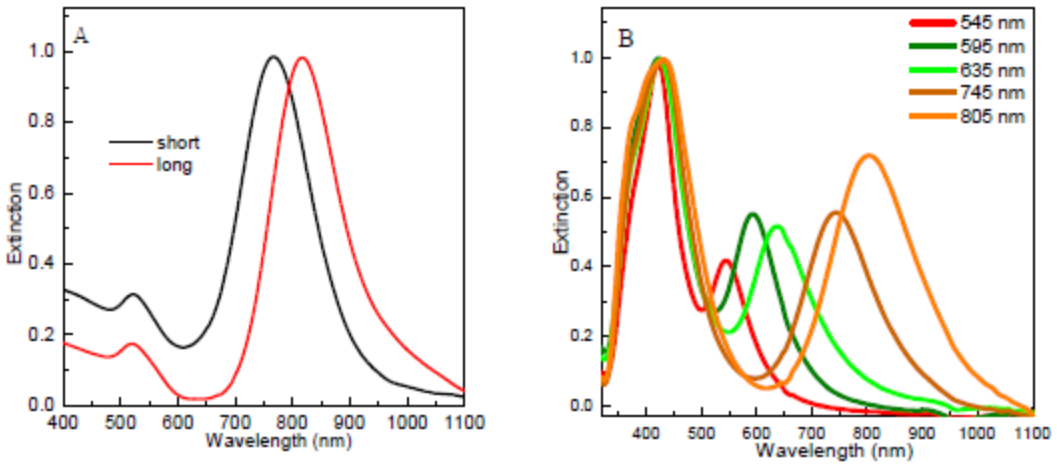

Figure 4-4. Extinction spectra of A) gold and B) silver nanorods. The peak labeled short corresponds to gold-a. The peak labeled long corresponds to gold-b. The LSPR peak positions are listed for the silver nanorods. They correspond to samples silver-a, silver-b, silver-c, silver-d, and silver-e respectively.

Figure 4-4 shows the extinction spectra of the AgNRs and AuNRs. As the length of the rods is increased, the position of the LSPR band red-shifts. Or rather, it should be said that as the aspect ratio (diameter divided by length) of the rods increases, their LSPR bands red-shift. However, because widths are quite similar, length is proportional to aspect ratio.

Figure 4-5 shows an example of a transient absorption spectra for the silver nanorods a few hundred picoseconds after excitation. 405 nm light was used pump the particles. This light has sufficient energy to produce electronic transitions within gold and silver in addition to plasmonic excitations. However, similar transient spectra are observed if using light that only has enough energy to produce plasmonic excitations. What occurs is that as energy is added to the conduction band electrons, the polarizability of the nanoparticles changes. This leads to a shift in the LSPR band of the nanoparticles. This registers as a large negative peak next to a large positive peak in the transient spectrum. Because the LSPR band also changes shape during this process, the transient peaks are not necessarily symmetric.

Figure 4-6A shows the transient absorption signal for the silver nanorods with lengths 39.6 and 86.0 nm. These were pumped at 405 nm and probed at 529 and 787 nm, respectively. Although the response of the samples over a wide range of probe wavelengths was measured, only a single wavelength was selected for analysis. In all cases we used a wavelength on the higher energy side of the LSPR band. The data was fit to Eq. 1. The cosine term provides the phonon frequency. The exponential in the first term relates to the decay of the phonon as well as dephasing due to some variability in the nanoparticle size. The other two exponential terms are primarily present to provide a good fit of the first few picosecond of data. They relate to the decay of the thermalization of the hot electrons.

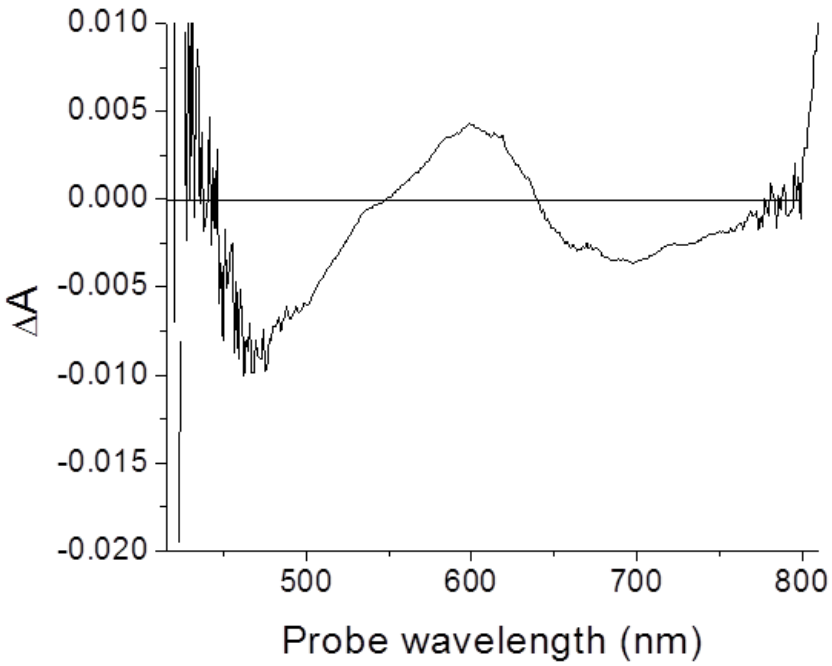

Figure 4-5. Example of a transient spectrum from a silver nanorod.

Previous studies have shown that the main observed frequency for nanorods is the longitudinal mode of vibration.[29] This mode is a simple stretch along the long axis of the nanoparticle. It is expected to vary with the length and be insensitive to the diameter. However, since all rods had similar diameters this could not be investigated.

A similar procedure was used to measure gold nanorods with two different lengths. In order to make a full comparison between gold and silver we show the data obtained for AuNRs by Hartland's group.[27] Figure 4-6B shows a full comparison of the frequencies of gold and silver nanorods. The data from Hu *et al.* is shown in red and is similar to the data that we obtained for gold nanorods (shown in blue).

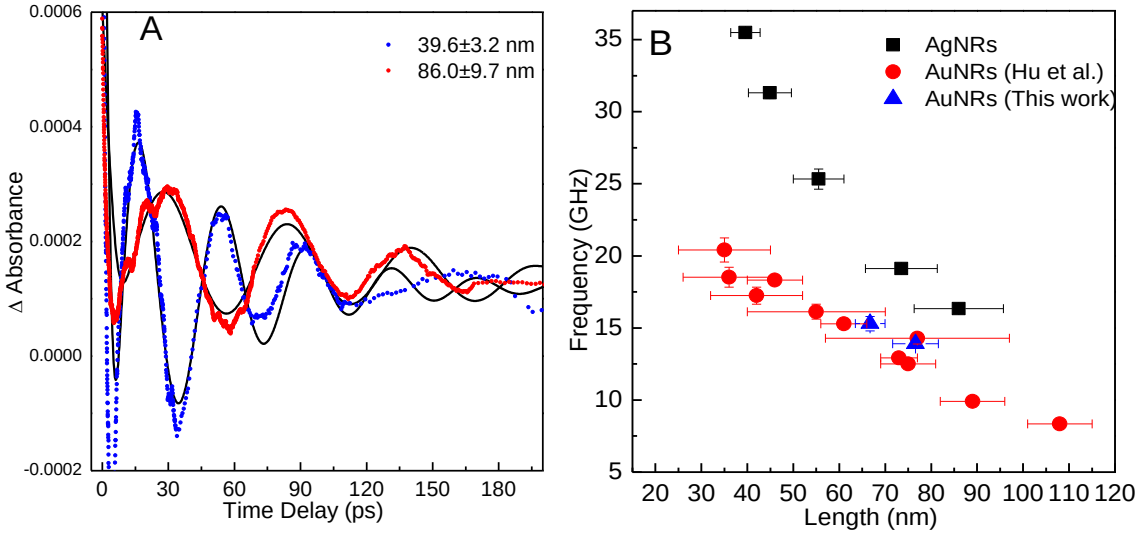

Figure 4-6. A) Example vibrational data from silver nanorods with lengths 39.8 and 86 nm. B) Measured vibrational frequencies as a function of length for the various silver and gold nanorods discussed in this work. This is the frequency of the extensional mode.

Overall, we see that the vibrational frequency decreases with increasing length and that silver has a higher vibrational frequency than similarly sized gold nanorods. Additionally, it appears that silver nanorods are more sensitive to length changes than gold nanorods. Curiously, this behavior differs from the much better studied nanospheres. Others have shown that silver and gold nanospheres have about the same frequency for a given size.[21, 22] In order to understand these difference it is necessary to turn to some theoretical and computational results. The following section provides an examination of these differences.

4.4.2 Theoretical Results

This section draws heavily upon ideas not typically covered in chemistry. For a deeper explanation of terms and concepts please see Appendix A. The natural frequencies of cylinders have been exactly calculated. For the purposes of this work, we are only interested in the first longitudinal (extensional) mode. Which relates frequency (*f*), to length (L), Young's modulus

(E) and density (ρ). This equation has been used to model gold nanorods by assuming that the nanorods are cylindrical.[30]

$$f = \frac{1}{2L} \times \sqrt{\frac{E}{\rho}} \tag{2}$$

Similarly, an equation has been found for the breathing mode of spheres. This mode exhibits a radially symmetric expansion.

$$f = \frac{\chi c_l}{2\pi R} \tag{3}$$

$$\chi \cot(\chi) = 1 - \frac{\chi^2 c_l^2}{4 c_t^2} \tag{4}$$

Where *f* is the frequency of the breathing modes, *R* is the radius, c_l is the longitudinal speed of sound, c_t is the transverse speed of sound, and χ are the eigenvalues which correspond to each mode. These are found by numerically solving Equation 4. Since low energy phonons are typically produced in these experiments, we need only consider the lowest eigenvalue.

In a typical calculation, the bulk values for the metals are used. The densities are 19.3 and 10.5 g/cm^3 for gold and silver, respectively. The Young's moduli for these metals are 79 and 83 GPa respectively. These values were determined for isotropic polycrystalline samples. When these values are applied to spheres the results are quite good. Figure 4-7 shows experimental data for gold and silver nanospheres found in papers by Del Fatti *et al.*[21] and Hodak *et al.*[22] Over a wide range of sizes, Eq. 3 provides an excellent fit of the results and shows a clear inverse relationship between size and frequency.

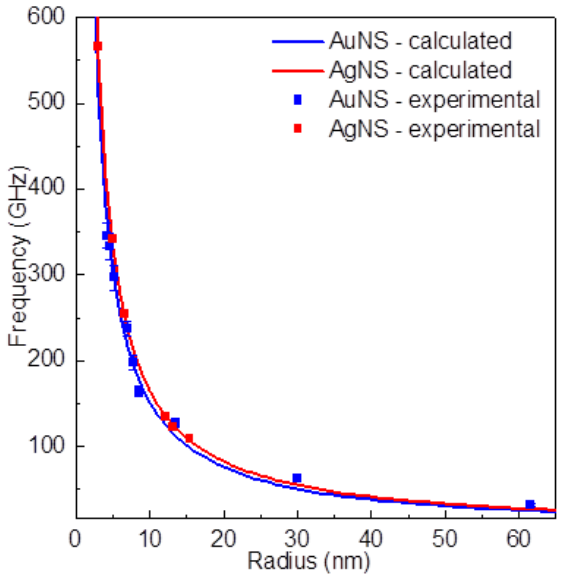

Figure 4-7. Comparison of experimental and calculated results for gold and silver nanospheres. The experimental data was taken from two other publications.[21, 22]

When the same is attempted for the nanorods the results are less promising. Figure 4-8 shows a comparison of measured and calculated vibrational frequencies for gold and silver nanorods. It is apparent that although the fit is closer for the longer lengths, the short rods show a significant deviation. In particular, we see that the short rods are calculated to be much stiffer than measured. An obvious reason for this is that we are modeling the rods as exact cylinders. We know from the high resolution TEM (Figure 4-1) that the rods are more accurately described as flat sided rods with reasonably sharp tips. Additionally, the model assumes that the nanoparticles are isotropic (same properties in all directions) and polycrystalline. We know that both gold and silver nanorods are multitwinned (typically constructed from 5 different crystal grains). Thus, it would be more accurate to treat these nanoparticles anisotropically.

Others have sought to overcome these problems for some nanoparticle shapes. Petrova *et al.* have found that the data for gold rods is fit better if you assume that the gold is

anisotropic.[31] Crut *et al.* have looked into using finite-element modeling to study the vibrational modes of both nanospheres and nanorods. They found that it was necessary to introduce higher order vibrations, so-called quadrupolar modes, in order to explain their experimental results.[27]

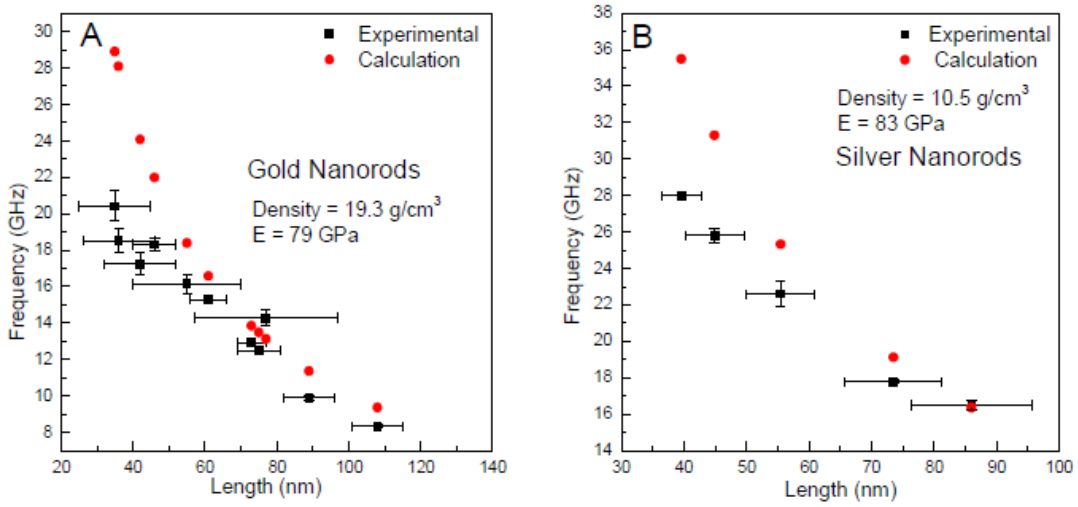

Figure 4-8. Comparison of experimental and calculated frequencies for A) gold and B) silver nanorods

In moving away from an idealized cylinder, we had no hope of finding and exact expression for the natural phononic modes for our nanorods. To deal with this constraint, we turned to a standard tool of engineering analysis: finite element modeling (FEM). Appendix A contains a more detailed discussion of how FEM works as well as its strengths and limitations compared to other approaches. We utilized the FEM package COMSOL to calculate the eigenfrequencies of AuNRs and AgNRs. These were modeled as pentagonal prisms with pentagonal tips of varying sharpnesses. Instead of the mechanical properties of bulk gold/silver listed above, we treated the metals as cubically anisotropic. This requires three distinct constants of elasticity rather than the two of an isotropic material (c11, c12, c44). For

gold c11 = 193 GPa, c12 = 164 GPa, c44 = 42 GPa. For silver c11 = 124 GPa, c12 = 93 GPa, c44 = 46 GPa.

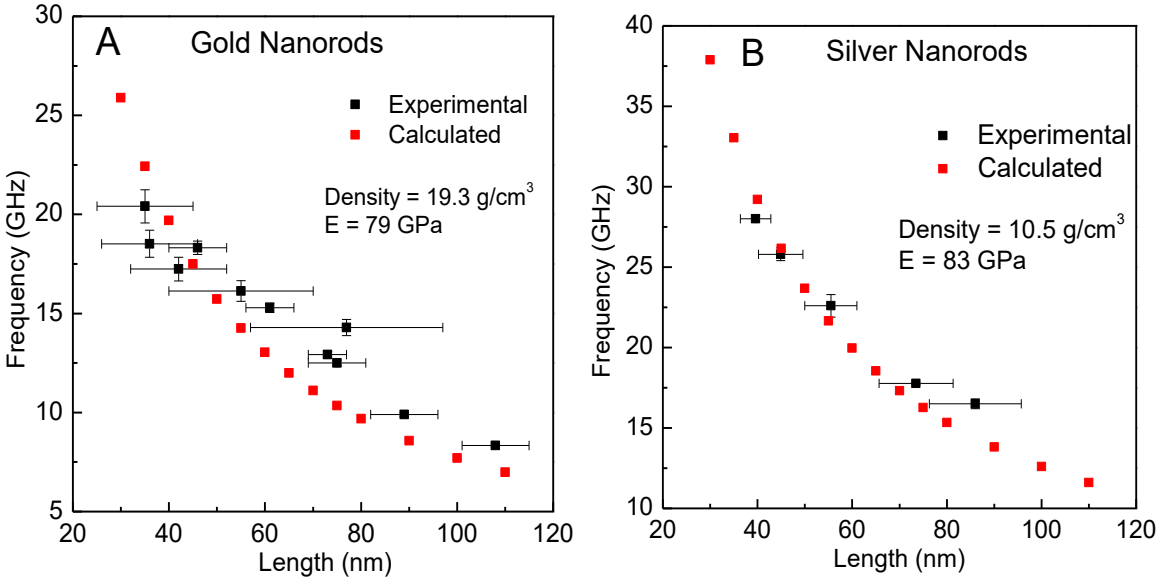

Figure 4-9. Experimental and computational values for the extensional frequencies of A) gold and B) silver nanorods

Figure 4-1 shows a high resolution image of a silver nanorod in which the tapered tip is clearly visible. Others have observed a similar phenomenon for AuNRs.[32] We explored a variety of different tip shapes including points which fully tapered and ones in which the tip was truncated with a flat plane. To avoid overfitting our data we limited the number of options considered to a few different archetypes. The best fit was given by a truncated model. Figure 4-9 shows a comparison of the data to the experimental fits obtained by finite element modeling. Clearly, this has improved the fit of the model although there is still some discrepancy. Possible reasons for this deviations include: 1) All of the models (both FEM and analytical equations) have used room temperature values for the elastic constants. However, the measurement technique is invasive – energy is added to the system which eventually heats

the lattice. Since elastic constants are temperature dependent this could lead to some disagreement. 2) However, the calculations involving gold and silver nanoparticles agreed very well with the experimental results. If temperature were the problem, it should affect spheres as well as rods. Perhaps, the anisotropy of the nanorods introduces another factor which must be accounted for.

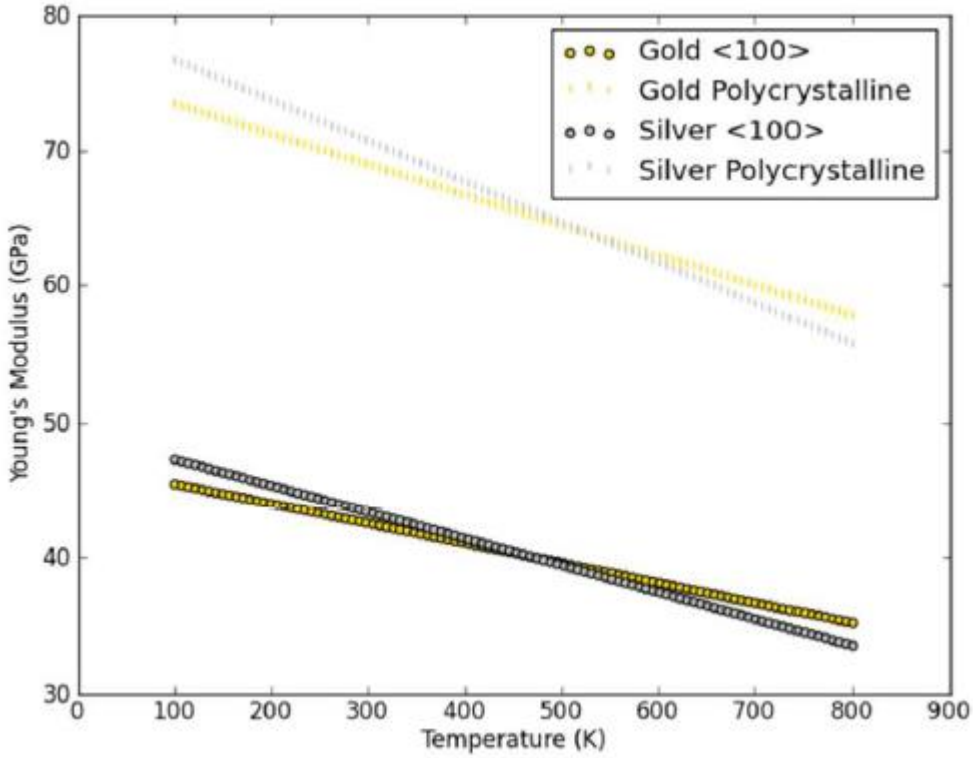

Figure 4-10. Young's modulus for gold and silver as a function of temperature. The values for both polycrystalline metal and single crystalline along the <100> direction are shown.

4.4.3 Temperature Effects

The values of the Young's modulus and the generalized elastic constants depend heavily upon the temperature of the materials (Figure 4-10).[33] The figure shows that there is, roughly, a decreasing linear relationship between temperature and Young's modulus. Although

not shown, the individual elastic constants (c11, c12, and c44) have a similar dependency. Interestingly, silver varies more with silver than gold does.

We repeated out calculations at a variety of temperatures to see how this would affect the results. Figure 4-11 shows the shift in the extensional frequency of silver nanorods relative to the frequency at 300 K. In all cases, the frequency decreases as temperature increases in accordance with a general "softening" at higher temperatures. Interestingly, the small nanorods are more effected than the large ones. This is mainly due to the fact that small nanorods have a larger frequency to begin with.

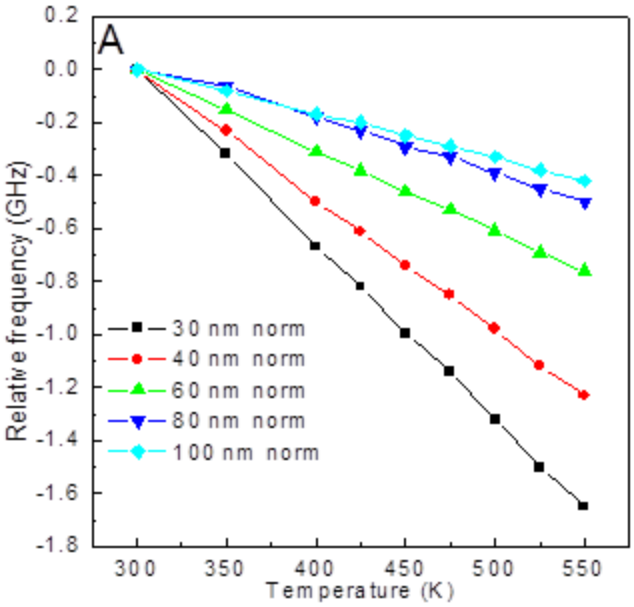

Figure 4-11. Shift in calculated extensional frequency relative to the value at 300 K for silver nanorods at different temperatures.

The temperature of the nanorods depends upon a number of factors including size, pump intensity, absorption coefficient, and cooling rate. It is estimated that the temperature of nanoparticles may briefly reach a few hundred ^{o}C.[1-4] In our experiment, the pump intensity was kept constant in the different experiments. Thus, the temperature change should depend

upon the number of absorbed photons which depends on the absorption cross-sections of the nanorods. Since the gold and silver nanorods were pumped by different transistions, the length dependences of their absorption cross sections were different. The AuNRs were pumped by exciting their interband transition while transverse plasmon modes of the AgNRs were excited. The absorbance of this latter transition has little dependence upon the length of the nanoparticle. Thus it is expected that the different sizes of silver nanorods would absorb equal numbers of photons. Since the large rods have a greater volume, they should experience a smaller temperature rise. This will decrease the frequency difference between short and long rods – a trend which is observed.

For gold the story is simpler. The interband transition for gold vary proportionally with volume. Therefore, for a fixed pump power, the lattice temperatures of gold nanorods with different lengths will be similar.

4.5 Conclusions

The lattice vibration frequencies of silver and gold nanospheres of similar sizes are very similar. The analytical solution for a vibrating sphere predicts the experimental results very accurately. Nanorods, however, cannot be accurately modeled by the analytical solution for a vibrating cylinder. Additionally, a large difference between gold and silver nanorods of similar sizes is observed. A large reason for this discrepancy is that nanorods are not cylinders. In order to correct for this, finite element model simulations were carried out to calculate the extensional frequency of gold and silver nanorods. The modeling results of the frequency agree well with the experiment, but not completely. This mismatch results from the fact that the Young's modulus is temperature dependent, while previous models assume room temperature values for elastic constants. For this reason we have carried out the calculations at different

temperatures. The values of the frequency of the lattice vibration of silver and gold nanorods decrease as the length of the rod increases.

4.6 Future Work

Further work is needed to examine the effect of temperature upon the mechanical properties of gold and silver nanorods. On an experimental front, we can vary the pump intensity to see if the vibrational frequency changes. Based on our current findings we would expect that as the pump intensity increased, the extensional frequency should decline. Ideally this would involve some way to measure the temperature of nanoparticles. However, it should be possible to accomplish something similar by varying the ambient temperature during the measurement. Consider measuring the frequency of the nanoparticles at ambient temperatures of 30, 80, 130, and 180 °C, with the pump providing the same increase in temperature for each sample. By observing the frequency change between the samples, we could estimate the change induced by pump heating.

Another avenue of investigation is to fully harness the power of finite element modeling. These models are able to incorporate light absorption and heat propagation calculations. It is possible to construct a model of a nanoparticle, illuminate it with light, and see how its mechanical properties change with time as it heats and cools.

4.7 References

1. Link, S.; Hathcock, D. J.; Nikoobakht, B.; El-Sayed, M. A., Medium effect on the electron cooling dynamics in gold nanorods and truncated tetrahedra. *Advanced Materials* **2003,** *15* (5), 393.

2. El-Sayed, M. A., Small is different: Shape-, size-, and composition-dependent properties of some colloidal semiconductor nanocrystals. *Acc. Chem. Res.* **2004,** *37* (5), 326-333.

3. Link, S.; Furube, A.; Mohamed, M. B.; Asahi, T.; Masuhara, H.; El-Sayed, M. A., Hot electron relaxation dynamics of gold nanoparticles embedded in MgSO4 powder compared to solution: The effect of the surrounding medium. *J. Phys. Chem. B* **2002,** *106* (5), 945-955.

4. Mohamed, M. B.; Ahmadi, T. S.; Link, S.; Braun, M.; El-Sayed, M. A., Hot electron and phonon dynamics of gold nanoparticles embedded in a gel matrix. *Chem. Phys. Lett.* **2001,** *343* (1-2), 55-63.

5. Halte, V.; Bigot, J. Y.; Palpant, B.; Broyer, M.; Prevel, B.; Perez, A., Size dependence of the energy relaxation in silver nanoparticles embedded in dielectric matrices. *Appl. Phys. Lett.* **1999,** *75* (24), 3799-3801.

6. Link, S.; Burda, C.; Mohamed, M. B.; Nikoobakht, B.; El-Sayed, M. A., Femtosecond transient-absorption dynamics of colloidal gold nanorods: Shape independence of the electron-phonon relaxation time. *Physical Review B* **2000,** *61* (9), 6086-6090.

7. Hodak, J. H.; Martini, I.; Hartland, G. V., Spectroscopy and Dynamics of Nanometer-Sized Noble Metal Particles. *The Journal of Physical Chemistry B* **1998,** *102* (36), 6958-6967.

8. Ahmadi, T. S.; Logunov, S. L.; El-Sayed, M. A., Picosecond Dynamics of Colloidal Gold Nanoparticles. *The Journal of Physical Chemistry* **1996,** *100* (20), 8053-8056.

9. Heilweil, E. J.; Hochstrasser, R. M., Nonlinear spectroscopy and picosecond transient grating study of colloidal gold. *The Journal of Chemical Physics* **1985,** *82* (11), 4762-4770.

10. Zhang, J. Z., Ultrafast Studies of Electron Dynamics in Semiconductor and Metal Colloidal Nanoparticles: Effects of Size and Surface. *Acc. Chem. Res.* **1997,** *30* (10), 423-429.

11. Hartland, G. V., Optical Studies of Dynamics in Noble Metal Nanostructures. *Chemical Reviews* **2011,** *111* (6), 3858-3887.

12. Del Fatti, N.; Voisin, C.; Chevy, F.; Vallee, F.; Flytzanis, C., Coherent acoustic mode oscillation and damping in silver nanoparticles. *Journal of Chemical Physics* **1999,** *110* (23), 11484-11487.

13. Hodak, J. H.; Henglein, A.; Hartland, G. V., Size dependent properties of Au particles: Coherent excitation and dephasing of acoustic vibrational modes. *Journal of Chemical Physics* **1999,** *111* (18), 8613-8621.

14. Huang, W. Y.; Qian, W.; El-Sayed, M. A., The optically detected coherent lattice oscillations in silver and gold monolayer periodic nanoprism arrays: The effect of interparticle coupling. *J. Phys. Chem. B* **2005,** *109* (40), 18881-18888.

15. Petrova, H.; Perez-Juste, J.; Zhang, Z. Y.; Zhang, J.; Kosel, T.; Hartland, G. V., Crystal structure dependence of the elastic constants of gold nanorods. *Journal of Materials Chemistry* **2006,** *16* (40), 3957-3963.

16. Hu, M.; Wang, X.; Hartland, G. V.; Mulvaney, P.; Juste, J. P.; Sader, J. E., Vibrational Response of Nanorods to Ultrafast Laser Induced Heating: Theoretical and Experimental Analysis. *Journal of the American Chemical Society* **2003,** *125* (48), 14925-14933.

17. Mahmoud, M. A.; El-Sayed, M. A., Different Plasmon Sensing Behavior of Silver and Gold Nanorods. *The Journal of Physical Chemistry Letters* **2013**.

18. Jana, N. R.; Gearheart, L.; Murphy, C. J., Wet chemical synthesis of high aspect ratio cylindrical gold nanorods. *J. Phys. Chem. B* **2001,** *105* (19), 4065-4067.

19. Nikoobakht, B.; El-Sayed, M. A., Preparation and growth mechanism of gold nanorods (NRs) using seed-mediated growth method. *Chemistry of Materials* **2003,** *15* (10), 1957-1962.

20. Hartland, G. V.; Hu, M.; Wilson, O.; Mulvaney, P.; Sader, J. E., Coherent excitation of vibrational modes in gold nanorods. *J. Phys. Chem. B* **2002,** *106* (4), 743-747.

21. Oliphant, T. E., Python for scientific computing. *Computing in Science & Engineering* **2007,** *9* (3), 10-20.

22. Hu, M.; Wang, X.; Hartland, G. V.; Mulvaney, P.; Juste, J. P.; Sader, J. E., Vibrational response of nanorods to ultrafast laser induced heating: Theoretical and experimental analysis. *Journal of the American Chemical Society* **2003,** *125* (48), 14925-14933.

23. Crut, A.; Maioli, P.; Fatti, N. D.; Vallee, F., Anisotropy effects on the time-resolved spectroscopy of the acoustic vibrations of nanoobjects. *Physical Chemistry Chemical Physics* **2009,** *11* (28), 5882-5888.

24. Enrique Carbo-Argibay, B. R.-G., Sergio Gomez-Grana, Andres Guerrero-; Martinez, I. P.-S., Jorge Perez-Juste, and Luis M. Liz-Marzan, The Crystalline Structure of Gold Nanorods Revisited: Evidence for Higher-Index Lateral Facets. *Angewandte Chemie* **2010,** *122*, 9587-9590.

25. Neighbours, J.; Alers, G., Elastic constants of silver and gold. *Physical Review* **1958,** *111* (3), 707.

26. Mahmoud, M. A.; El-Sayed, M. A.; Gao, J.; Landman, U., High-frequency mechanical stirring initiates anisotropic growth of seeds requisite for synthesis of asymmetric metallic nanoparticles like silver nanorods. *Nano Lett.* **2013,** *13* (10), 4739-4745.

27. Mie, G., Beiträge zur Optik trüber Medien, speziell kolloidaler Metallösungen. *Annalen der physik* **1908,** *330* (3), 377-445.

28. Mulvaney, P., Surface plasmon spectroscopy of nanosized metal particles. *Langmuir* **1996,** *12* (3), 788-800.

29. Papavassiliou, G. C., Optical properties of small inorganic and organic metal particles. *Prog. Solid State Chem.* **1979,** *12* (3–4), 185-271.

30. El-Sayed, M. A., Some Interesting Properties of Metals Confined in Time and Nanometer Space of Different Shapes. *Acc. Chem. Res.* **2001,** *34* (4), 257-264.

31. Jiang; Bosnick, K.; Maillard, M.; Brus, L., Single Molecule Raman Spectroscopy at the Junctions of Large Ag Nanocrystals. *J. Phys. Chem. B* **2003,** *107* (37), 9964-9972.

32. Maier, S. A.; Atwater, H. A., Plasmonics: Localization and guiding of electromagnetic energy in metal/dielectric structures. *J. Appl. Phys.* **2005,** *98* (1), -.

33. Jain, P. K.; Huang, W.; El-Sayed, M. A., On the Universal Scaling Behavior of the Distance Decay of Plasmon Coupling in Metal Nanoparticle Pairs: A Plasmon Ruler Equation. *Nano Lett.* **2007,** *7* (7), 2080-2088.

CHAPTER 5 – PLASMONIC COUPLING OF GOLD/SILVER HETERODIMERS

5.1 Summary

Gold and silver nanocubes are known to have incredible electric fields induced by plasmonic resonances. These types of particles are used in sensing and imaging applications because the coupling between the particles results in hot spots which can enhance processes like absorption, Raman scattering, and fluorescence. In these situations it is aggregates of nanoparticles rather than individual particles which dominate the enhancement effect. To understand aggregates we began with the first step, dimerization. This chapter describes the use of the discrete dipole approximation (DDA) to calculate how the interaction of nanocubes changes as the distance between them is reduced. In particular we examine the change in the absorption and scattering components of the localized surface plasmon resonance (LSPR) spectra of homo and heterodimers of Ag and Au nanocubes. We also examined the changes in the nanocube surface plasmonic field distributions as the dimer separation was varied.

The results from the homodimers were as expected: as the cubes were brought together, there was a red-shift in the primary plasmon band in accordance with the universal scaling law. Additionally, as the particles moved together, scattering contributed more to the overall extinction. By examining the E-field distributions, we found that the hot spot geometry changes abruptly at small separations. At distances below 2 nm, the hot spot was located between the two adjacent faces and moved away from the corners. Further away, the hot spots moved to the corners. We observed apparently anomalous behavior for the heterodimer. First, the E-field resulting from excitation of the Ag dominated plasmon resonance was significantly

weaker than expected. Second, the red-shift of the gold dominated plasmon resonance did not follow the universal scaling law. The most likely explanation for these observations is that the silver plasmon mixes strongly with the energetically resonant, but nonplasmonic, gold interband transition to form a hybrid resonance that produces weaker overall field intensity on the two nanocubes at short separation. We propose an ultrafast pump-probe experiment to measure the transfer of energy within the heterodimer and relate this to the features observed in the spectra.

5.2 Introduction

The field of plasmonic metal nanoparticles has been the subject of intense research recently for their interesting optical and photothermal properties arising from their localized surface plasmon resonance (LSPR). A plasmon is the collective oscillatory motion of electrons resulting from the coherent excitation of the "free" electrons in the conduction band. This leads to an in-phase strong electromagnetic oscillation. This LSPR is tunable and strongly dependent on the shape, size, composition, and relative dielectric function of the nanostructure.[8] The oscillation of the electrons results in a strong enhancement in the optical absorption, scattering and near-field intensities of noble metal nanoparticles allowing for their use in numerous applications such as biological imaging, selective photothermal therapy, surface enhanced Raman scattering (SERS), optical wave guiding, and biochemical sensing.[11-12] The effect of coupling between the surface plasmons of adjacent particles, such as in nanoparticle aggregates, is very important and has received a great deal of attention in recent years. Coupling typically results in a shift in the LSPR wavelength and a great enhancement of the plasmonic E-field. This is important in optical technologies in chemical and biological imaging, sensing,[16-19] and therapeutics. This interparticle plasmon coupling forms the basis

of the intense enhancement of spectroscopic signals (e.g., SERS) from molecules adsorbed at nanoparticle junctions, providing the capability for single-molecule sensing and detection. The overall strength of coupling depends on the polarization direction of the exciting field and the distance between nanoparticles. It has been observed that the LSPR shift due to coupling decreases exponentially with increasing interparticle distance. When normalized to particle size, the relationship holds for many nanoparticles with different sizes, shapes, metals, and media; this has been termed the universal scaling law.[24-26]

Silver and gold nanocubes with sharp corners are known to have very strong plasmonic fields concentrated at their corners. The study of the coupling between a pair of silver nanocubes and the effect of rounding the cube corners on their coupling strength has recently been carried out. In the present paper, we used the discrete dipole approximation (DDA) method to study the distance dependence of the plasmonic field coupling between homodimers (Ag-Ag or Au-Au) and heterodimers (Ag-Au) of nanocubes with sharp corners. We examined the dependence of the interaction with light on interparticle separation. We looked at the effect on the LSPR extinction wavelength and the relative importance of the contribution of the absorption and scattering to the total extinction peak intensity. Next, we studied the field intensity distribution and the hot spot formation between adjacent nanoparticles at small interparticle separations. Finally, we propose how this system could be used to investigate the formation of a Fano resonance between gold and silver nanocubes.

5.2.1 Discrete Dipole Approximation

There are several methods to simulate the optical properties of metallic nanoparticles. DDA is one of the most powerful theoretical method for simulating extinction, absorption, and scattering spectra of plasmonic nanoparticles as well as plasmonic field distributions.[14, 27-31] The advantage of this method is that it includes multipolar and finite size effects which are

quite important for particles with sizes close to the wavelength of light. Details of this method have been described before but an explanation of the technique is in order.

When light interacts with a particle it begins by exerting a force on the electrons within the particle via its electric field. In response, these electrons move according to their polarizability. The redistribution of each electron changes the overall electric field which creates new forces on all the electrons. This causes them to move which in turn changes the electric field and so on and so on. The discrete dipole approximation provides a simplification of the system to make the computational problem tractable. The first step is to split the object into a cubic lattice of evenly spaced dipoles. The properties of these dipoles can be exactly related to the experimentally determinable optical properties of the bulk material by the Clausius-Mossotti relationship. This was originally demonstrated for individual atoms or molecules by Hendrick Lorentz. Specifically, it relates the relative permittivity of the material (ε) to the polarizability of the dipoles (α). The number density of the dipoles (N) given in number per volume and the permittivity of free space (ε_0) are also needed.

$$\alpha = \frac{3\varepsilon_0}{N}\frac{\varepsilon-1}{\varepsilon+2} \quad (1)$$

Although this relation was originally applied to individual atoms or molecules on a lattice, there is no reason that it cannot be applied to larger "clumps" of matter on a lattice – which is indeed standard practice for DDA calculations.

Once the polarizability of the dipoles has been determined, their interaction with incident light – and each other – may be exactly calculated using Maxwell's equations. This exact computation holds true for both a finite number of dipoles and an infinite – but periodic – structure. Thus, accuracy is limited only by how accurately the shape of the dipole lattice reflects the true shape of the nanoparticle being studied. The way to improve this is to increase

the density of dipoles at the cost of computational speed. Highly curved structures need a greater density of dipoles while cubic ones need fewer.

Originally, this technique was developed to calculate scattering by interstellar particles. Extending the technique to account for absorption merely requires using the complex permittivity. Most DDA software allow for immersion of the particles in a medium. Commonly air is used although water, oil, and silica are sometimes considered. Typically, software forces the user to choose a single polarization of light for their calculations. Unpolarized light may be simulated by averaging over a range of polarizations of light. Since the polarizability of the dipoles is a function of wavelength, repeating the calculation for different wavelengths will produce an extinction spectrum.

The electric field around the nanoparticle is solved for as a side effect of calculating the extinction spectra. This allows one to see how the E-field around the nanoparticle is enhanced by the plasmonic modes. For these calculations a wavelength must be specified. Usually, a wavelength near the peak of interest is selected. Although the electric field is a vector field, For sensing purposes, the direction of the field is always essential. In these cases the square of the electric field magnitude, E^2, is reported.

5.2.2 Fano Resonance

A Fano resonance is a characterisitc assymetric lineshape that occurs when a sharp resonant feature couples with a broad continuum feature.[18, 32] A typical Fano resonance is shown in Figure 5-1 exhibiting the usual dip next to the resonant peak. In the case of plasmonic nanoparticles, it is expected that silver and gold nanoparticles couple in this fashion. In this case, the gold nanoparticle's interband transition provides the broad continuum process and the silver's LSPR provides the shape resonant process. There should be a dip in the extinction next to the silver's peak if coupling occurs. This may, of course, be buried

underneather other spectral features. This dip is due to destructive interference between the two processes.

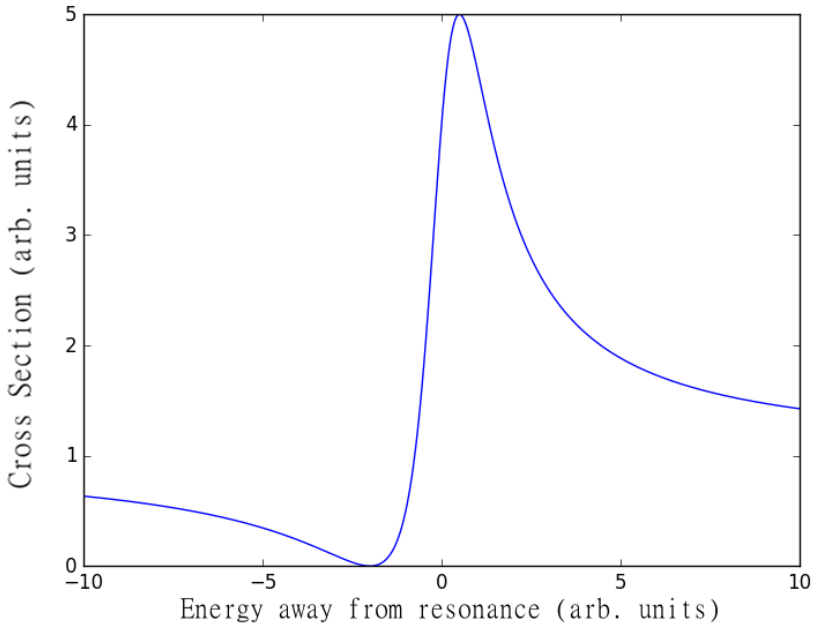

Figure 5-1. A typical Fano resonance. A dip is present next to the resonant peak.

5.3 Results and Discussion

Collaboration Note: Dr. Nasrin Hooshmand of the El-Sayed group at Georgia Tech performed most of the DDA calculations. I set up the initial calculations and performed analysis of the results.

Previous experimental studies have examined the effect of changing the interparticle distance and the incident polarization on the spectra of the dimers of gold and silver nanospheres. In the present work we compare the theoretical results of the plasmonic coupling between homo- and heterodimers of silver and gold nanocubes with sharp corners on their extinction, absorption and scattering and plasmonic field intensity.

5.3.1 Two Gold Cubes

As two plasmonic nanoparticles are brought close together, hybridization occurs between the plasmon modes of the particles.[36] These hybrid modes tend to be red-shifted but depending on the polarization of light, may be blue-shifted. Figure 5-2 shows the calculated extinction, absorption and scattering spectra for a pair of Au nanocubes with 42 nm edges in water as a function of the interparticle separation. It shows that as the cubes are moved together, the extinction peak red shifts. It is clear from Figure 5-2b that these cubes follow the typical scaling law seen for other particles. The total extinction increases from 5 a.u. for a single particle (or a large separation) to 18 a.u. for 2 nm of separation. The percentage of scattering increases from less than 1% for a single nanocube to 5% for 2 nm separation. Upon decreasing the separation, the extinction band maximum red-shifts from 585 nm to 641 nm. These results are expected. Larger particles tend to have a larger scattering-to-absorption ratio and a redder extinction peak than small particles. As the interparticle separation of the dimer is decreased, it behaves more like a single large particle than two small particles.

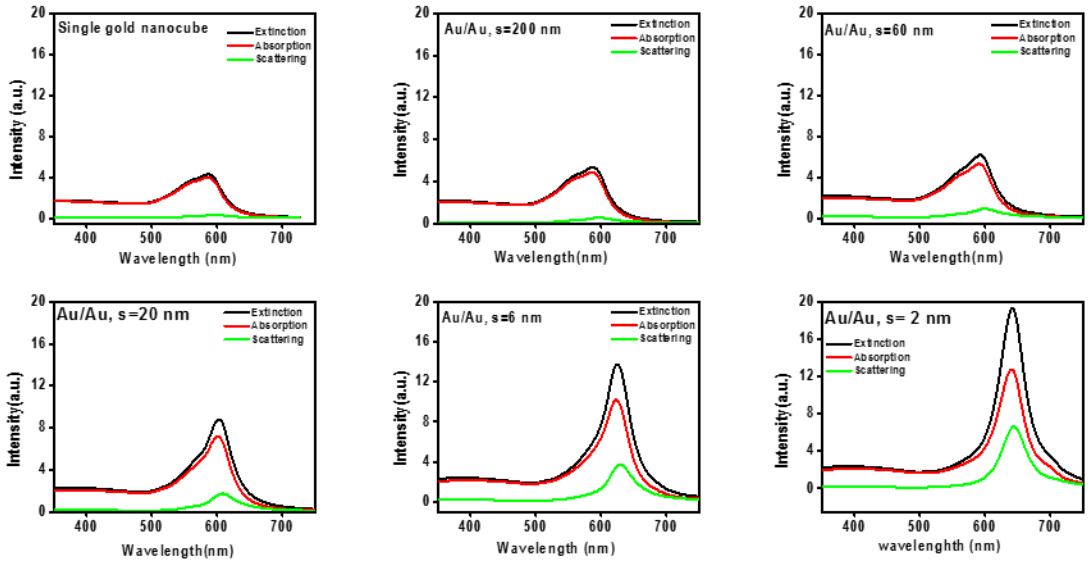

Figure 5-2. Calculated extinction, absorption, and scattering spectra for two gold cubes at separations of 2, 6, 20, 60, and 200 nm. The spectra for a single gold cube are included for comparison.

Nanosphere dimers are known to obey the "plasmon ruler equation". The rule states that as the separation is decreased, the peak position will red shift following an exponential trend. Spheres of different sizes will indeed follow a similar equation if the distance is normalized to the size of the particle. Figure 5-3b shows this analysis applied to the gold cubes – the calculated fit parameters are included in the figure.

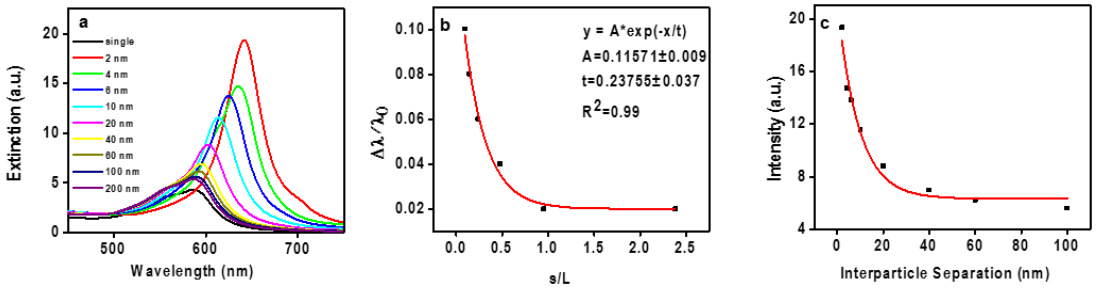

Figure 5-3. Comparison of the extinction spectra of two gold cubes. A) The extinction spectra red shift as the separation is increased. B) The peak position measured relative to the peak position of a single gold cube as a function of separation distance normalized to the edge length of a cube (42 nm). C) The intensity of the peak measured as a function of separation.

To better understand the hybridization process between the two approaching nanocubes, the E-field plasmonic enhancement was calculated for a single gold nanoparticle and dimers with various separations. For these calculations, a single wavelength at the peak of the plasmon band of interest was used to excite the particle or dimer. Figure 5-3 shows the E-field enhancement around a single gold nanocube (excited at 585 nm), a dimer with 2 nm of separation (641 nm excitation), and a dimer with 10 nm separation (613 nm excitation). The field around the single nanocube shows the characteristic pattern of field concentration at the corners. The 10 nm separated dimer shows a similar pattern with a slight strengthening of the

field near the adjacent corners. When the separation is reduced to 2 nm the field strength moves away from the adjacent corners and to in between facing facets of the dimer.

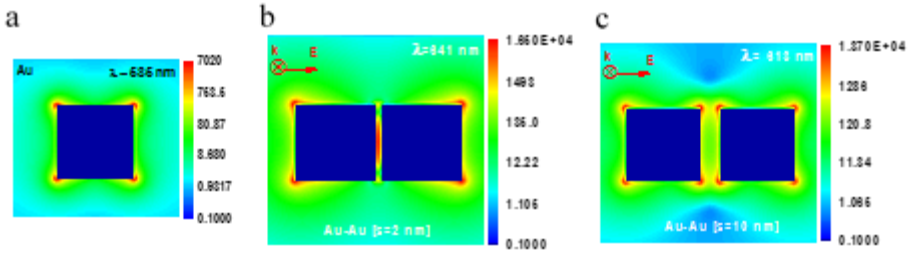

Figure 5-4. Calculated E-field magnitude for A) a single gold cube, B) two gold cubes at a separation of 2 nm, and C) two gold cubes at a separation of 10 nm.

5.3.2 Two Silver Cubes

DDA calculations were repeated for pairs of silver nanocubes. Figure 5-5 shows that the extinction spectrum of a widely separated pair is nearly identical to that of the monomer. They both have four bands: two strong bands at long wavelengths (probably dipolar) and two weak higher order bands at short wavelengths. As the separation decreases, all the bands shift to longer wavelengths, but the shorter wavelength bands seem to shift further than the longer wavelength bands. While a strong doublet is observed for 60 nm of separation, one band of the doublet becomes weaker but broader in the 20 nm separation spectrum. It is possible that the higher order bands become stronger and the higher energy dipolar band is submerged under the strong higher order band. Figure 5-5 shows the results of the decomposition of the extinction band into absorption and scattering. While the absorption is more intense than scattering for the single Ag cube (and for the pair at 200 nm), they become comparable in intensity at 60 nm separation and the scattering becomes stronger at shorter distances.

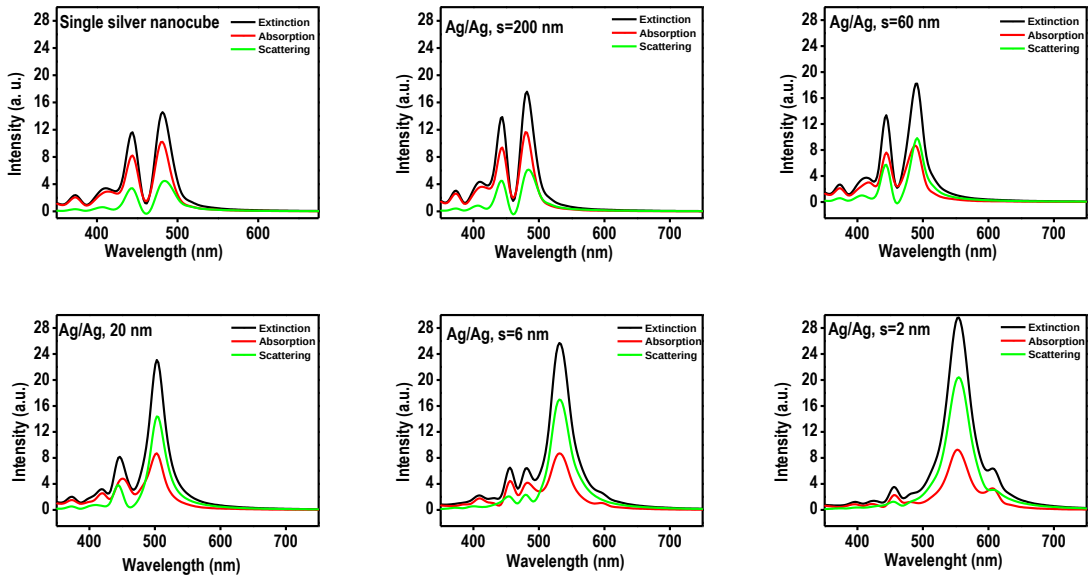

Figure 5-5. Extinction, absorption, and scattering spectra for silver nanocube dimers in water with separations of 2, 6, 20, 60, and 200 nm. The spectra for a single silver nanocube are included for reference.

Figure 5-6 shows a comparison of the extinction spectra of the silver nanocube dimer. As with gold, the position of the main peak red shifts as the separation is decreased. This is not surprise as a closely spaced dimer is quite similar to a larger rectangular nanorod. Rectangular nanorods would have a redder extinction peak. Once again, the shift follows an exponential dependence on the separation. The peak intensity also increases as the separation is decreased.

The E-fields of silver dimers and an isolated silver cube were calculated in a similar manner as was used for the gold particles. Due to the presence of multiple distinguishable plasmonic modes for a single silver particle, only the peak wavelength for the main resonance at 481 nm was excited. As seen in Figure 5-7, this produced an E-field distribution that is similar to the single gold nanocube. The hybridized dimer modes were examined as well yielding similar results as to those for the Au-Au nanocube dimer. At 10 nm of separation, the field strength is strongest at the corners. At 2 nm of separation, the strongest field moves to

the center of the adjacent faces. In all cases, the fields are stronger than for the equivalent gold nanocube systems, as expected.

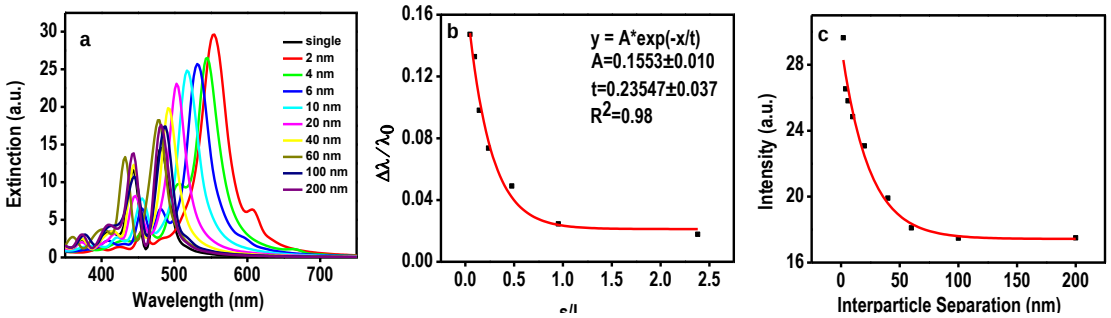

Figure 5-6. A) Extinction spectra of two silver cubes at a variety of separations. As the separations decreases, the absorption peak red shifts. B) The extent of red shifting as a function of separation. The red shift is normalized to the peak position of a single silver cube and the distance is normalized to the size of the cubes (42 nm). The data is fit by an exponential function whose constants are shown in the figure. C) The intensity of the peak increases with decreasing separation with an exponential relationship.

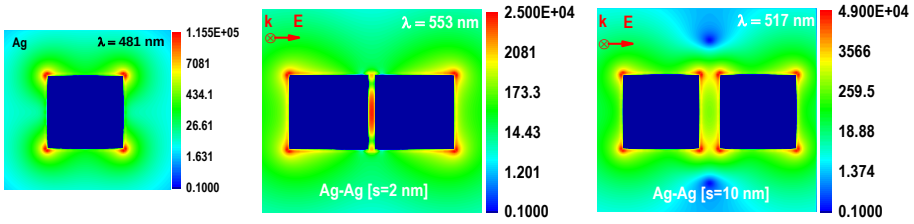

Figure 5-7. E-field intensity plots for silver nanocubes. A) A single silver nanocube exhibits strong fields around its corners. B) Two silver cubes at a separation of 2 nm. The strongest E-field moves to the center between the two faces. C) The E-field around two silver cubes with at a separation of 10 nm. The field is located around the corners.

5.3.3 Heterodimers of Gold and Silver

The results from the heterodimers yield more exciting conclusions. We expect that the plasmonic modes of gold and silver will mix to form hybrid modes. Naively, we might think that the two hybrid modes would be (ΨAu + ΨAg) and (ΨAu – ΨAg), where ΨAu and ΨAg

are the dipolar modes for gold and silver respectively. However, since the energies of the uncoupled modes are so different (gold at 585 nm and silver at 481 nm) the hybrid modes will not have equal contributions from gold and silver. Additionally, as was discussed by Sheikholeslami *et al.* in their work on silver-gold nanosphere heterodimers[37], because the interband transition of gold strongly overlaps energetically with the silver nanocube's natural LSPR resonance, the LSPR resonance of the Ag nanocube may strongly couple to it. As Figure 5-8 shows, at large separations there is no coupling between the silver and gold cubes. The spectrum is nearly identical to the summation of the spectra for a single gold cube and a single silver cube. As the Au cube gets closer to the Ag cube, mixing occurs between the wavefunctions of two particles. The band around 600 nm, which is predominantly gold-like in character (as discussed later), red-shifts with decreasing separation (although it does not follow the universal scaling law like the homodimers). The higher energy bands of silver below 500 nm decrease in intensity as the cubes move closer to one another.

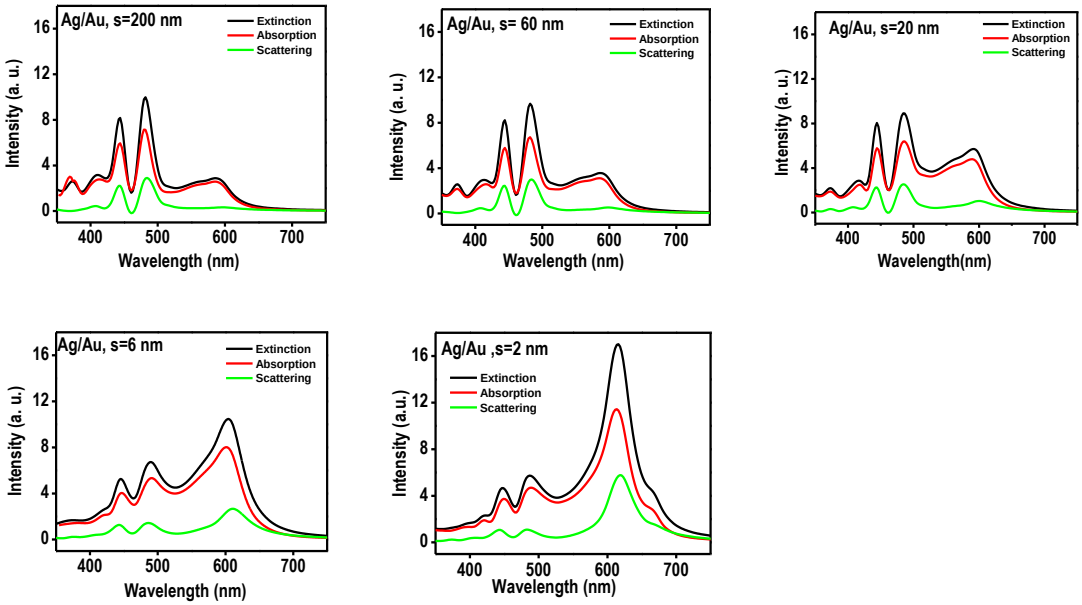

Figure 5-8. Calculated spectra for gold-silver nanocube heterodimers. The separations between the cubes are 2, 6, 20, 60, and 200 nm.

E-fields were calculated at different excitation wavelengths to unravel the interplay between the gold and silver nanocube electronic systems. Although the hybrid bands contain both gold and silver components, most of the bands will be predominantly composed of either gold (at the low energy region in Figure 5-10) or silver (at the high energy region in Figure 5-10). It is expected that the band near 600 nm is mostly gold-like in character because the spectra in Figure 5-8 show it forming from the gold based resonance of the 200 nm separation spectrum. This is borne out in Figure 5-10, which shows the fields resulting from exciting a 2 nm separated dimer with 615 nm light and a 10 nm dimer with 597 nm light. With 10 nm of separation the field is located primarily upon the corners of the gold cube (on the right). At 2 nm of separation, the field strength increases on the silver cube due to increased mixing-in of silver's dipolar wavefunction, however, it is still weaker than the field around the gold cube.

This hybrid mode can be represented as $\Psi = a\Psi_{Au} + b\Psi_{Ag}$ where $a > b$. Just as with the homodimers, the E-field is strongest at the corners and between the adjacent faces.

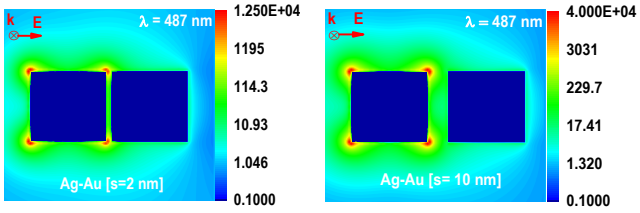

Figure 5-9. Calculated E-field for a gold-silver nanocube dimer at a separation of A) 10 nm and B) 2 nm. In both cases the silver cube is on the left and the gold cube on the right. The exciting wavelength of light was selected to probe the silver-like extinction bands and is given in the top right corner.

Exciting at a shorter wavelength stimulates hybrid modes that have more silver character. Figure 5-9 shows the result of probing 2 nm and 10 nm dimers at 487 nm. In both cases we see essentially no field strength around the gold cubes' corners. This supports the claim that this hybrid mode contains little gold dipole character. Interestingly, as the distance is reduced from 10 nm to 2 nm, the overall field strength is reduced contrary to what was seen with all other dimer pairs and excitation wavelengths. This is because silver's dipole mode

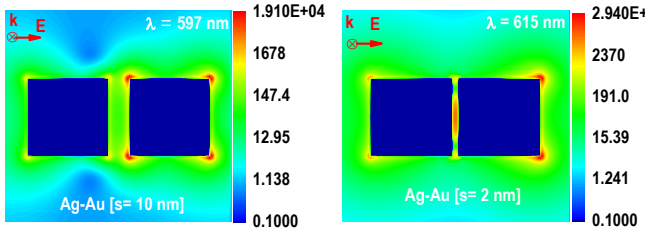

Figure 5-10. Calculated E-field for a gold-silver nanocube dimer at a separation of A) 10 nm and B) 2 nm. In both cases the silver cube is on the left and the gold cube on the right. The exciting wavelength of light was selected to probe the gold-like extinction bands and is given in the top right corner.

hybridizes with the gold interband transition. Exciting the interband transition produces an incoherent excitation and little net E-field and so a hybrid mode containing significant interband transition-character will produce a weaker overall E-field. We would also expect that there would be little to no E-field located on the gold nanocube, which is observed. We surmise that the wavefunction of this mode has the form $\Psi = a\Psi_{Ag} + b\Psi_{Au} + c\Psi_{IB}$, where Ψ_{IB} is the interband excited state wavefunction, with $a > c$ and $b \approx 0$. This wavefunction explains the absence of E-field around the gold nanoparticle.

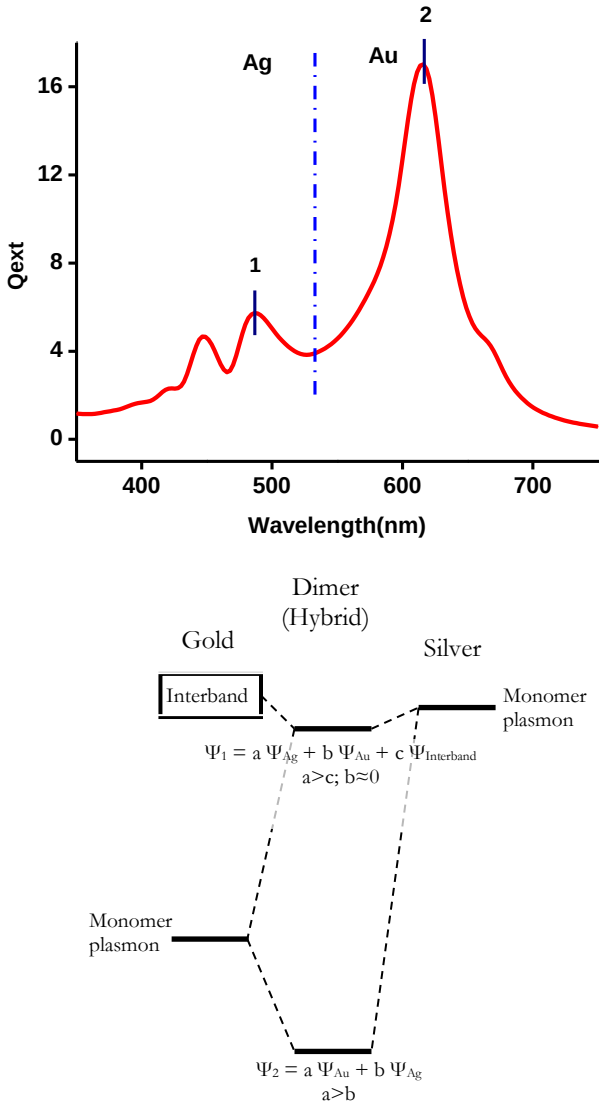

Figure 5-11. The proposed interaction model for a gold cube and silver cube. A) In the extinction spectrum the higher energy region is dominated by a single peak which is silver-like in character. The lower energy peak is gold-like. B) A mode mixing schematic showing how the monomer plasmons combine to form hybrid dimer modes. Gold's interband transition is similar in energy to silver's plasmon and so mixes with it.

Our proposed explanation for this system is shown in Figure 5-11. The extinction spectrum for the heterodimer has two main regions. The high energy region is mainly silver-like in character. The low energy region is dominated by a single peak which is gold-like. This first band is composed of silver's monomer plasmon mixing with the interband transition of gold. The lower energy peak is composed of the gold monomer plasmon with a little silver character mixed in.

Although we observe no clear signature of a Fano resonance in the heterodimer spectrum, it is quite possible that it is simply buried underneath other features. The theoretical calculations of Bachelier *et al.* suggest that although a Fano resonance would be present for heterodimers of spheres, it would not be distinguishable in the spectrum of the total system.[35] Ultrafast pump-probe spectroscopy provides a way around this problem. The system may be pumped with a wavelength that preferentially excites the silver nanoparticle (say 500 nm) and then probed with a wavelength that is preferentially effected by changes to the gold nanoparticle (say 650 nm). The amount of energy the pump pulse adds to the gold nanoparticle as a function of wavelength will be the measure of the absorption spectrum of the gold. The amount of energy added to the gold can be measured by seeing how much the absorption is effected at 650 nm. The more energy that is added, the more the temperature of the gold will increase and there will be a larger change in absorption. Then this change in absorption can be mapped out as a function of pump wavelength. There should be Fano-like dip near the position of the silver's LSPR. A similar experiment was performed by Lombardi *et al* in 2016.[1]

5.4 Conclusions

Exciting homodimers of gold and silver nanocubes parallel to the interparticle axis gave results consistent with expectations. Decreasing the distance between the cubes

strengthened the E-field around the particles and red-shifted the extinction in agreement with the universal scaling law and gave an exponential dependence of the dimer extinction intensity on their separation. At 2 nm of separation the strongest region of the plasmonic field moved away from the corners of the cubes to the center of the adjacent faces. Different behavior is observed for the heterodimer. As the gold and silver cubes moved closer together, their plasmon modes mixed to form hybrid modes. Gold's dipolar mode weakly mixed with silver's higher energy dipolar mode. As a result, this hybrid mode enhanced the E-field primarily around the gold nanocube. Due to their similar energies, silver's dipolar mode mixed with the nonplasmonic interband transition of gold. Since the interband transition results from an incoherent excitation, it yields no E-field and this hybrid mode had a weaker enhancement than the unhybridized silver mode.

5.5 Experimental

In our study we looked at cubes and pairs of cubes with a side length of 42 nm. Each dipole occupied 1 nm^3 leading to 74088 dipoles for calculations with a single cube and 148176 dipoles for the dimers. The interparticle separation between the pairs was varied. The refractive index of gold or silver was assumed to be the same as that of the bulk metal. [2-3] [2-3] [2-3] This is a standard assumption for gold and silver nanoparticles. The refractive index of the surrounding medium was set to equal 1.33 (that of water) at all wavelengths. Although the refractive index of water varies with wavelength (and indeed has an imaginary component), the variation over of the visible spectrum is quite small. Plasmon resonance spectra were calculated for light propagated parallel to the interparticle axis. The plasmonic field intensification factor (in log scale of $|E|^2/|E_0|^2$) located on the surface of a pair of cubes and

calculated with the DDA technique at different excitation wavelengths. For these calculations, we used the DDSCAT 6.1 code developed by Draine and Flatau.

5.6 References

1. Mie, G., Beiträge zur Optik trüber Medien, speziell kolloidaler Metallösungen. *Annalen der physik* **1908,** *330* (3), 377-445.

2. El-Sayed, I. H.; Huang, X.; El-Sayed, M. A., Surface Plasmon Resonance Scattering and Absorption of anti-EGFR Antibody Conjugated Gold Nanoparticles in Cancer Diagnostics: Applications in Oral Cancer. *Nano Lett.* **2005,** *5* (5), 829-834.

3. Sokolov, K.; Follen, M.; Aaron, J.; Pavlova, I.; Malpica, A.; Lotan, R.; Richards-Kortum, R., Real-time vital optical imaging of precancer using anti-epidermal growth factor receptor antibodies conjugated to gold nanoparticles. *Cancer Res* **2003,** *63* (9), 1999-2004.

4. Alivisatos, P., The use of nanocrystals in biological detection. *Nat Biotech* **2004,** *22* (1), 47-52.

5. Haes, A. J.; Hall, W. P.; Chang, L.; Klein, W. L.; Van Duyne, R. P., A Localized Surface Plasmon Resonance Biosensor: First Steps toward an Assay for Alzheimer's Disease. *Nano Lett.* **2004,** *4* (6), 1029-1034.

6. Rosi, N. L.; Mirkin, C. A., Nanostructures in Biodiagnostics. *Chem. Rev.* **2005,** *105* (4), 1547-1562.

7. Hirsch, L. R.; Stafford, R. J.; Bankson, J. A.; Sershen, S. R.; Rivera, B.; Price, R. E.; Hazle, J. D.; Halas, N. J.; West, J. L., Nanoshell-mediated near-infrared thermal therapy of tumors under magnetic resonance guidance. *Proceedings of the National Academy of Sciences of the United States of America* **2003,** *100* (23), 13549-54.

8. Huang, X.; El-Sayed, I. H.; Qian, W.; El-Sayed, M. A., Cancer cell imaging and photothermal therapy in the near-infrared region by using gold nanorods. *J. Am. Chem. Soc.* **2006,** *128* (6), 2115-20.

9. Huang, X.; Jain, P. K.; El-Sayed, I. H.; El-Sayed, M. A., Determination of the Minimum Temperature Required for Selective Photothermal Destruction of Cancer Cells with the Use of Immunotargeted Gold Nanoparticles. *Photochem. Photobiol.* **2006,** *82* (2), 412-417.

10. Jain, P. K.; El-Sayed, I. H.; El-Sayed, M. A., Au nanoparticles target cancer. *nano today* **2007,** *2* (1), 18-29.

11. Michaels, A. M.; Jiang; Brus, L., Ag Nanocrystal Junctions as the Site for Surface-Enhanced Raman Scattering of Single Rhodamine 6G Molecules. *J. Phys. Chem. B* **2000,** *104* (50), 11965-11971.

12. Nie, S.; Emory, S. R., Probing Single Molecules and Single Nanoparticles by Surface-Enhanced Raman Scattering. *Science* **1997,** *275* (5303), 1102-1106.

13. Rechberger, W.; Hohenau, A.; Leitner, A.; Krenn, J. R.; Lamprecht, B.; Aussenegg, F. R., Optical properties of two interacting gold nanoparticles. *Opt. Commun.* **2003,** *220* (1–3), 137-141.

14. Su, K. H.; Wei, Q. H.; Zhang, X.; Mock, J. J.; Smith, D. R.; Schultz, S., Interparticle Coupling Effects on Plasmon Resonances of Nanogold Particles. *Nano Lett.* **2003,** *3* (8), 1087-1090.

15. Jain, P. K.; Huang, W.; El-Sayed, M. A., On the Universal Scaling Behavior of the Distance Decay of Plasmon Coupling in Metal Nanoparticle Pairs: A Plasmon Ruler Equation. *Nano Lett.* **2007,** *7* (7), 2080-2088.

16. Reinhard, B. M.; Siu, M.; Agarwal, H.; Alivisatos, A. P.; Liphardt, J., Calibration of Dynamic Molecular Rulers Based on Plasmon Coupling between Gold Nanoparticles. *Nano Lett.* **2005,** *5* (11), 2246-2252.

17. Grillet, N.; Manchon, D.; Bertorelle, F.; Bonnet, C.; Broyer, M.; Cottancin, E.; Lermé, J.; Hillenkamp, M.; Pellarin, M., Plasmon Coupling in Silver Nanocube Dimers: Resonance Splitting Induced by Edge Rounding. *ACS Nano* **2011,** *5* (12), 9450-9462.

18. Draine, B. T.; Flatau, P. J., Discrete-dipole approximation for scattering calculations. *J. Opt. Soc. Am. A* **1994,** *11* (4), 1491-1499.

19. Jain, P. K.; Lee, K. S.; El-Sayed, I. H.; El-Sayed, M. A., Calculated Absorption and Scattering Properties of Gold Nanoparticles of Different Size, Shape, and Composition: Applications in Biological Imaging and Biomedicine. *J. Phys. Chem. B* **2006,** *110* (14), 7238-7248.

20. Kelly, K. L.; Coronado, E.; Zhao, L. L.; Schatz, G. C., The Optical Properties of Metal Nanoparticles: The Influence of Size, Shape, and Dielectric Environment. *J. Phys. Chem. B* **2002,** *107* (3), 668-677.

21. Coronado, E. A.; Schatz, G. C., Surface plasmon broadening for arbitrary shape nanoparticles: A geometrical probability approach. *J. Chem. Phys.* **2003,** *119* (7), 3926-3934.

22. Hao, E.; Schatz, G. C., Electromagnetic fields around silver nanoparticles and dimers. *J. Chem. Phys.* **2004,** *120* (1), 357-366.

23. Jensen, T.; Kelly, L.; Lazarides, A.; Schatz, G., Electrodynamics of Noble Metal Nanoparticles and Nanoparticle Clusters. *J. Cluster Sci.* **1999,** *10* (2), 295-317.

24. Kelly, K. L.; Lazarides, A. A.; Schatz, G. C., Computational Electromagnetics of Metal Nanoparticles and Their Aggregates. *Computing in Science and Engg.* **2001,** *3* (4), 67-73.

25. Lorentz, H. A., *The Theory of Electrons and Its Applications to the Phenomena of Light and Radiant Heat: A Course of Lectures Delivered in Columbia University, New York, in March and April, 1906*. Columbia University Press: 1909; Vol. 29.

26. Fano, U., Effects of configuration interaction on intensities and phase shifts. *Physical Review* **1961,** *124* (6), 1866.

27. Bachelier, G.; Russier-Antoine, I.; Benichou, E.; Jonin, C.; Del Fatti, N.; Vallée, F.; Brevet, P.-F., Fano profiles induced by near-field coupling in heterogeneous dimers of gold and silver nanoparticles. *Phys. Rev. Lett.* **2008,** *101* (19), 197401.

28. Fan, J. A.; Bao, K.; Wu, C.; Bao, J.; Bardhan, R.; Halas, N. J.; Manoharan, V. N.; Shvets, G.; Nordlander, P.; Capasso, F., Fano-like interference in self-assembled plasmonic quadrumer clusters. *Nano Lett.* **2010,** *10* (11), 4680-4685.

29. Sheikholeslami, S.; Jun, Y.-w.; Jain, P. K.; Alivisatos, A. P., Coupling of Optical Resonances in a Compositionally Asymmetric Plasmonic Nanoparticle Dimer. *Nano Lett.* **2010,** *10* (7), 2655-2660.

30. Atay, T.; Song, J.-H.; Nurmikko, A. V., Strongly Interacting Plasmon Nanoparticle Pairs: From Dipole−Dipole Interaction to Conductively Coupled Regime. *Nano Lett.* **2004,** *4* (9), 1627-1631.

31. Marhaba, S.; Bachelier, G.; Bonnet, C.; Broyer, M.; Cottancin, E.; Grillet, N.; Lerme , J.; Vialle, J.-L.; Pellarin, M., Surface Plasmon Resonance of Single Gold Nanodimers near the Conductive Contact Limit. *J. Phys. Chem. C* **2009,** *113* (11), 4349-4356.

32. Lombardi, A.; Grzelczak, M. P.; Pertreux, E.; Crut, A.; Maioli, P.; Pastoriza-Santos, I.; Liz-Marzán, L. M.; Vallée, F.; Del Fatti, N., Fano Interference in the Optical Absorption of an Individual Gold–Silver Nanodimer. *Nano Letters* **2016,** *16* (10), 6311-6316.

33. Johnson, P. B.; Christy, R. W., Optical Constants of the Noble Metals. *Physical Review B* **1972,** *6* (12), 4370-4379.

34. Jain, A.; Ong, S. P.; Hautier, G.; Chen, W.; Richards, W. D.; Dacek, S.; Cholia, S.; Gunter, D.; Skinner, D.; Ceder, G.; Persson, K. A., Commentary: The Materials Project: A materials genome approach to accelerating materials innovation. *APL Materials* **2013,** *1* (1), 011002.

35. Raj, A. M. E.; Victoria, S. G.; Jothy, V. B.; Ravidhas, C.; Wollschläger, J.; Suendorf, M.; Neumann, M.; Jayachandran, M.; Sanjeeviraja, C., XRD and XPS characterization of mixed valence Mn 3 O 4 hausmannite thin films prepared by chemical spray pyrolysis technique. *Applied Surface Science* **2010,** *256* (9), 2920-2926.

36. Sherman, P. D., Galileo and the inclined plane controversy. *The Physics Teacher* **1974,** *12* (6), 343-348.

37. Hecht, S., PHOTOCHEMISTRY OF VISUAL PURPLE: I. THE KINETICS OF THE DECOMPOSITION OF VISUAL PURPLE BY LIGHT. *The Journal of general physiology* **1920,** *3* (1), 1.

CHAPTER 6 – GOLD/METAL OXIDE HYBRID NANOPARTICLES

6.1 Introduction

Nanoparticles have been an especially active area of chemical research over the past two decades. Some of the effusive praise of nanoscience has been hype but it is clear that nanoparticles have made a demonstrable impact in a number of fields including sensing[4], microscopy[5-6], and catalysis[6-7]. Nanoparticles offer two advantages as catalysts: 1) they have a significant specific surface area and 2) control of their exposed crystal facets can impact their activity. Although nanoparticles can be made of a variety of classes of materials (polymers, metal oxides, and semiconductors), catalysis research has focused on metallic semiconductors – in particular the group 10 and 11 transition metals.

Metallic nanoparticles have been produced since, at least, the 4th century CE.[8-9] Their optical properties were first systematically investigated by Faraday.[10] Since then gold[11], copper[12], silver[13], platinum[14], palladium[15], nickel[16], and many other metals have been made into spheres[17], cubes[11], pyrimids[18], octohedra[19], and even more exotic shapes. In many ways the synthesis of metal oxide nanoparticles has lagged behind their metallic counterparts. To be sure, there are a number of classics of oxide synthesis – the Stöber process for SiO_2 nanospheres, for instance[20] – but there is still a lot of space to explore in the shape and size control of metal oxides.

A number of factors complicate the controlled synthesis of metal oxides. 1) Many metal oxides are soluble in water necessitating the use of capping materials or organic solvents. 2) The strength of ionic bonds creates a high barrier to rearrangement leading to trapping of

defects. This produces branched structures.[21] 3) Some oxidation states are unstable in the presence of oxygen – e.g. magnetite - which complicates their synthesis and use.[22] Nevertheless, oxide nanoparticles have already seen numerous applications with heterogeneous catalysis leading the field.

Historically, metal oxides have found great success as supports for metallic catalysts. SiO_2, Al_2O_3, and TiO_2 are used to support noble metals and metal complexes for hydrogenation[23], oxidation[24], olefin metathesis[25], and hydroformylation[26]. This can be accomplished with both large, but porous structures like zeolites[27] or with nanoparticles. Of course, metal oxides have a number of properties which make them useful as catalysts themselves.

In many ways oxides are superior to native metals like gold or platinum as catalysts. 1) As any organometallic chemist will say, transition metal complexes are valuable for catalysis because they have a variety of accessible oxidation states - this facilitates the necessary redox chemistry. Their oxides behave similarly. 2) Their surface is populated by two distinct binding site for substrates – the metal centers and the oxygens. By providing two chemical environments, the range of catalyzable reactions is increased. 3) Most oxides are semiconductors many of which have band gaps in the visible region. This opens the way for interesting photocatalytic reactions utilizing sunlight.

One promising direction in nanocatalysis involves the fusion of metal and metal oxides into hybrid nanostructures which can harness the strengths of each. An early example of this was the use of gold on TiO_2 nanostructures to facilitate water splitting.[28] TiO_2 is natively capable of splitting water, but UV irradiation is required.[29] When plasmonic gold nanoparticles are introduced onto the surface of the TiO_2, visible light can be used instead. This type of

synergistic interaction can result from a number of effects – hot electron injection, charge separation, and plasmonic enhancement of light absorption.

6.1.1 Hybrid Effects

As discussed in detail in earlier chapters, nanoparticles of certain metals exhibit plasmonic resonances. This grants the nanoparticle fantastically enhanced absorption/scattering well beyond what the bulk material possesses.[30] The incredible electric fields present around these particles can enhance the photoproperties of adjacent systems – fluorescence, absorption, etc.[31] These can augment the catalytic behaviors of metal oxides. Figure 6-1 shows the possible mechanisms by which this can occur.

Plasmonic nanoparticles may enhance catalysis with semiconductors by directly improving their light absorption. It has been shown that gold nanoparticles increase the amount of light absorbed by Si[32-33], GaAs[34], Ge[35], and SnO_2[36]. This enhancement is attributed to the strong local electric fields caused by the plasmons. The only requirement is that the semiconductor's absorption band overlaps with the plasmonic resonance. This same type of enhancement should easily occur for any metal oxides with absorbance in the visible region.

When plasmonic nanoparticles absorb light, their conduction band electrons exist for a few hundred femtoseconds in an excited state. Since they are not in thermal equilibrium with the surrounding crystal lattice they are termed "hot electrons". If there is a Shottky barrier present, the electrons can be injected in to the adjacent semiconductor with some probability dependent on their energy and the density of states in the semiconductor's conduction band.[37-38] As the electron cools and moves into lower energy states in the semiconductor (including trap states), its probability of transfer back to the metal is reduced because the transfer becomes less energetically favorable. The injection process for gold on TiO_2 has a timescale

of about 50 fs and the back-transfer process has a timescale of over 1 ns.[39] This provides sufficient time for the separated charges to perform catalytic work before recombination.

The reverse process is also effective for narrow bandgap semiconductors. After the semiconductor absorbs visible light, it will inject electrons into adjacent metal nanoparticles. The timescale of the recombination is slowed by the presence of a Shottky barrier. Our lab has previously observed this behavior in Cu_2O-Au systems.[40] The increased lifetime of charge separation improved the catalytic degradation of methylene blue. It should be noted that this mechanism (unlike the others described here) does not require the metal nanoparticles to be plasmonic.

Ultrafast kinetics measurements are an excellent set of tools for better understanding these processes and seeing which play a role in different catalytic processes. The most thoroughly investigated mechanism is hot electron injection. Pump-probe spectroscopy has been used to study the kinetics of injection from gold nanoparticles into TiO_2 by measuring the concentration of conduction band electrons in the TiO_2.[39] Similar experiments were performed to measure the lifetime of injected electrons as a function of TiO_2 morphology – timescales were found to vary from 1-30 ns.[41] Cushing *et al.* have tried to distinguish between hot electron injection and absorption enhancement by placing an insulating layer of silica between the gold/silver and TiO_2.[42] They used ultrafast measurements to study the lifetimes of the charge carriers finding that electrons injected from the metal had significantly longer lifetimes than excitons created in the oxide. Similar work on other oxides is noticeably lacking.

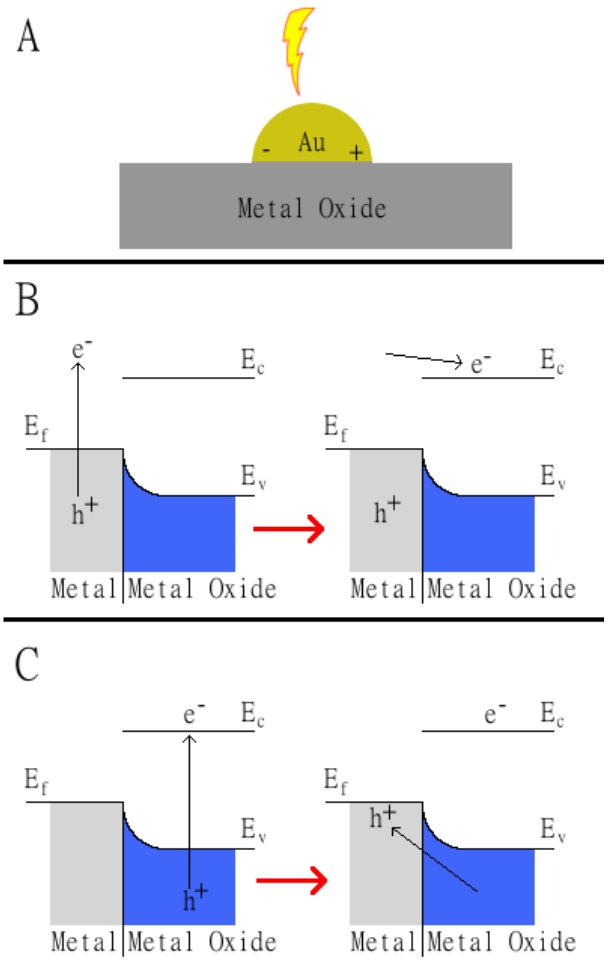

Figure 6-1. Catalytic enhancement mechanism of gold nanoparticles. (A) Plasmonic nanoparticles create strong electric fields in their vicinity, this can enhance the absorption of semiconductors. (B) If a plasmonic material absorbs light it can inject hot electrons into the semiconductor creating separation of the charge carriers and driving catalysis. (C) The metal oxide can absorb light and transfer a hole to the metal.

6.1.2 Purpose of work

To explore the use of hybrid metal/metal oxide nanoparticles for catalysis we set out to produce new structures. To begin, we narrowed down the range of materials under consideration. We focused on materials which could reasonably serve as economical catalysts and selected cheap, earth-abundant metals to serve as the metal oxide constituent. Manganese and vanadium were selected as targets for investigation. These constitute 0.8% and 0.05% of atoms in the Earth's crust respectively.[43] Although the amounts of manganese and vanadium are low in comparison to other first row metals, they are still quite cheap: manganese costs about $2/kg and vanadium about $12/kg.

The second consideration was stability in aqueous environments. It would be ideal to perform catalysis in water because it is cheap and easy to recycle. Since nanostructures have such a high surface area it is essential that the selected metal have an oxide form which is stable - does not oxidize, reduce, or dissolve – under typical conditions found in water. Pourbaix diagrams from the Materials Project guided this screening (Figure 6-2).[6, 44] Both metals exhibit regions where a solid oxide phase is stable in water but Mn requires high pH whereas V requires something closer to neutral.

Vanadium oxides are found in a variety of oxidation states including VO, V_2O_3, VO_2, and V_2O_5. Of these V_2O_5 is the most common catalyst being used in the production of sulfuric acid.[45] VO_2 is the most studied for nanomaterials because it exhibits unusual optical properties: at 68 °C it undergoes a reversible phase transition from a semiconducting to metallic state.[46] Although this is not necessarily useful for catalysis it does mean that there is a substantial literature describing the synthesis of VO_2 in a wide range of morphologies. Nanobelts[47], nanorods[48], nanospheres[49], and other shapes of vanadium dioxide have been produced.

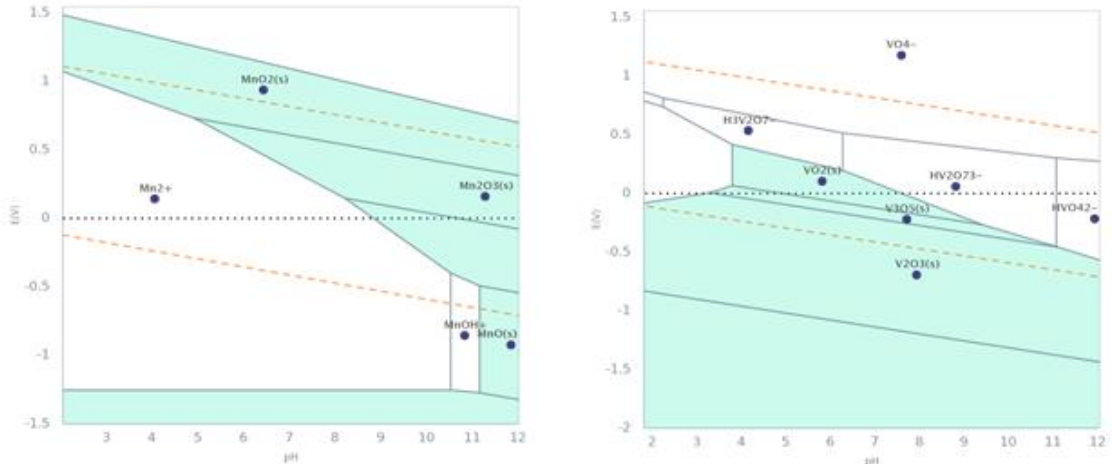

Figure 6-2. Pourbaix diagrams for manganese and vanadium at concentrations of 1 mM at 25 °C. The dashed orange lines indicate the points at which water decomposes to O_2 and H_2. Blue shaded regions show solid phases. Diagrams produced by the Materials Project.[2]

Like vanadium, manganese exhibits stable oxides in a variety of oxidation states. All of these have seen use as catalysts. MnO_2 has been used for ozone reduction[50], and oxidation of exhaust VOCs[51]; Mn_2O_3 for alkane oxidation[52], and water oxidation[53] and; amorphous Mn_2O_3/Mn_3O_4 for NOx reduction[54], and alcohol oxidation[55]. All of these oxides are attractive as photocatalysts because they have significant absorption in the visible spectrum.

The partial oxidation of alcohol is particularly interesting. MnO_4 is known to react stoichiometrically with supercritical isopropanol converting to lower oxidation states but not to manganese metal.[56] This bodes well for its utility as a catalyst because incorporating a zero valence metal into a catalytic cycle is difficult. The total oxidation of isopropanol on the surface of manganese oxides has been observed.[57] IR studies have demonstrated that isopropanol proceeds through a multistep oxidation with different products being produced at different temperatures. First, it binds to the surface of the manganese as an alkoxide. This converts to acetone around 500 K via oxy-dehydrogenation which can desorb from the surface.[58] At higher temperatures, the acetone is further oxidized to CO_2. This mechanism gives good conversion

(around 80%) but poor selectivity for the partial oxidation steps. Better selectivity for acetone can be had at room temperature under photocatalytic conditions.[59] Unfortunately, this dropped the conversion to under 10%.

A typical synthesis of MnO_x nanoparticles begins dissolving a soluble Mn^{2+} salt and oxidizing it in the presence of some growth directing agent. $KMnO_4$ is often employed as the oxidant because it removes the risk of introducing impurities.[60] An alternative approach involves basifying the solution and allowing dissolved oxygen to act as oxidant. As Figure 6-2 indicates, a high pH favors the formation of insoluble oxides. Using various Mn precursors and oxidants, a range of morphologies have been synthesized in different oxidation states - Table 6-1 shows a summary of these results. Some syntheses require high temperature/pressure conditions.[61]

Table 6-1. Examples of manganese oxide nanoparticle shapes.

Reference	Shape	Size (nm)	Oxidation State
62	Hollow nanospheres	20	+2, +3
61	Nanorods	2000 diam.	+2, +3, +3/4
63	Oblongs	50	+2, +3/4
64	Stars	200	+2
65	Dumbbells	150	+2
66	Wires	10000 len.	+2

6.2 Results and Discussion

6.2.1 Vanadium dioxide

We prepared vanadium dioxide nanoparticles using an adaptation of Son *et al*'s sol-gel approach.[67] This involved dissolving the V_2O_5 precursor in acidified solution and reducing it to a soluble V^{4+} species with hydrazine hydrate. This was precipitated as a complex oxide-

hydroxide network by raising the pH with NaOH. The black crystalline oxide was obtained by a hydrothermal reaction in a sealed reaction vessel in the presence of citrate. The high temperature was necessary to convert the oxide-hydroxide into a pure crystalline oxide. The citrate likely acted as a directing agent.

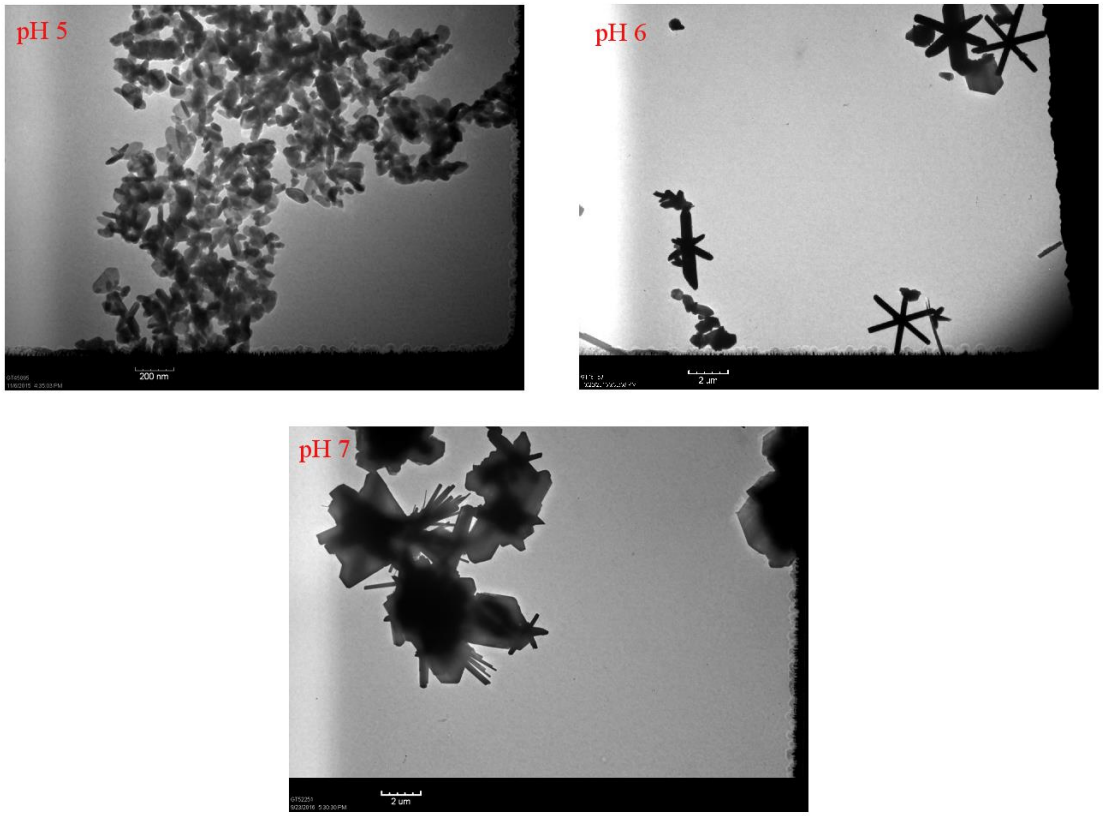

Figure 6-3. TEM images of VO_2 nanoparticles synthesized at various pHs.

The final pH during basification of the V^{4+} provided control over the final morphology of the vanadium crystals. A lower pH below 5 yielded small bumpy rod-likes shapes. A pH of 6 gave striking six-armed stars. High pHs produced multiarmed stars and plates exhibiting crystal twinning. TEM images of these particles are shown in Figure 6-3. In general, smaller particles were produced in more acidic conditions.

Powder x-ray diffraction was used to determine the phase of the VO_2. Samples were dried at 100 ^{0}C but were otherwise unannealed. The diffraction pattern is shown in Figure 6-4. There is a good match with the pattern for the monoclinic M phase (VO_2(M)) and no peaks from the monoclinc B phase or the tetragonal rutile, R, phase.[48] This is surprise because most hydrothermal syntheses of VO_2 produce VO_2(B) and require an additional annealing step to reach the more useful VO_2(M). This includes heating at 550 ^{0}C in vacuum[68], heating at 700 ^{0}C in nitrogen[49], or heating with tungstic acid in solution at 280 ^{0}C.[47] By avoiding these steps, the synthesis is simplified. Additionally, the sharpness of the peaks is a good indication of high crystallinity.

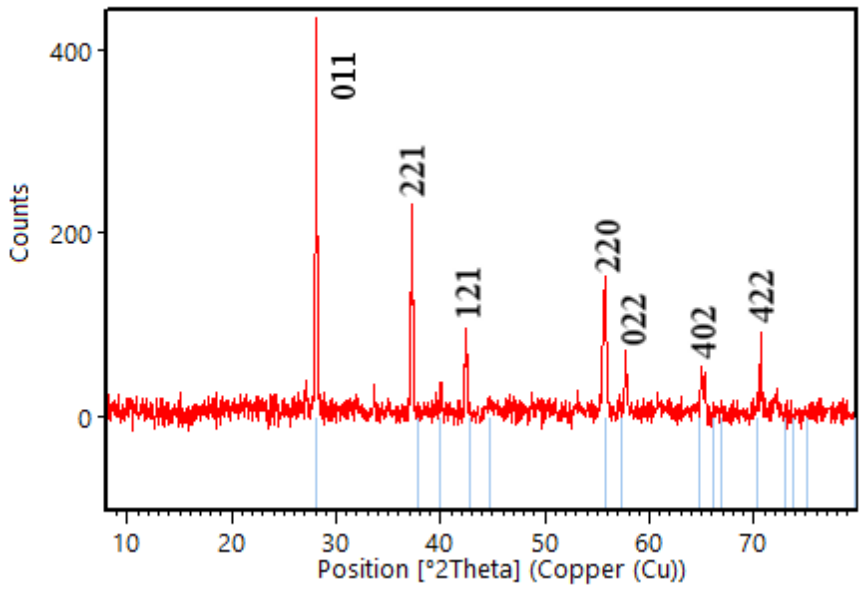

Figure 6-4. Powder x-ray diffraction pattern for the VO_2 nanoparticles. The blue lines show the reference pattern for monoclinic VO_2. The assignments are from Zhang et al.[48]

Initially we attempted to grow gold on the surface by performing a simple reduction of $HAuCl_4$ with sodium borohydride in the presence of VO_2 nanoparticles. This type of

procedure has been used previously to deposit gold on SiO_2[69], TiO_2[70], and Fe_3O_4[71]. Unfortunately, this failed to deposit gold on the surface of the VO_2. After reduction, the particles were centrifuged causing the VO_1 to precipitate out but leaving a red supernatant. The absorption spectrum of the supernatant was indicative of gold nanospheres. The typical mechanism for this type of growth involves individual gold atoms begin reduced with the metal oxide surface acting as a nucleation site. This gold atoms then serve as nucleation sites for the growth of larger gold particles. In the case of VO_2 it appears that the individual gold atoms are failing to adhere to the surface of the VO_2.

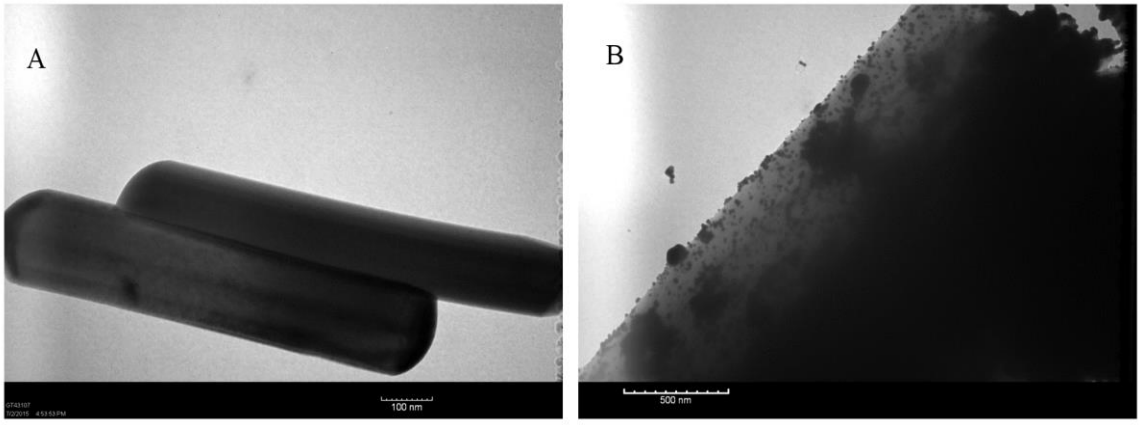

Figure 6-5. (A) Example of vanadium dioxide nanoparticles without gold on the surface. (B) Gold nanoparticles on the surface of a vanadium dioxide nanoparticle.

We attempted a modification of Lim *et al.*'s work on the production of a gold layer around silica nanoparticles.[69] They washed SiO_2 nanoparticles with a dilute solution of $SnCl_2$ leaving Sn^{2+} ions bound to the surface hydroxyls. When a dilute solution of $HAuCl_4$ was added the Au^{3+} oxidized the Sn^{2+} to Sn^{4+} leaving isolated gold atoms behind on the surface. To avoid the disproportionation that tin undergoes in water, the solution must be below a pH of 1.5. When this procedure was attempted with VO_2 particles, the promptly dissolved. To avoid this

problem we replaced the $SnCl_2$ with $FeCl_2$. Iron undergoes a similar redox reaction at a potential that is low enough for Au^{3+}. As far as we are aware, this procedure has not previously been utilized for the production of metallic nanoparticles on the surface of metal oxides. TEM imaging confirmed the presence of gold nanoparticle on the surface of the VO_2 (Figure 6-5). The gold nanoparticles are mostly less than 50 nm in diameter but some are as large as 300 nm.

6.2.2 Manganese Oxide

We aimed to produce Mn_3O_4 particles using a low temperature method that relies on dissolved oxygen as the oxidiant.[72] First, an appropriate manganese (II) salt is dissolved in water in the presence of some ligand. Then base is slowly added to the solution, producing $Mn(OH)_2$ which can be oxidized to an insoluble mixed Mn^{2+}/Mn^{3+} with a spinel crystal structure. The proposed overall reaction is as follows:

$$Mn^{2+}(aq) + 2OH^{-}(aq) \rightarrow Mn(OH)_2(aq) \quad (1)$$

$$6Mn(OH)_2(aq) + O_2(aq) \rightarrow 2Mn_3O_4(s) + 6H_2O \quad (2)$$

Nanoparticle synthesis generally proceeds by a two-step process. 1) Production of small seed particles. 2) Growth of these seed particles into larger particles with a well-defined shape. The specific conditions of both steps influence the final shape of the nanoparticles. Since dissolved oxygen is present in solution from the start, as soon as $Mn(OH)_2$ is produced it will begin to be oxidized. Thus the rate of addition of base, the temperature, and the concentration of Mn^{2+} will impact the number of Mn_3O_4 seed particles. The growth of the final particles will depend on the concentration of seed particles, temperature, and most importantly, the type and concentration of growth directing agent. Growth directing agents are ligands which preferentially bind to certain crystal facets of the material. If they preferentially bind, say, the (100) face, growth along this direction will be stunted and must

occur along a different axis – perhaps the (110). We explored the use of two different ligands to control the shape of Mn_3O_4 – cetrimonium bromide (CTAB), and citrate. These ligands are representative of two broadly used classes of directing agents, cationic surfactants and small carboxylates respectively.

Use of either ligand produced the same brown-orange solid upon addition of base. After washing with water to remove excess ligand, the CTAB capped particles formed small clumps (1-2 mm in size) in solution which were impossible to permanently disperse even with the application of sonication. After shaking, the particles would self-assemble into these structures after a few seconds. The citrate capped particles gave no such visible clumps. Figure 6-6 reveals that this difference is due to morphology differences between the two types of nanoparticles. Both reactions produced rod-like shapes. But whereas the CTAB rods have a length of well over 10 μm, the citrate particles are closer to 0.5 μm. (In both cases there are also rounder particles with a diameter of about 50 nm.) The CTAB particles are so long that they have formed a tangle which shows the origin of their clumping behavior in solution.

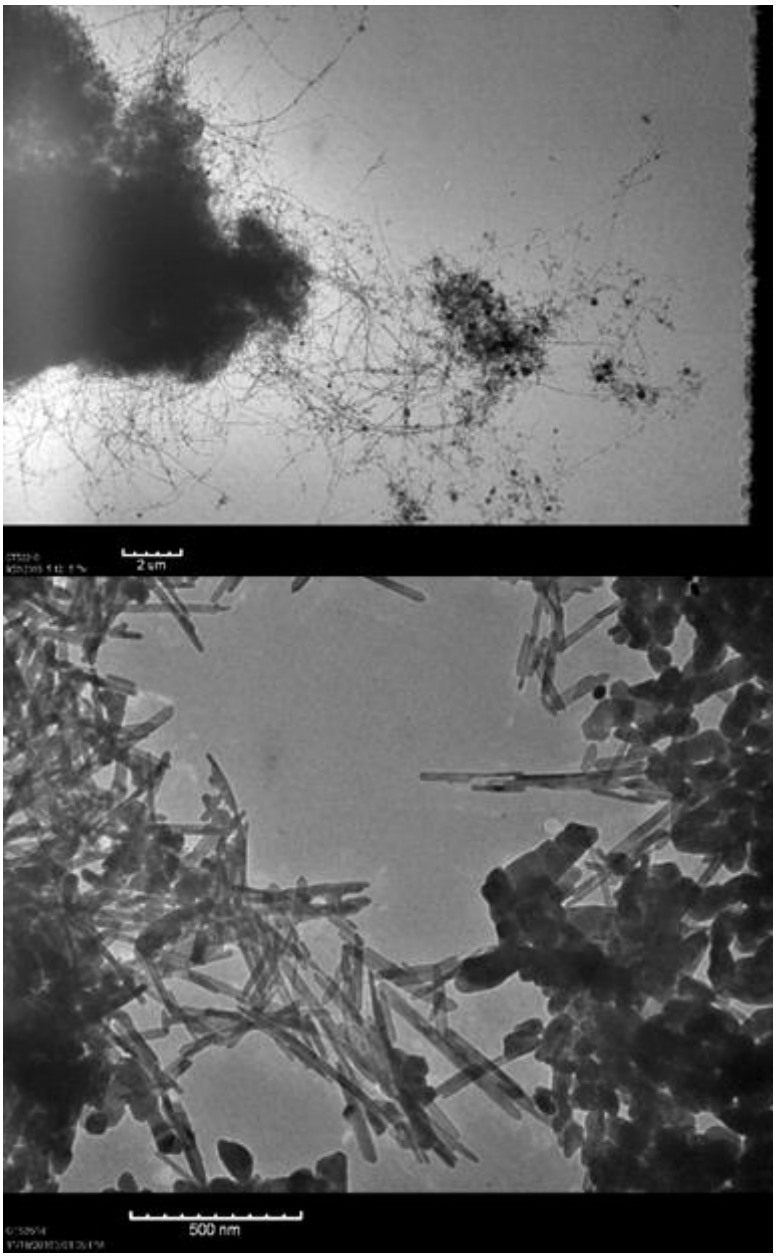

Figure 6-6. TEM micrographs of Mn_3O_4 particles with different capping agents: CTAB (A) and citrate (B).

We next investigated temperature as a route to shape control. Lowering the temperature should have two effects. 1) There should be fewer seeds which may lead to a smaller distribution of shapes and sizes and 2) the facet-selective binding of CTAB should be amplified at lower temperatures due to the reduction in available thermal energy. Reactions were run at 0, 22, 37, and 50 °C under otherwise identical conditions. The reaction mixture was cooled after the addition of CTAB to enable complete dissolution of the surfactant. Figure 6-7 shows the surprisingly diverse resultant particles. At low temperature long, thin wires are

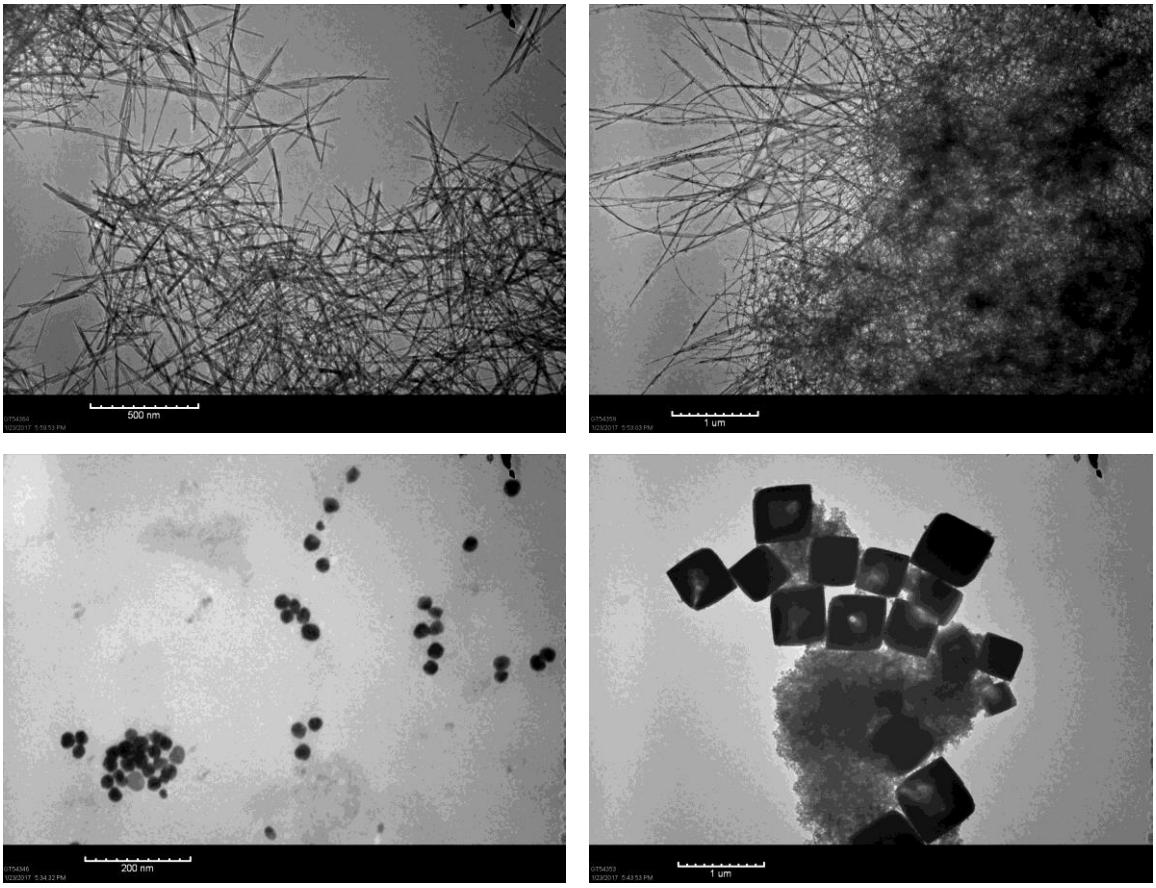

Figure 6-7. TEM micrographs of Mn_3O_4 nanoparticles synthesized at a variety of temperatures. 0 (A), 22 (B), 37 (C), and 50 °C (D).

produced. These are approximately 10 nm wide and vary from about 1 μm for the reaction at 0 °C and 10s of microns at room temperature. As the temperature was raised to 37 °C spheres with diameter of around 40 nm were produced. This result is not especially surprising – and is well known for metallic particles.[73] Oddly, as the temperature was raised further, the reaction produced large cubes with typical side lengths of around 500 nm.

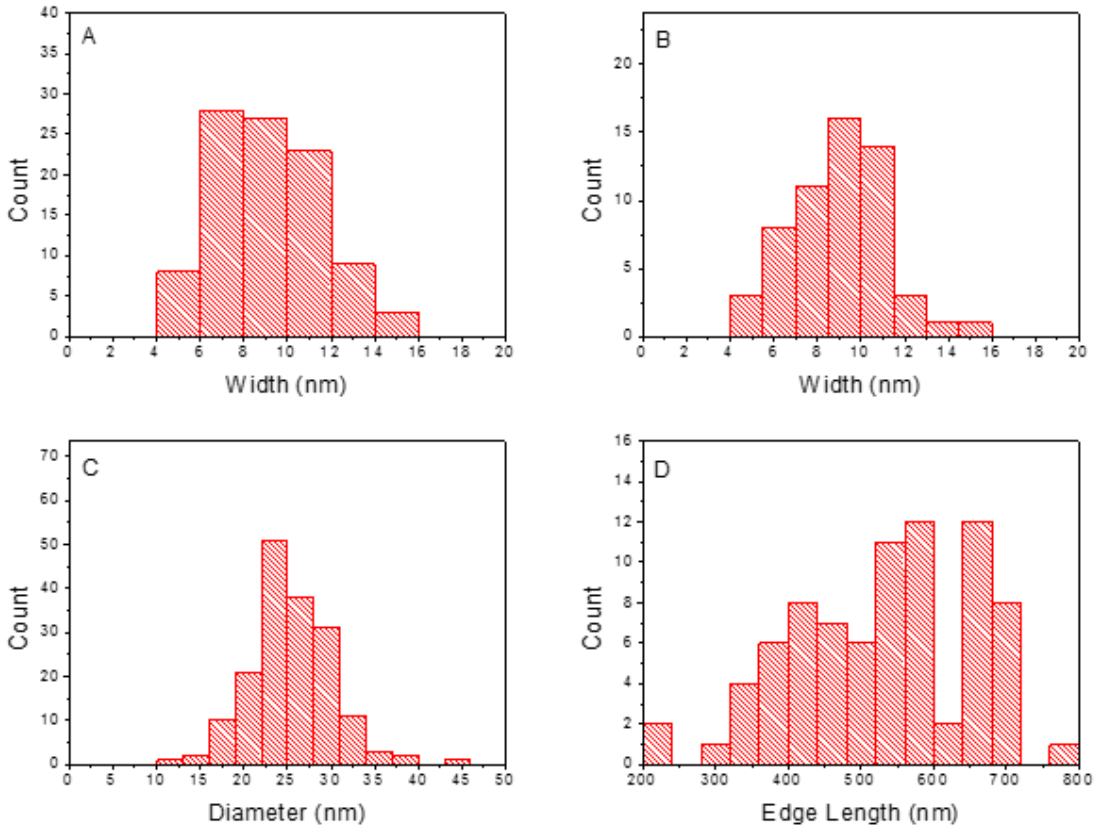

Figure 6-8. Mn_3O_4 particle size distributions for nanowires produced at 0 °C (A), nanowires produced at 22 °C (B), nanospheres produced at 37 °C (C), and nanocubes produced at 50 °C (D).

The size distributions of the nanoparticles were determined and are shown in Figure 6-8. The length of the nanowires could not be easily measured because of the challenge of

identifying both ends of nanowires within the tangles – instead the width was measured. The size distribution was quite good for all but the cubes. Large nanoparticles are frequently hard to grow in a single step. It usually works better to grow small particles first and then add additional material in a series of steps.

6.2.2.1 Characterization

XRD was used to determine the phase and oxidation state of the nanoparticles. The diffraction pattern of the as-synthesized manganese oxide nanoparticles is shown in Figure 6-9. There are no major peaks present indicating an amorphous form of the oxide – and is consistent with other syntheses of amorphous manganese oxide.[74-75] The sample was heated to 300 ^{o}C for one hour and slowly cooled to room temperature. No color change was observed. Manganese oxides are known to change oxidation state at higher temperatures. Mn_2O_3 is produces at 400 ^{o}C[76] and Mn_3O_4 at 900 ^{0}C[77]. Our annealing temperature was too low to produce a change of oxidation state. The powder diffraction pattern after annealing is a clear match for Mn_3O_4 – hausmannite.[1] This indicates that the nanoparticles began in the mixed (II/III) oxidation state but as an amorphous material.

6.2.2.2 Growth of Gold

The introduction of gold on to the surface was accomplished by a variation of the galvanic replacement method.[13] With this technique, a solution of gold (III) salt was added to the manganese nanoparticles. The Au^{3+} reduced the manganese to a lower oxidation state and deposited gold on the surface. Sodium borohydride solution was then added to ensure that all gold in solution was reduced to metallic gold on the surface. Adding only a small amount of gold relative to the amount of manganese present prevented degradation of the particles' structural integrity. When the particles were centrifuged at low speed the supernatant had no spectral features which would indicate free Au nanoparticles. This suggests that all the gold

was fixed to the surface of the manganese oxide nanoparticles. This was confirmed by dissolving the nanoparticle in water acidified to a pH of 2 with HCl. The acid dissolved the manganese oxide but left the gold unaffected. An absorption spectrum confirmed that gold nanoparticles were present by a clear LSPR peak at 540 nm – indicative of plasmonic gold nanospheres.

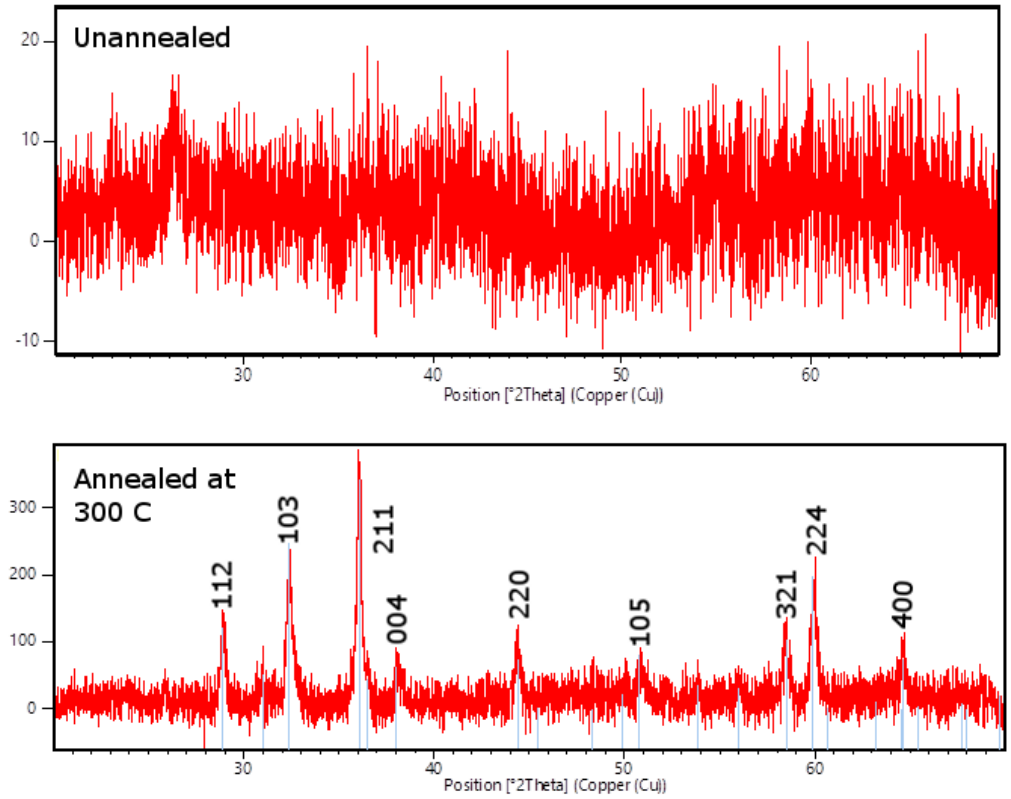

Figure 6-9. Powder x-xray diffraction plots for the manganese oxide nanoparticles. (Top) The diffraction pattern for the nanoparticles as synthesized - no major peaks are observed. (Bottom) The pattern after annealing at 300 ^{0}C for 1 hour produced a pattern which matched the structure of Mn_3O_4. The blue lines show the positions of literature peaks and the assignments are from Raj et al.[1]

This process was repeated at a variety of gold concentrations producing loadings of 1%, 5%, and 10%. TEM images of the as produced particles is shown in Figure 6-10. The gold

nanoparticles deposited on the surface show up much darker than the manganese oxide because of their higher electron density. The shape of the gold particles is roughly spherical but still quite irregular. This could be better controlled by the introduction of a capping agent for the gold. Citrate, CTAB, and polymers like polyvinylpyrrolidone are known to control the growth of gold nanospheres producing better more regular spheres with tight size distributions.[78-79]

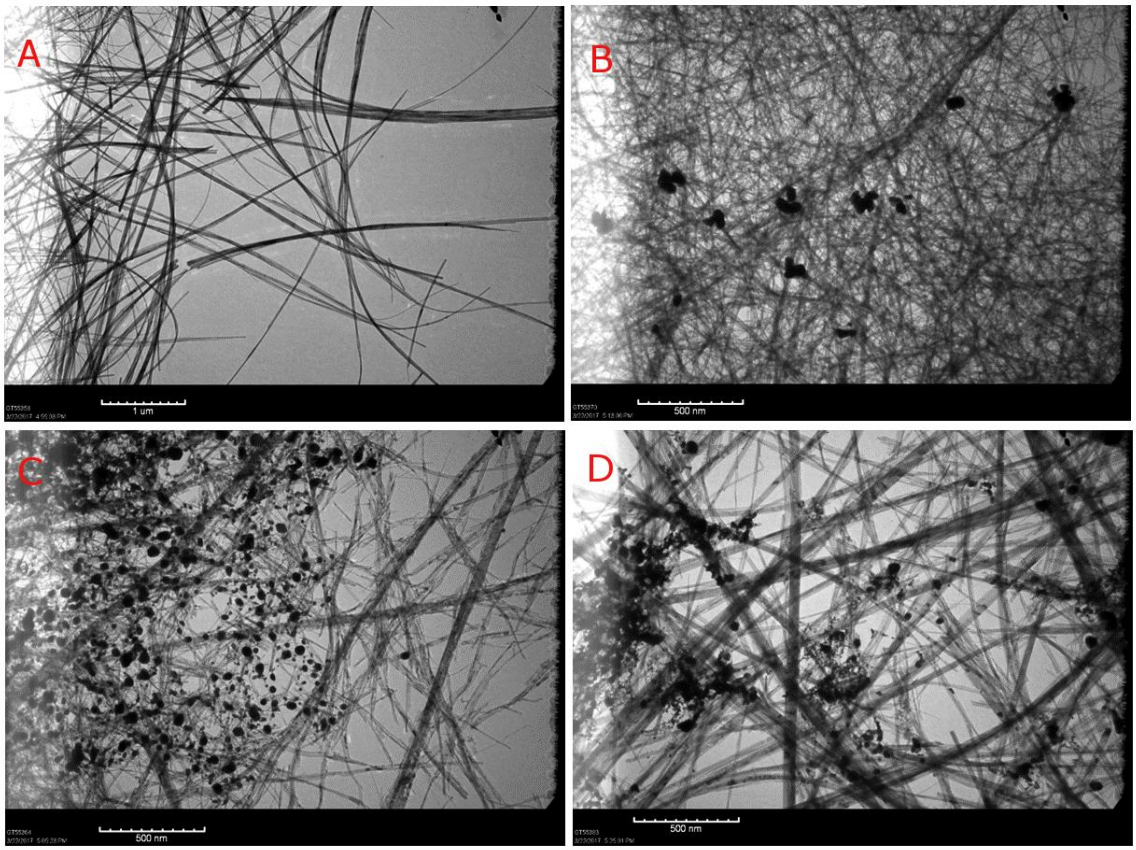

Figure 6-10. TEM images of Mn_3O_4 nanowires with gold deposited. (A) No gold. (B) 1% loading. (C) 5% loading. (D) 10% loading.

6.3 Future Work

The next step will be to utilize these hybrid particles to perform catalytic reactions and study how the presence of gold influences their activity. We will utilize the photooxidation of diphenylmethanol to benzophenone with oxygen as our model reaction. This partial oxidation of an alcohol is easy to follow because benzophenone has a near-UV absorption which can be tracked via absorption measurements. We intend to study the turnover rate as a function of metal oxide concentration and gold loading.

Ultrafast pump-probe measurements will be used to help understand how gold influences the reaction occurring. Both VO_2 and Mn_3O_4 absorb visible light. Although the ultrafast behavior of Mn_3O_4 is not well studied, pumping it at 400 nm produces a broad absorption in the visible due to the population of the conduction band. Thus the lifetime of conduction band electrons can be followed.

6.4 Experimental

6.4.1 VO_2 Nanoparticles

450 mg of V_2O_5 (2.47 mmol) were suspended in 100 mL H_2O. The solution was heated to 50 °C causing some, but not all of the V_2O_5 to dissolve giving a yellow-orange opaque suspension. 10 mL 98% sulfuric acid was slowly added with stirring. The suspension continued to be heated until all the V_2O_5 dissolved as a clear yellow solution. 0.5 mL hydrazine hydrate was added dropwise turning the solution green and then blue. This indicates the complete reduction of V^{5+} to V^{4+}. 10 M sodium hydroxide solution was added dropwise until a pH of 6 was reached. During this process a grey-blue precipitate formed. Over addition of base caused the precipitate to take on a reddish-brown color. The precipitate was centrifuged (5000 rpm, 5 minutes) and resuspended in water 3 times. The final pellet was transferred to Teflon lined

pressure reactor along with 20 mL H_2O and 120 mg trisodium citrate dihydrate (0.4 mmol). This vessel was sealed and heated to 220 °C for 48 hr. After cooling to room temperature the resultant black solid was collected by vacuum filtration and drying in the oven at 100 °C overnight. Yield = 77%.

6.4.2 Au/VO_2 Nanoparticles

60 mg of VO_2 nanoparticles (0.4 mmol) were dispersed in 10 mL H_2O with vigorous stirring. 20 mg $FeCl_2$ (0.11 mmol) was added and the solution was allowed to sit overnight. This suspension was centrifuged and the pellet was resuspended in water 5 times to remove any free ferrous ions present. A gold solution was prepared by diluting 100 μL of 60 mM $HAuCl_4$ to 5 mL with water and adding 10 mg potassium carbonate. This solution was aged overnight in the dark. 2 mL of the gold solution was added to the suspension of vanadium nanoparticles and was stirred for 10 minutes. Then 50 μL of 60 mM $HAuCl_4$ was added with vigorous stirring. 10 mM $NaBH_4$ solution (100 μL) was added slowly and caused a red-purple tint appear indicating the formation of gold nanoparticles. The solution was centrifuged (5000 rpm, 5 minutes) twice.

6.4.3 Mn_3O_4 Nanoparticles

In a typical synthesis, 190.0 mg of $MnSO_4 \cdot H_2O$ (1.12 mmol) was dissolved in 80 mL H_2O. 450.0 mg cetrimonium bromide (1.20 mmol) was added and stirred until dissolved yielding a clear or pale pink solution. The reaction flask was placed in a water bath of the desired temperature (0 °C – 80 °C). 50.0 mg of NaOH (1.25 mmol) was dissolved in 5 mL H_2O and added dropwise to the solution of Mn^{2+} with stirring. The solution rapidly turned orange-brown and was left to stir for 2 hours. The resulting solid was cleaned by centrifugation (1000 rpm, 2 minutes) and resuspension in H_2O five times to ensure removal of all free CTAB.

It is easiest to use the product by suspending in a known volume of water. Suspending all product in 25.0 mL gives a 0.92 mM suspension. Yield = 82%.

6.4.4 Au/Mn_3O_4 Nanoparticles

2 mL of 0.92 mM Mn_3O_4 was diluted with 8 mL H_2O. 0-200 mg of trisodium citrate was added. To this was added a variable amount of 60 mM $HAuCl_4$ (2-10 μL). The solution rapidly changed from orange-brown to a darker brown. 10 mM $NaBH_4$ solution (100 μL) was added slowly to ensure complete reduction of the gold. The resulting particles were cleaned by centrifugation (1000 rpm, 2 minutes).

6.4.5 TEM Imaging

Samples were prepared by depositing a dilute suspension on carbon coated copper TEM grids (Ted Pella) and waiting for evaporation. They were imaged on a JEOL 100 CX-II TEM at an accelerating voltage of 100 kV.

6.4.6 Powder XRD

Samples were prepared by drying the solid in a 100 ^{0}C oven overnight. The dried powder was ground in a mortar until an even consistency was reached. The powder was pressed into a 0.25 inch powder sample holder. Diffraction patterns were acquired on a Panalytical XPert PRO Alpha-1 XRD using a copper source.

6.5 References

1. Raj, A. M. E.; Victoria, S. G.; Jothy, V. B.; Ravidhas, C.; Wollschläger, J.; Suendorf, M.; Neumann, M.; Jayachandran, M.; Sanjeeviraja, C., XRD and XPS characterization of mixed valence Mn 3 O 4 hausmannite thin films prepared by chemical spray pyrolysis technique. *Applied Surface Science* **2010,** *256* (9), 2920-2926.

2. Liu, Q.; Wang, J.-K.; Zewail, A. H., Femtosecond dynamics of dissociation and recombination in solvent cages. *Nature* **1993,** *364* (6436), 427-430.

3. Schwartz, B. J.; Peteanu, L. A.; Harris, C. B., Direct Observation of Fast Proton Transfer: Femtosecond Photophysics of. *J. Phys. Chem* **1992,** *96*, 3591-3598.

4. Saha, K.; Agasti, S. S.; Kim, C.; Li, X.; Rotello, V. M., Gold nanoparticles in chemical and biological sensing. *Chem. Rev.* **2012,** *112* (5), 2739-2779.

5. Lei, D. Y.; Appavoo, K.; Sonnefraud, Y.; Haglund, J. R. F.; Maier, S. A., Single-particle plasmon resonance spectroscopy of phase transition in vanadium dioxide. *Opt. Lett.* **2010,** *35* (23), 3988-3990.

6. Jain, A.; Ong, S. P.; Hautier, G.; Chen, W.; Richards, W. D.; Dacek, S.; Cholia, S.; Gunter, D.; Skinner, D.; Ceder, G.; Persson, K. A., Commentary: The Materials Project: A materials genome approach to accelerating materials innovation. *APL Materials* **2013,** *1* (1), 011002.

7. Narayanan, R.; El-Sayed, M. A., Shape-dependent catalytic activity of platinum nanoparticles in colloidal solution. *Nano Lett.* **2004,** *4* (7), 1343-1348.

8. Colomban, P.; Tournie, A.; Ricciardi, P., Raman spectroscopy of copper nanoparticle-containing glass matrices: ancient red stained-glass windows. *Journal of Raman Spectroscopy* **2009,** *40* (12), 1949-1955.

9. Freestone, I.; Meeks, N.; Sax, M.; Higgitt, C., The Lycurgus cup—a roman nanotechnology. *Gold bulletin* **2007,** *40* (4), 270-277.

10. Faraday, M., The Bakerian lecture: experimental relations of gold (and other metals) to light. *Philosophical Transactions of the Royal Society of London* **1857,** *147*, 145-181.

11. Kim, F.; Connor, S.; Song, H.; Kuykendall, T.; Yang, P., Platonic gold nanocrystals. *Angew. Chem.* **2004,** *116* (28), 3759-3763.

12. Lee, Y.; Choi, J.-r.; Lee, K. J.; Stott, N. E.; Kim, D., Large-scale synthesis of copper nanoparticles by chemically controlled reduction for applications of inkjet-printed electronics. *Nanotechnology* **2008,** *19* (41), 415604.

13. Sun, Y.; Xia, Y., Shape-controlled synthesis of gold and silver nanoparticles. *Science* **2002,** *298* (5601), 2176-2179.

14. Ahmadi, T. S.; Wang, Z. L.; Green, T. C.; Henglein, A.; El-Sayed, M. A., Shape-controlled synthesis of colloidal platinum nanoparticles. *Science* **1996,** *272* (5270), 1924.

15. Teranishi, T.; Miyake, M., Size control of palladium nanoparticles and their crystal structures. *Chem. Mater.* **1998,** *10* (2), 594-600.

16. Wu, Z. G.; Munoz, M.; Montero, O., The synthesis of nickel nanoparticles by hydrazine reduction. *Adv. Powder Technol.* **2010,** *21* (2), 165-168.

17. Liang, H.; Wang, W.; Huang, Y.; Zhang, S.; Wei, H.; Xu, H., Controlled synthesis of uniform silver nanospheres. *J. Phys. Chem. C* **2010,** *114* (16), 7427-7431.

18. Jin, R.; Cao, Y.; Mirkin, C. A.; Kelly, K.; Schatz, G. C.; Zheng, J., Photoinduced conversion of silver nanospheres to nanoprisms. *Science* **2001,** *294* (5548), 1901-1903.

19. Tian, N.; Zhou, Z.-Y.; Sun, S.-G.; Ding, Y.; Wang, Z. L., Synthesis of tetrahexahedral platinum nanocrystals with high-index facets and high electro-oxidation activity. *science* **2007,** *316* (5825), 732-735.

20. Stöber, W.; Fink, A.; Bohn, E., Controlled growth of monodisperse silica spheres in the micron size range. *J. Colloid Interface Sci.* **1968,** *26* (1), 62-69.

21. Mehra, S.; Chan, E. M.; Salleo, A., Modular synthetic design enables precise control of shape and doping in colloidal zinc oxide nanorods. *Journal of Materials Chemistry C* **2015,** *3* (27), 7172-7179.

22. Laurent, S.; Forge, D.; Port, M.; Roch, A.; Robic, C.; Vander Elst, L.; Muller, R. N., Magnetic iron oxide nanoparticles: synthesis, stabilization, vectorization, physicochemical characterizations, and biological applications. *Chem. Rev.* **2008,** *108* (6), 2064-2110.

23. Al-Ammar, A. S.; Webb, G., Hydrogenation of acetylene over supported metal catalysts. Part 1.—Adsorption of [14 C] acetylene and [14 C] ethylene on silica supported rhodium, iridium and palladium and alumina supported palladium. *Journal of the Chemical Society, Faraday Transactions 1: Physical Chemistry in Condensed Phases* **1978,** *74*, 195-205.

24. Schimpf, S.; Lucas, M.; Mohr, C.; Rodemerck, U.; Brückner, A.; Radnik, J.; Hofmeister, H.; Claus, P., Supported gold nanoparticles: in-depth catalyst characterization and application in hydrogenation and oxidation reactions. *Catal. Today* **2002,** *72* (1), 63-78.

25. Vidal, V.; Théolier, A.; Thivolle-Cazat, J.; Basset, J.-M., Metathesis of alkanes catalyzed by silica-supported transition metal hydrides. *Science* **1997,** *276* (5309), 99-102.

26. Riisager, A.; Eriksen, K. M.; Wasserscheid, P.; Fehrmann, R., Propene and 1-octene hydroformylation with silica-supported, ionic liquid-phase (SILP) Rh-phosphine catalysts in continuous fixed-bed mode. *Catal. Lett.* **2003,** *90* (3), 149-153.

27. Laursen, A. B.; Højholt, K. T.; Lundegaard, L. F.; Simonsen, S. B.; Helveg, S.; Schüth, F.; Paul, M.; Grunwaldt, J. D.; Kegnæs, S.; Christensen, C. H., Substrate Size-Selective

Catalysis with Zeolite-Encapsulated Gold Nanoparticles. *Angew. Chem.* **2010,** *122* (20), 3582-3585.

28. Subramanian, V.; Wolf, E. E.; Kamat, P. V., Catalysis with TiO2/gold nanocomposites. Effect of metal particle size on the Fermi level equilibration. *J. Am. Chem. Soc.* **2004,** *126* (15), 4943-4950.

29. Fujishima, A.; Honda, K., Photolysis-decomposition of water at the surface of an irradiated semiconductor. *Nature* **1972,** *238* (5385), 37-38.

30. Link, S.; El-Sayed, M. A., Spectral Properties and Relaxation Dynamics of Surface Plasmon Electronic Oscillations in Gold and Silver Nanodots and Nanorods. *J. Phys. Chem. B* **1999,** *103* (40), 8410-8426.

31. Tam, F.; Goodrich, G. P.; Johnson, B. R.; Halas, N. J., Plasmonic enhancement of molecular fluorescence. *Nano Lett.* **2007,** *7* (2), 496-501.

32. Lim, S.; Mar, W.; Matheu, P.; Derkacs, D.; Yu, E., Photocurrent spectroscopy of optical absorption enhancement in silicon photodiodes via scattering from surface plasmon polaritons in gold nanoparticles. *J. Appl. Phys.* **2007,** *101* (10), 104309.

33. Schaadt, D.; Feng, B.; Yu, E., Enhanced semiconductor optical absorption via surface plasmon excitation in metal nanoparticles. *Appl. Phys. Lett.* **2005,** *86* (6), 063106.

34. Nakayama, K.; Tanabe, K.; Atwater, H. A., Plasmonic nanoparticle enhanced light absorption in GaAs solar cells. *Appl. Phys. Lett.* **2008,** *93* (12), 121904.

35. Tang, L.; Kocabas, S. E.; Latif, S.; Okyay, A. K.; Ly-Gagnon, D.-S.; Saraswat, K. C.; Miller, D. A., Nanometre-scale germanium photodetector enhanced by a near-infrared dipole antenna. *Nature Photonics* **2008,** *2* (4), 226-229.

36. Shen, Q.; Jiang, J.; Liu, S.; Han, L.; Fan, X.; Fan, M.; Fan, Q.; Wang, L.; Huang, W., Facile synthesis of Au–SnO 2 hybrid nanospheres with enhanced photoelectrochemical biosensing performance. *Nanoscale* **2014,** *6* (12), 6315-6321.

37. Clavero, C., Plasmon-induced hot-electron generation at nanoparticle/metal-oxide interfaces for photovoltaic and photocatalytic devices. *Nature Photonics* **2014,** *8* (2), 95-103.

38. White, T. P.; Catchpole, K. R., Plasmon-enhanced internal photoemission for photovoltaics: theoretical efficiency limits. *Appl. Phys. Lett.* **2012,** *101* (7), 073905.

39. Furube, A.; Du, L.; Hara, K.; Katoh, R.; Tachiya, M., Ultrafast plasmon-induced electron transfer from gold nanodots into TiO2 nanoparticles. *J. Am. Chem. Soc.* **2007,** *129* (48), 14852-14853.

40. Mahmoud, M. A.; Qian, W.; El-Sayed, M. A., Following charge separation on the nanoscale in Cu2O–Au nanoframe hollow nanoparticles. *Nano Lett.* **2011,** *11* (8), 3285-3289.

41. Bian, Z.; Tachikawa, T.; Zhang, P.; Fujitsuka, M.; Majima, T., Au/TiO2 superstructure-based plasmonic photocatalysts exhibiting efficient charge separation and unprecedented activity. *J. Am. Chem. Soc.* **2013,** *136* (1), 458-465.

42. Cushing, S. K.; Li, J.; Bright, J.; Yost, B. T.; Zheng, P.; Bristow, A. D.; Wu, N., Controlling plasmon-induced resonance energy transfer and hot electron injection processes in Metal@ TiO2 core–shell nanoparticles. *J. Phys. Chem. C* **2015,** *119* (28), 16239-16244.

43. Taylor, S., Abundance of chemical elements in the continental crust: a new table. *Geochimica et cosmochimica acta* **1964,** *28* (8), 1273-1285.

44. Ong, S. P.; Cholia, S.; Jain, A.; Brafman, M.; Gunter, D.; Ceder, G.; Persson, K. A., The Materials Application Programming Interface (API): A simple, flexible and efficient API for materials data based on REpresentational State Transfer (REST) principles. *Computational Materials Science* **2015,** *97*, 209-215.

45. Mars, P.; Van Krevelen, D. W., Oxidations carried out by means of vanadium oxide catalysts. *Chem. Eng. Sci.* **1954,** *3*, 41-59.

46. Morin, F., Oxides which show a metal-to-insulator transition at the Neel temperature. *Phys. Rev. Lett.* **1959,** *3* (1), 34-36.

47. Zhang, K.-F.; Liu, X.; Su, Z.-X.; Li, H.-L., VO2(R) nanobelts resulting from the irreversible transformation of VO2(B) nanobelts. *Mater. Lett.* **2007,** *61* (13), 2644-2647.

48. Zhang, Y.; Zhang, X.; Huang, Y.; Huang, C.; Niu, F.; Meng, C.; Tan, X., One-step hydrothermal conversion of VO 2 (B) into W-doped VO 2 (M) and its phase transition and optical switching properties. *Solid State Commun.* **2014,** *180*, 24-27.

49. Kam, K. C.; Cheetham, A. K., Thermochromic VO2 nanorods and other vanadium oxides nanostructures. *Mater. Res. Bull.* **2006,** *41* (5), 1015-1021.

50. Li, W.; Gibbs, G.; Oyama, S. T., Mechanism of ozone decomposition on a manganese oxide catalyst. 1. In situ Raman spectroscopy and ab initio molecular orbital calculations. *J. Am. Chem. Soc.* **1998,** *120* (35), 9041-9046.

51. Kim, S. C.; Shim, W. G., Catalytic combustion of VOCs over a series of manganese oxide catalysts. *Applied Catalysis B: Environmental* **2010,** *98* (3), 180-185.

52. Tian, Z.-R.; Tong, W.; Wang, J.-Y.; Duan, N.-G.; Krishnan, V. V.; Suib, S. L., Manganese oxide mesoporous structures: mixed-valent semiconducting catalysts. *Science* **1997,** *276* (5314), 926-930.

53. Jiao, F.; Frei, H., Nanostructured cobalt and manganese oxide clusters as efficient water oxidation catalysts. *Energy & Environmental Science* **2010,** *3* (8), 1018-1027.

54. Kang, M.; Park, E. D.; Kim, J. M.; Yie, J. E., Manganese oxide catalysts for NOx reduction with NH 3 at low temperatures. *Applied catalysis A: general* **2007,** *327* (2), 261-269.

55. Chen, J.; Lin, J. C.; Purohit, V.; Cutlip, M. B.; Suib, S. L., Photoassisted catalytic oxidation of alcohols and halogenated hydrocarbons with amorphous manganese oxides. *Catal. Today* **1997,** *33* (1-3), 205-214.

56. Buslaeva, E. Y.; Kravchuk, K.; Kargin, Y. F.; Gubin, S., Reactions of MnO2, Mn2O3, α-Bi2O3, and Bi12Ti1–xMnxO20with Supercritical Isopropanol. *Inorganic materials* **2002,** *38* (6), 582-585.

57. Gallardo-Amores, J. M.; Armaroli, T.; Ramis, G.; Finocchio, E.; Busca, G., A study of anatase–supported Mn oxide as catalysts for 2-propanol oxidation. *Applied Catalysis B: Environmental* **1999,** *22* (4), 249-259.

58. Baldi, M.; Milella, F.; Ramis, G.; Escribano, V. S.; Busca, G., An FT-IR and flow reactor study of the selective catalytic oxy-dehydrogenation of C3 alcohols on Mn3O4. *Applied Catalysis A: General* **1998,** *166* (1), 75-88.

59. Cao, H.; Suib, S. L., Highly efficient heterogeneous photooxidation of 2-propanol to acetone with amorphous manganese oxide catalysts. *Journal of the American Chemical Society;(United States)* **1994,** *116* (12).

60. Djerdj, I.; Arcˇon, D.; Jagličić, Z.; Niederberger, M., Nonaqueous synthesis of manganese oxide nanoparticles, structural characterization, and magnetic properties. *J. Phys. Chem. C* **2007,** *111* (9), 3614-3623.

61. Ahmad, T.; Ramanujachary, K. V.; Lofland, S. E.; Ganguli, A. K., Nanorods of manganese oxalate: a single source precursor to different manganese oxide nanoparticles (MnO, Mn 2 O 3, Mn 3 O 4). *J. Mater. Chem.* **2004,** *14* (23), 3406-3410.

62. Shin, J.; Anisur, R. M.; Ko, M. K.; Im, G. H.; Lee, J. H.; Lee, I. S., Hollow manganese oxide nanoparticles as multifunctional agents for magnetic resonance imaging and drug delivery. *Angew. Chem., Int. Ed.* **2009,** *48* (2), 321-324.

63. Portehault, D.; Cassaignon, S.; Baudrin, E.; Jolivet, J.-P., Structural and morphological control of manganese oxide nanoparticles upon soft aqueous precipitation through MnO 4−/Mn 2+ reaction. *J. Mater. Chem.* **2009,** *19* (16), 2407-2416.

64. Zitoun, D.; Pinna, N.; Frolet, N.; Belin, C., Single crystal manganese oxide multipods by oriented attachment. *J. Am. Chem. Soc.* **2005,** *127* (43), 15034-15035.

65. Zhong, X.; Xie, R.; Sun, L.; Lieberwirth, I.; Knoll, W., Synthesis of dumbbell-shaped manganese oxide nanocrystals. *J. Phys. Chem. B* **2006,** *110* (1), 2-4.

66. Yuan, Z.-Y.; Zhang, Z.; Du, G.; Ren, T.-Z.; Su, B.-L., A simple method to synthesise single-crystalline manganese oxide nanowires. *Chem. Phys. Lett.* **2003,** *378* (3), 349-353.

67. Son, J.-H.; Wei, J.; Cobden, D.; Cao, G.; Xia, Y., Hydrothermal synthesis of monoclinic VO2 micro-and nanocrystals in one step and their use in fabricating inverse opals. *Chem. Mater.* **2010,** *22* (10), 3043-3050.

68. Popuri, S. R.; Miclau, M.; Artemenko, A.; Labrugere, C.; Villesuzanne, A.; Pollet, M. l., Rapid hydrothermal synthesis of VO2 (B) and its conversion to thermochromic VO2 (M1). *Inorg. Chem.* **2013,** *52* (9), 4780-4785.

69. Lim, Y. T.; Park, O. O.; Jung, H.-T., Gold nanolayer-encapsulated silica particles synthesized by surface seeding and shell growing method: near infrared responsive materials. *J. Colloid Interface Sci.* **2003,** *263* (2), 449-453.

70. Albert, M.; Gao, Y.; Toft, D.; Dwight, K.; Wold, A., Photoassisted gold deposition of titanium dioxide. *Mater. Res. Bull.* **1992,** *27* (8), 961-966.

71. Mandal, M.; Kundu, S.; Ghosh, S. K.; Panigrahi, S.; Sau, T. K.; Yusuf, S.; Pal, T., Magnetite nanoparticles with tunable gold or silver shell. *J. Colloid Interface Sci.* **2005,** *286* (1), 187-194.

72. Jana, S.; Basu, S.; Pande, S.; Ghosh, S. K.; Pal, T., Shape-selective synthesis, magnetic properties, and catalytic activity of single crystalline β-MnO2 nanoparticles. *J. Phys. Chem. C* **2007,** *111* (44), 16272-16277.

73. Jana, N. R.; Gearheart, L.; Murphy, C. J., Seed-mediated growth approach for shape-controlled synthesis of spheroidal and rod-like gold nanoparticles using a surfactant template. *Adv. Mater.* **2001,** *13* (18), 1389.

74. Xu, J. J.; Kinser, A. J.; Owens, B. B.; Smyrl, W. H., Amorphous manganese dioxide: a high capacity lithium intercalation host. *Electrochemical and solid-state letters* **1998,** *1* (1), 1-3.

75. Yang, J.; Xu, J. J., Nanoporous amorphous manganese oxide as electrocatalyst for oxygen reduction in alkaline solutions. *Electrochemistry communications* **2003,** *5* (4), 306-311.

76. Toupin, M.; Brousse, T.; Bélanger, D., Influence of microstucture on the charge storage properties of chemically synthesized manganese dioxide. *Chemistry of Materials* **2002,** *14* (9), 3946-3952.

77. Devaraj, S.; Munichandraiah, N., Electrochemical supercapacitor studies of nanostructured α-MnO2 synthesized by microemulsion method and the effect of annealing. *Journal of the Electrochemical Society* **2007,** *154* (2), A80-A88.

78. Bastús, N. G.; Comenge, J.; Puntes, V., Kinetically controlled seeded growth synthesis of citrate-stabilized gold nanoparticles of up to 200 nm: size focusing versus Ostwald ripening. *Langmuir* **2011,** *27* (17), 11098.

79. Sau, T. K.; Murphy, C. J., Room temperature, high-yield synthesis of multiple shapes of gold nanoparticles in aqueous solution. *J. Am. Chem. Soc.* **2004,** *126* (28), 8648-8649.

APPENDIX A – VIBRATIONS IN SOLIDS

A.1 Materials Background

Nanoparticles behave similarly to macroscopic objects from a mechanical perspective. Physicists and engineers have done a great deal of work studying the mechanical properties of large objects so it makes sense to take their findings and apply them to the very small. Unfortunately, the terms Young's modulus, elasticity, speed of sound, eigenmode, stiffness, and deflection are rarely mentioned in chemistry classes. As such, it seems wise to provide an introduction to the theory of the movement of solids.

Hooke's law states that the amount of force a spring exerts is equal to the amount that it is stretched multiplied by a constant intrinsic to that particular spring. This behavior applies reasonably well to other solids and, in particular, metals. When a normal stress (force along an axis of the object) is applied, the object will respond with strain (an elongation along that same axis). For most materials and at small stresses, this relationship is linear just like for springs. The specific constant of proportionality here will depend upon the shape of the object in question in addition to its material. To develop a truly material specific constant we need simply multiply by the cross-sectional area (A) and divide by length (L). Force (F) is thus related to change in length (ΔL):

$$F = \frac{EA}{L}\Delta L \tag{1}$$

This new constant, E, is called the Young's modulus and is material specific. It varies from less than 0.1 GPa for rubber to over 1000 GPa for diamond. A larger value indicates greater stiffness.

This equation may be simplified by the introduction of the stress, σ, and the strain, ε.

$$\sigma = \frac{F}{A} \tag{2}$$

$$\varepsilon = \frac{\Delta L}{L} \tag{3}$$

$$\sigma = E\varepsilon \tag{4}$$

The bulk modulus, K, determines how a material responds to an equal pressure pushing inwards on all sides. The small change in volume (dV) as a function of change in pressure (dP) and the initial volume (V) all play a role.

$$K = -V\frac{dP}{dV} \tag{2}$$

These two constants are sufficient to describe the mechanical properties of an ideal material. However, there are a few derived constants which give the same information but are more useful in certain calculations. The Poisson ratio, ν, is a measure of how a material thins as its ends are stretched. This is generally positive except for some unusual metamaterials. It is related to the earlier constants by:

$$\nu = \frac{1}{2} - \frac{E}{6K} \tag{3}$$

Of course, there are other ways to apply force to an object. The shear modulus, G, measures how much a rod would defect (Δx) if one end were fixed and the other were pushed perpendicular to its length (L) axis.

$$F = \frac{GA}{L}\Delta x \tag{4}$$

This provides a complete description of an isotropic material – one whose properties do not vary with the direction in which a force is applied. Crystalline materials tend to be anisotropic. However, bulk materials are typically formed from numerous, small crystalline grains with random orientations. Overall, this produces a material which appears isotropic. For nanoparticles this no longer holds because even when polycrystalline, the number of grains

tends to be low and there is often some correlation between the orientation of the grains. As discussed in this work, nanorods are made of five twinned crystals.

A.1.1 Anisotropic materials

To understand the mechanics of anisotropic materials it is handy to introduce the stiffness tensor, [C] which is just the multidimensional analogue of Young's modulus. The full matrix equation relating stress and strain is:

$$\begin{vmatrix}\sigma_{xx}\\ \sigma_{yy}\\ \sigma_{zz}\\ \sigma_{yz}\\ \sigma_{xz}\\ \sigma_{xy}\end{vmatrix} = \begin{vmatrix}C_{11} & C_{12} & C_{13} & C_{14} & C_{15} & C_{16}\\ C_{21} & C_{22} & C_{23} & C_{24} & C_{25} & C_{26}\\ C_{31} & C_{32} & C_{33} & C_{34} & C_{35} & C_{36}\\ C_{41} & C_{42} & C_{43} & C_{44} & C_{45} & C_{46}\\ C_{51} & C_{52} & C_{53} & C_{54} & C_{55} & C_{56}\\ C_{61} & C_{62} & C_{63} & C_{64} & C_{65} & C_{66}\end{vmatrix} \begin{vmatrix}\varepsilon_{xx}\\ \varepsilon_{yy}\\ \varepsilon_{zz}\\ \varepsilon_{yz}\\ \varepsilon_{xz}\\ \varepsilon_{xy}\end{vmatrix} \tag{5}$$

The terms with two of the same subscript (e.g. σ_{xx}) are the normal stresses and strains which those with different subscripts (σ_{yz}) are shear stresses and strains.

Although it would appear that there are potentially 36 unique parameters, the matrix is symmetric about its diagonal which reduces the number of parameters to 21. For an isotropic material the matrix further simplifies to:

$$C = \begin{vmatrix}C_{11} & C_{12} & C_{12} & 0 & 0 & 0\\ & C_{11} & C_{12} & 0 & 0 & 0\\ & & C_{11} & 0 & 0 & 0\\ & & & C_{11}-C_{12} & 0 & 0\\ & & & & C_{11}-C_{12} & 0\\ & & & & & C_{11}-C_{12}\end{vmatrix} \tag{6}$$

There are only two unique parameters because each direction x, y, and z are all equivalent and there is no interaction between orthogonal forces other than the narrowing that occurs perpendicular to normal forces. So,

$$C_{11} = \frac{1}{E} \tag{7}$$

$$C_{11} - C_{12} = \frac{1}{2G} \tag{8}$$

Metals, like gold and silver, frequently exhibit cubic symmetry. Each direction x, y, and z are equivalent but, the way that shear stresses relate to shear strains are not reducible to the usual Poisson ratio. Thus three unique parameters are required for full characterization C_{11}, C_{12}, C_{44}.

$$C = \begin{vmatrix} C_{11} & C_{12} & C_{12} & 0 & 0 & 0 \\ & C_{11} & C_{12} & 0 & 0 & 0 \\ & & C_{11} & 0 & 0 & 0 \\ & & & C_{44} & 0 & 0 \\ & & & & C_{44} & 0 \\ & & & & & C_{44} \end{vmatrix} \tag{9}$$

Other solids will have less symmetry and require more parameters.

A.1.2 Vibrations

All objects have natural vibrational frequencies that they can resonate with. All frequencies will cause vibrations in an object but only a few eigenfrequencies (the resonant frequencies) will create sustained vibrations that persist long after the applied force is removed. This frequency is paired with some vibrational mode – a combination of stretching, twisting, and expanding – of the object called an eigenmode or normal mode. The eigenfrequencies and eigenmodes will depend upon the size, shape, and material. Generally, smaller objects made of stiffer materials will have higher frequencies. Determining *a priori* what these frequencies should be is not trivial. Physicists have determined them for some shapes including spheres and cylinders.

A.2 Finite Element Methods

Finite element modeling is a way to numerically solve for various properties of physical systems. All that is required is that the equations governing the time evolution of relevant quantities and the material specific constants for these equations are known. It was

originally developed to assist with structural calculations but has been applied to heat transfer, mass transfer, and electromagnetic interactions.

Initially, the object under consideration is broken up into discrete points called a mesh. It is important that the density of mesh points be large enough to capture the shape of the object. This discretization is necessary to reduce a spatially continuous problem to a finite one. Next, the system must be initialized by providing the initial conditions. For a simulation of heat transfer, this would be the temperature of all points within the object.

Finally, the time evolution of the whole system is followed by using the differential equations which guide the system. For heat transfer this would involve the temperature difference between two adjacent points in the mesh and the thermal conductivity between these points. Using a small time step ensures that the final results are an accurate reflection of reality. For the mechanical simulations discussed here the discretized mesh points are treated like masses connected by springs and dampers. The standard equations of motion guide the time evolution.